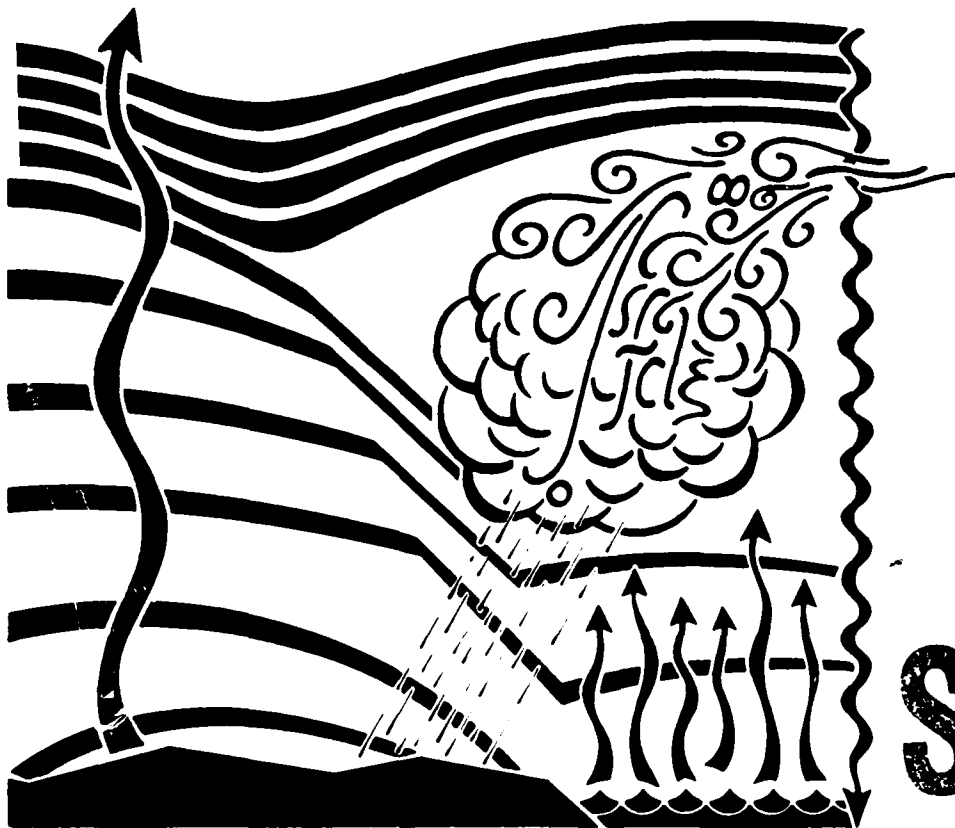




AD-A228 918

DYNAMICALLY DRIVEN ROLL CIRCULATIONS IN AN INVERSION-CAPPED BOUNDARY LAYER



by
Robert
Medred

DTIC
ELECTE
OCT 24 1990
S E D

Master of Science

August 1989

DISTRIBUTION STATEMENT A
Approved for public release;
Distribution Unlimited

90 10 22 124

August 1990

Thesis/Dissertation

Dynamically Driven Roll Circulations in an Inversion-
Capped Boundary Layer

Robert Medred

AFIT Student at: Pennsylvania State University

AFIT/CI/CIA - 90-107

AFIT/CI
Wright-Patterson AFB OH 45433

Approved for Public Release IAW AFR 190-1
Distribution Unlimited
ERNEST A. HAYGOOD, 1st Lt, USAF
Executive Officer, Civilian Institution Programs

The Pennsylvania State University
The Graduate School
Department of Meteorology

DYNAMICALLY DRIVEN
ROLL CIRCULATIONS IN AN INVERSION-CAPPED
BOUNDARY LAYER

A Thesis in
Meteorology

by
Robert Medred

Submitted in Partial Fulfillment
of the Requirements
for the Degree of
Master of Science

August 1989

Accession For	
NTIS GRA&I	<input checked="" type="checkbox"/>
DTIC TAB	<input type="checkbox"/>
Unannounced	<input type="checkbox"/>
Justification	
By _____	
Distribution/	
Availability Codes	
Dist	Avail and/or Special
A-1	



I grant The Pennsylvania State University
the nonexclusive right to use this work for
the University's own purposes and to make
single copies of the work available to
the public on a not-for-profit basis if
copies are not otherwise available.

A handwritten signature in cursive script, reading "Robert Medred". The signature is written in dark ink and is positioned above a horizontal line.

Robert Medred

We approve the thesis of Robert Medred.

Date of Signature

Hampton N. Shirer

June 26, 1989

Hampton N. Shirer
Associate Professor of Meteorology
Thesis Advisor

William M. Frank

26 June 1989

William M. Frank
Professor of Meteorology
Head of the Department of Meteorology

George S. Young

6-26-89

George S. Young
Assistant Professor of Meteorology

ABSTRACT

From a Boussinesq system of equations modified to include background wind and temperature profiles, a two-dimensional, nonlinear spectral model is derived to study the development of boundary layer roll circulations in a nonrotating, stratified environment. The spectral expansions for the dependent variables include more than one vertical harmonic, thereby allowing the determination of the structure of the roll circulations and the roles of the dynamic and thermodynamic instability mechanisms. The dynamic forcing is represented by a Fourier expansion of an arbitrary vertical profile of the background horizontal wind. The thermodynamic forcing is represented by a generalized, nonlinear background temperature profile. The spectral system of equations is obtained by using the Galerkin technique and contains the appropriate energy sources for representing both the Rayleigh-Bénard and the inflection point instability mechanisms.

In this ^{Theses} study, only the linear aspects of the roll solutions are examined through the use of a standard linear stability analysis. From this analysis are obtained the minimum critical values of the dynamic forcing parameter Re and the effective thermodynamic forcing parameter Ra_e that represent the smallest magnitudes of the forcing rates required for the onset of roll circulations. In addition,

the preferred horizontal wavelengths, circulation depths and orientations with respect to a reference direction are found for the various roll modes. (147)

The primary emphasis of this study is to test the hypothesis that dynamic forcing by wind shear in a capping inversion can interact synergistically with thermal forcing at the lower boundary to excite boundary layer roll modes that can extend into that inversion. Owing to time constraints, we do not perform the nonlinear analysis that would provide evidence confirming our hypothesis and showing whether this interaction is manifested by one or two dominant circulations in the vertical. This model is tested with an idealized wind profile and arbitrary temperature profile. The model results are examined further by using two observed wind and temperature profiles obtained from the 1981 West German field experiment KonTur. One of the temperature profiles displays a distinct capping inversion having significant wind shear; the other temperature profile is characterized by weak, generally linear behavior that has only a small portion of the capping inversion, as well as moderate wind shear, within the vertical domain. Good agreement with observations is found in the first case having a distinct inversion capping a well-mixed layer--a result unobtainable from previous, simpler models. Although the model results for the case with an observed, generally linear profile are acceptable,

they are slightly poorer than the results obtained by using the simpler model that has only an estimated linear profile. In both cases studied, many aspects of the observed roll circulations are adequately described by the inflection point instability mode that is excited by shear in the upper portion of the boundary layer, in agreement with the energetics analysis of Brümmer (1985).

TABLE OF CONTENTS

	<u>Page</u>
ABSTRACT	iii
LIST OF TABLES	viii
LIST OF FIGURES	ix
ACKNOWLEDGMENTS	xii
<u>Chapter</u>	
1 INTRODUCTION	1
1.1 Previous Studies	5
1.2 Spectral Modeling of Boundary Layer Rolls	12
2 MODEL DEVELOPMENT	17
2.1 The Partial Differential Equations	19
2.1.1 The Boussinesq System	20
2.1.2 Boundary Conditions	25
2.1.3 Dimensionless Quantities	26
2.2 The Spectral Equations	32
2.3 Orientation Angles	41
2.4 Energetics Analysis	47
3 LINEAR STABILITY ANALYSIS	50
3.1 The Linear Spectral System	53
3.2 The Hopf Bifurcation Points	57
3.3 Special Cases	67
3.3.1 Pure Inflection Point Case	68
3.3.2 Single-Wavenumber Thermal Special Cases	69
3.3.3 Steady Pure Thermal Special Case .	77

TABLE OF CONTENTS (continued)

<u>Chapter</u>		<u>Page</u>
4	MODEL RESULTS USING IDEALIZED WIND AND TEMPERATURE PROFILES	80
4.1	Billows Wind Profile	82
4.2	Idealized Temperature Profile	83
4.3	Stability of the Billows Wind Profile with and without a Capping Inversion ..	86
4.3.1	The Linear ($\varepsilon_i = 0$) Temperature Profile Case	89
4.3.2	The Nonlinear ($\varepsilon_i \neq 0$) Temperature Profile Case	97
5	MODEL RESULTS USING OBSERVED WIND AND TEMPERATURE PROFILES	110
5.1	The KonTur 1981 Observations	110
5.2	Results from Two Previous Models	118
5.3	Fourier Representation of the Profiles ..	121
5.4	Stability Results	133
5.4.1	The Linear ($\varepsilon_i = 0$) Temperature Profile Case	135
5.4.2	The Nonlinear ($\varepsilon_i \neq 0$) Temperature Profile Case	144
5.4.3	Summary of Results	153
	REFERENCES	158
Appendix	A Portion of the Output Produced by the Symbolic Manipulator CFORMAC That Was Used to Find the Coefficients in (3.12)	164

LIST OF TABLES

<u>Table</u>		<u>Page</u>
2.1	Coefficients in the Spectral Model (2.39)-(2.52)	38
2.2	Fourier Coefficients of the Background Wind Profile	39
2.3	Integrals of the Background Wind in the Reference Coordinate System	46
4.1	Effects of Varying the Level of the Inflection Point on the Inflection Point Mode	92
4.2	A Portion of the Model Output Showing a Clear Mode Transition	95
4.3	The Thermal Special Cases Using a Billows Wind Profile and an Idealized Temperature Profile.....	98
5.1	Values of the Fourier Coefficients Used in the Model	132
5.2	Comparisons of Values Specified in the Model with the Observed Values	134
5.3	Summary of Typical Model Results for the Inflection Point Instability Mode	141

LIST OF FIGURES

<u>Figure</u>		<u>Page</u>
1.1	Schematic Diagram of Typical Roll Circulations	7
2.1	A Typical Boundary Layer Temperature Profile	22
2.2	Rotation of the Standard Coordinate Axes (x_s, y_s) into the Roll Coordinate Axes (x, y)	43
3.1	Schematic of a Hopf Bifurcation Curve	51
3.2	Schematic Illustration of Three Hopf Bifurcation Curves	63
3.3	Schematic Illustration of Possible Hopf Bifurcation Curves Associated with Fig. 3.2	65
4.1	Vertical Profile of the Potential Temperature Used in the Billows Stability Analysis	87
4.2	Billows Wind Profile Given by (4.4)-(4.5)	88
4.3	Mode Diagram for the Billows Wind Profile Given by (4.4)-(4.5) Illustrated in Fig. 4.2 for the $\varepsilon_i = 0$ Case Given by the Temperature Profile (4.6) Illustrated in Fig. 4.1	90
4.4	Enlarged Version of Fig. 4.3 Isolating the Thermal (dashed line) and Inflection Point (solid line) Modes	91

LIST OF FIGURES (continued)

<u>Figure</u>	<u>Page</u>
4.5	Mode Diagram for the Billows Wind Profile Given by (4.4)-(4.5) Illustrated in Fig. 4.2 for the $\varepsilon_i \neq 0$ Case Given by the Temperature Profile (4.6) Illustrated in Fig. 4.1 99
4.6	Mode Diagram for the Billows Wind Profile (4.4)-(4.5) Illustrated in Fig. 4.2 Comparing the $\varepsilon_i = 0$ and $\varepsilon_i \neq 0$ Cases Given by the Temperature Profile (4.6) Illustrated in Fig. 4.1 102
4.7	Same as Fig. 4.6 Except for the Shear and Inflection Point Modes 103
5.1	Vertical Profiles of Potential Temperature θ , Mixing Ratio m , Along-roll Wind u and Cross-roll Wind v Measured on 18 September 1981 During KonTur 113
5.2	Vertical Profiles of Potential Temperature θ , Mixing Ratio m , Along-roll Wind u and Cross-roll Wind v Measured on 26 September 1981 During KonTur 114
5.3	A Comparison of the Observed Profiles (Fig. 5.1; dashed lines) and the Approximate Profiles (solid lines) of the Along-roll Wind v and the Cross-roll Wind u on 18 September 1981 124
5.4	A Comparison of the Observed Profiles (Fig. 5.2; dashed lines) and the Approximate Profiles (solid lines) of the Along-roll Wind v and the Cross-roll Wind u on 26 September 1981 125

LIST OF FIGURES (continued)

<u>Figures</u>	<u>Page</u>
5.5 A Comparison of the Observed Potential Temperature Profile (Fig. 5.1; dashed line), the Approximate Profile of Potential Temperature (solid line) and Its Linear Component (dotted line) for 18 September 1981	126
5.6 A Comparison of the Observed Potential Temperature Profile (Fig. 5.2; dashed line), the Approximate Profile of Potential Temperature (solid line) and Its Linear Component (dotted line) for 26 September 1981	127
5.7 Mode Diagram for the $\varepsilon_i = 0$ Case on 26 September 1981	136
5.8 Mode Diagram for the $\varepsilon_i = 0$ Case on 18 September 1981	137
5.9 Contour Diagram Showing Values of Ra_c as Functions of a and β for $Re_c = 50$ in the $\varepsilon_i = 0$ Case for 18 September 1981 Shown in Fig. 5.8	144
5.10 Mode Diagram for the $\varepsilon_i \neq 0$ Case on 26 September 1981	147
5.11 Contour Diagram Showing Values of Ra_c as Functions of a and β for $Re_c = 150$ in the $\varepsilon_i \neq 0$ Case for 26 September 1981 Shown in Fig. 5.10.....	148
5.12 Mode Diagram for the $\varepsilon_i \neq 0$ Case on 18 September 1981	149

ACKNOWLEDGMENTS

I extend my sincere thanks to Professor Hampton N. Shirer for his unselfish efforts, guidance, and understanding that he offered to me throughout this project. I also extend thanks to Tracy Haack-Hirschberg and Mark Laufersweiler. Their assistance on various aspects of this research made my learning experience more meaningful and efficient.

I am grateful to the United States Air Force for providing me this opportunity to obtain an advanced degree through the Air Force Institute of Technology civilian institution program. Additional support for this research was provided by the Office of Naval Research through contract N000014-86-K-06880.

Chapter 1
INTRODUCTION

In the present study, we examine the effects of wind shear in a capping temperature inversion on the development of roll circulations in the planetary boundary layer. Although the boundary layer is usually viewed as extending only up to the inversion base, we will broaden this convention somewhat to equate the depth of the roll circulation with the depth of the boundary layer. In this thesis, we extend the spectral model of Haack-Hirschberg (1988) for nonrotating, two-dimensional, thermally and dynamically forced flow by including a generalized vertical temperature profile in addition to an arbitrary background horizontal wind profile.

Horizontal rolls usually are confined to a boundary layer that is capped by an inversion, but in some cases, the roll circulations may extend some distance into that inversion. Certainly, roll circulations that are driven thermodynamically from the surface must remain below the inversion. Thus rolls may extend into the inversion only if sufficient dynamic forcing occurs within the inversion itself.

Brümmer (1985) presents evidence via visual observations and an energetics analysis that in some cases roll circulations do indeed extend into the stable

inversion layer and are not simply bounded by the average level of the inversion base. Apparently then, a deep roll circulation may develop via a synergistic interaction of the motions forced thermally from below the inversion and the motions forced dynamically from within the inversion. In this case, the inversion base is not a material surface forming a lower boundary for a circulation decoupled from the well-mixed layer, as is often assumed. Thus modeling the effect of dynamic forcing within a capping inversion on boundary layer roll development by permitting the rolls to extend into the inversion rather than just to perturb it, is a physically relevant goal, and it is the goal of the present study. An improvement in previous spectral models (e.g., Shirer and Brümmer, 1986; Haack-Hirschberg, 1988) for these types of cases is possible by improving the representation of the basic state temperature variations via inclusion of a nonlinear vertical temperature profile in the model.

Boundary layer roll circulations may be influenced by convectively forced gravity waves that are reflected by the stratosphere or by the capping inversion itself (Clark et al., 1986). Because we do not include in our model the complicated and not yet fully understood interactions of gravity waves with the boundary layer, we are not representing the effects related to these convection waves, even though they may substantially influence the results.

Favorable results obtained with the boundary layer-limited model, however, may provide some evidence that the effect of gravity waves on roll circulations is of secondary importance.

From observational studies, characteristic background flows and typical spatial and temporal features have been associated with roll circulations (e.g., Kuettner, 1959; LeMone, 1973; Kelly, 1984). Theoretical studies of roll circulations have identified four possible instability mechanisms, three of which are well known: a thermal mechanism, which is due to the Rayleigh-Bénard convective instability, and two dynamic mechanisms, which are due to the inflection point instability and the parallel instability (Brown, 1980). More recently, a fourth dynamic instability mechanism, the shear instability, was discovered by Haack-Hirschberg (1988), but the properties of this new instability mechanism are not yet fully understood. Finally, numerical and analytical models have further clarified the properties of roll circulation modes that arise from the three well known driving instability mechanisms (e.g., Faller and Kaylor, 1966; Asai, 1970; Shirer, 1986; Shirer and Stensrud, 1988). Although these efforts have improved our understanding of roll circulations, we continue to seek a relatively efficient but accurate means for diagnosing all the mechanisms underlying roll circulations. Lorenz (1963) demonstrated

the adequacy of using low-order spectral models to represent convective flows, and we use this type of model to examine several boundary layer instability mechanisms.

As mentioned earlier, we develop a modified version of the low-order spectral model created by Haack-Hirschberg (1988), who combined two previous models: the pure dynamic model of Stensrud and Shirer (1988) and the single-wavenumber thermal model of Shirer (1986). A model that contains representations of both of the dynamic and thermodynamic forcing rates adequately captures the thermal and inflection point instability mechanisms that are thought predominantly to produce boundary layer roll circulations (Kuettner, 1971). Linear analyses of low-order models yield the critical values of the appropriate forcing parameters whose magnitudes must be exceeded in order for rolls to form. The relevant forcing parameters for the present study are the effective Rayleigh number Ra_e , which represents the magnitude of the surface-based thermodynamic forcing Ra as modified by thermal dissipative effects of a capping inversion or a stably stratified boundary layer, and the Reynolds number Re that represents the magnitude of the dynamic forcing by the background wind shear. The critical values of these parameters, denoted by Ra_{ec} and Re_c , are functions of the horizontal cell wavelength L , the orientation angle β with respect to a fixed reference direction, and the assumed

depth z_T of the roll circulation. The minimum values of Ra_{ec} and Re_c , denoted by $(Ra_{ec})_{min}$ and $(Re_c)_{min}$, designate the minimum, critical forcing rates necessary for roll development to occur. The corresponding values of L , β and z_T yield the preferred geometry, L_p , β_p and z_{Tp} of the resulting roll circulations. Finally, from the above parameter values, the preferred values of the roll propagation period T_p may be obtained.

To provide a visual representation of the relationship between the critical dynamic and thermodynamic forcing rates, we plot the values of $(Ra_{ec})_{min}$ as a function of the values of $(Re_c)_{min}$. Often several curves can be drawn, one associated with each particular instability mode. If the parameter values for the atmosphere cross one of the transition curves for a roll circulation, then the associated roll mode is expected to develop.

1.1 Previous Studies

Kuettner (1959) studied boundary layer roll circulations identified through the presence of linear cloud patterns known as cloud streets, and he was among the first researchers to identify the characteristics and causes of these cloud patterns. The existence of cloud streets indicates that roll circulations are occurring, but the lack of cloud streets does not indicate an absence of

roll circulations. It is generally believed that the clouds simply act as tracers identifying the roll circulations and that roll circulations occur much more frequently than do cloud streets (e.g., Kuettner, 1971; Brown, 1980). Extensive observation of cloud streets has provided information on typical roll wavelengths, orientation angles and propagation periods. This data suggests that roll circulations are predominantly two-dimensional, have wavelengths ranging from one to eight times the depth of the boundary layer (Kelly, 1984) and propagate with periods of between 15 minutes and two hours (Brown, 1972). Cloud streets commonly occur in environments having moderate to strong wind shear (Kuettner, 1959, 1971), although in some cases they occur in relatively light winds as well (Plank, 1966). The orientation of the roll axis is generally parallel to the direction of the mean wind shear in the boundary layer (Kuettner, 1959, 1971). Figure 1.1, taken from Brown (1980), shows a schematic of the structure of roll circulations that we study.

Since roll circulations are a frequently occurring phenomenon in the boundary layer, it has been recognized that a better understanding of these secondary circulations may provide a better understanding of how the planetary boundary layer interacts with the free atmosphere (Brown, 1970). It follows that increasing our knowledge of

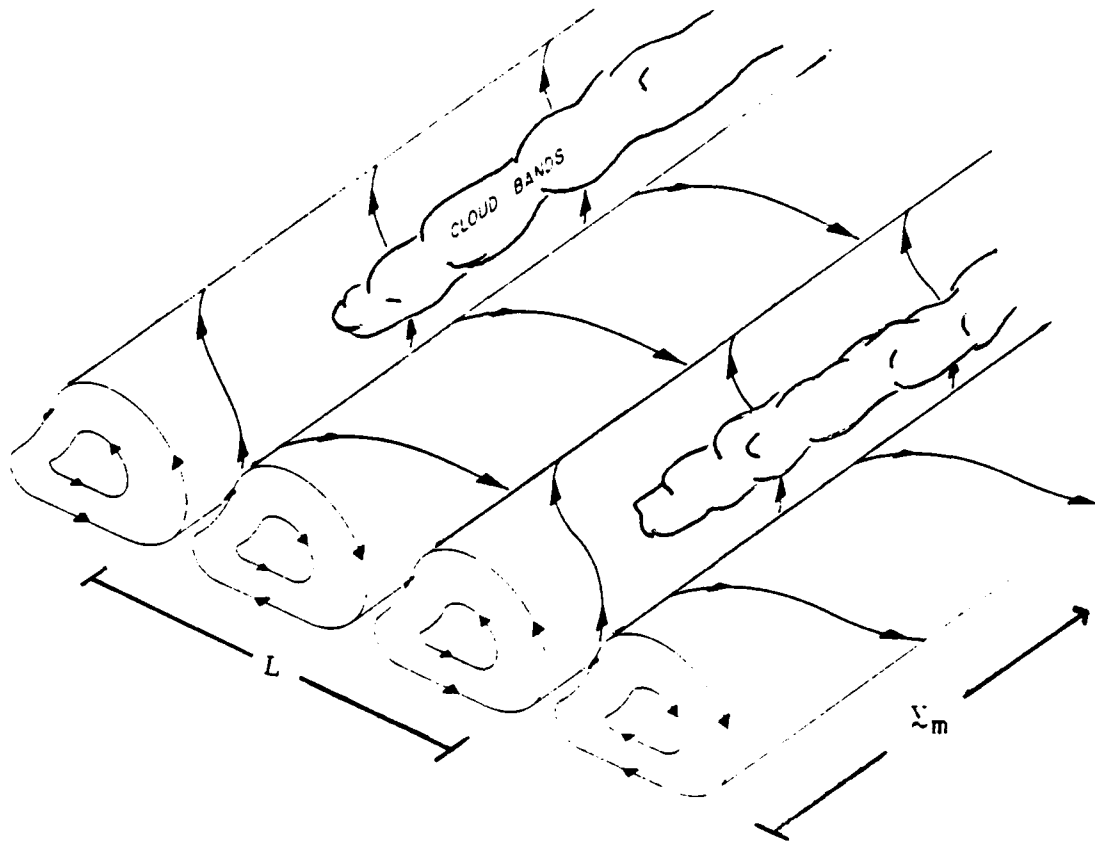


Fig. 1.1 Schematic Diagram of Typical Roll Circulations. These circulations have wavelength L and are oriented approximately parallel to the direction of the mean boundary layer wind u_m (from Brown, 1980).

boundary layer/free atmosphere interactions will help improve techniques characterizing the effects of the boundary layer via the use of bulk quantities, and that these results will lead ultimately to improved general circulation models.

As mentioned earlier, roll circulations commonly manifest themselves in the form of cloud streets and these streets often occur within stratocumulus outbreaks. The surface area of the globe that is covered by stratocumulus cloud decks is significant, being quite persistent in the Northern Hemisphere summer near the eastern boundaries of the subtropical oceans and in the Arctic region (Agee et al., 1973; Suarez et al., 1983). Both global climate models and general circulation models would benefit from a better understanding of how these essentially solid cloud decks form and evolve. In some cases, roll circulations play a major part in the dissipation of these stratocumulus cloud decks (e.g., Nicholls, 1984). It is therefore important to discover the conditions under which the roll instability mechanisms can act to cause a solid deck of stratocumulus to break into streets. The decrease in effective surface albedo in these situations would be significant since an area that previously was covered completely by clouds becomes mostly clear; this clearing occurs because the surface area covered by cloud streets is only a fraction of the area over which the roll

circulations extend. Roll circulations also act to affect the energy transfer between the boundary layer and the free atmosphere. Rolls modify the existing energy balance by increasing surface friction, extracting momentum from the mean flow and redistributing surface heating, moisture and turbulence (LeMone, 1973). All of the above interactions upon the boundary layer and free atmosphere warrant further study of roll circulations.

As noted earlier, the four instability mechanisms that have been identified with the development of boundary layer rolls are the thermal instability, the inflection point instability, and the parallel instability (Brown, 1980) as well as the shear instability (Haack-Hirschberg, 1988). The thermal instability is often called the Rayleigh-Bénard instability in honor of Lord Rayleigh who studied the generation of roll circulations in Bénard convection. This mechanism may operate in a statically unstable environment when a sufficiently large positive lapse rate exists near the surface. When this lapse rate, represented by a Rayleigh number Ra , exceeds a critical value, roll circulations form to replace the motionless, conductive state. In this case, convective perturbations are able to grow by extracting energy from the background thermal state (Shirer, 1986). The mean background wind shear also influences the thermal instability mechanism by causing free convective cellular patterns to form into linear

patterns with respect to the mean wind shear direction when the mean wind speed is greater than just a few meters per second (Kuettnner, 1959, 1971). Indeed, Kuettnner (1971) has shown that a wind component normal to the roll circulation axis imposes a stabilizing effect on the transport of heat via convection. Consequently, thermally driven rolls acquire alignments that minimize this cross-roll component of the wind shear (Shirer, 1980). These two-dimensional rolls can bifurcate into three-dimensional cellular patterns if the lapse rate increases sufficiently in magnitude relative to that of the wind shear (Kuettnner, 1971).

In a dry neutrally or stably stratified environment, the potential temperature lapse rate is necessarily nonpositive and thus, perturbations must derive energy from the background wind profile (Stensrud and Shirer, 1988; Haack-Hirschberg, 1988). Two such dynamic mechanisms are described in the literature: the inflection point instability mechanism, which is a form of the Kelvin-Helmholtz instability, and the parallel instability mechanism. Rayleigh (1880) discovered that a wind profile with an inflection point was inherently unstable to infinitesimal perturbations. However, an inflection point is a necessary but not a sufficient condition for this instability mechanism to exist (Drazin and Howard, 1966). More recently, Brummer and Latif (1984) revealed that an

inflection point located near the middle of the domain yields the most unstable unidirectional wind profile. For this dynamic mode, perturbations grow by extracting energy from the component of the wind shear normal to the roll axis. Therefore, roll circulations generated by the inflection point instability mechanism are generally aligned normal to the (unidirectional) wind component that has the maximum amount of shear (Haack-Hirschberg, 1988; Stensrud and Shirer, 1988).

In contrast, the parallel instability mechanism is characterized by the growth of perturbations that extract energy from the along-roll wind shear (Kaylor and Faller, 1972). Rolls formed by this mechanism are aligned parallel to the direction of along-roll wind shear, as are the rolls produced by the thermal instability mechanism. Lilly (1966) was the first to study the parallel instability mechanism and revealed that it is a function of the Coriolis force and the (eddy) viscosity. Thus, including the Coriolis terms in a physical system can make along-roll perturbations energetically active. However, Brown (1970) concluded that this instability mechanism is not important at values of Reynolds numbers or wind speeds typical of the atmosphere. In contrast, other investigators (e.g., Etling, 1971; Kaylor and Faller, 1972) believe that the Coriolis terms provide a significant source of energy to the development of roll circulations.

The fourth known instability mechanism is the shear instability that was recently identified by Haack-Hirschberg (1988). This dynamic instability mechanism, which may be a form of gravity wave instability, is characterized by a strongly stratified ($Ra < 0$) atmosphere and by relatively strong wind shear or large values of the Reynolds number. For simple wind profiles, the growth of perturbations is preferred in the direction normal to the mean wind shear, as with the inflection point instability, but is not dependent on the existence of an inflection point in the wind profile. Perturbations occurring under the above conditions can grow from any wind profile having sufficient wind shear.

1.2 Spectral Modeling of Boundary Layer Rolls

In many previous studies of secondary flow instabilities for boundary layer roll development (e.g., Brown, 1970; Etling, 1971; LeMone, 1973), investigators have reduced the partial differential equations into a system of wind profile-specific ordinary differential equations in appropriate amplitude variables, or to a single high-order differential equation in one of the variables. These methods produce satisfactory results but are lengthy and complicated to develop and require significant computer time. In more recent years, the

low-order modeling approach has been employed to represent the roll circulation modes developing from the above instability mechanisms. Lorenz (1960) introduced this modeling concept, which is based on the assumption that the dependent variables may be represented by a small number of horizontal and vertical harmonics. From the shallow Boussinesq system of equations, Lorenz (1963) used the Galerkin technique (described by Higgins, 1987) to derive the smallest possible nonlinear spectral model for the representation of Rayleigh-Bénard convection. A complete review of the Lorenz model and of nonlinear hydrodynamic modeling in general is found in the book edited by Shirer (1987a).

Spectral modeling of roll circulations has been conducted using successively more complicated low-order models. Spectral models developed by Shirer and Dutton (1979), Shirer (1980), Shirer (1986), Stensrud and Shirer (1988) and Haack-Hirschberg (1988) have extended the Lorenz (1963) model to include the known significant instability mechanisms pertaining to roll circulations. The resulting roll characteristics compare well with those obtained from earlier numerical models of Rayleigh-Bénard convection and more importantly with observations. The method of low-order spectral modeling has, however, been criticized by some who are concerned that the severe truncation used to represent the dependent amplitude coefficients may

prevent sufficient representation of the full physical problem. Indeed, these concerns still remain at present. However, because spectral models can represent the background wind profile explicitly through the Fourier coefficients of the wind and wind shear, Shirer (1980) noted that this modeling approach is ideal for direct comparisons between theory and observations. Now, owing to the work in this thesis, the background temperature profile can also be represented explicitly by suitably chosen Fourier coefficients, hence adding an important degree of freedom to the problem.

As a test of the adequacy of our model, we apply it to some particular cases. First we use idealized wind and temperature profiles in order to ensure that this model adequately represents the known instability mechanisms, and to test our hypothesis that rolls may extend into a capping inversion if sufficient dynamic forcing is available in that inversion. Then we compare our model results with observations taken during the KonTur field experiment (Brümmer *et al.*, 1985).

The study here is a linear analysis that is the first step toward finding the complete nonlinear solution, which is planned as future work. The full solution consists of roll circulations and roll-produced modifications to the background profiles composing the basic state; the summation of the basic state and its modification by the

roll circulations yields an interactive basic state. Observations necessarily involve this altered basic state, and Shirer and Haack (1989) have shown that removing the roll modifications from the background wind yields a better estimate of the basic state that is forcing the rolls. As a consequence, a better estimate of the preferred geometry of the expected roll modes is obtained; these preferred values must be chosen before the nonlinear solution is found. Once this full roll solution is known, we will be able to confirm the accuracy of the model results via calculations of the energetics of the solutions. In addition, we will be able to determine if one or two circulations are dominant in the vertical via the availability of two vertical wavenumbers in the vertical. Thus, obtaining good results for the preferred geometry using the linear version of the full model is an important indication that the nonlinear model is able to capture the essential physics of the problem.

The Haack-Hirschberg (1988) model results for the 18 September 1981 case of the KonTur experiment did not match observations very well because, in contrast to the wind profile, the observed nonlinear temperature profile was estimated using only a linear function. We find that our model, which is an extension of the dynamic/thermodynamic model of Haack-Hirschberg (1988), gives results that compare very favorably with the observed data, with the

greatest improvement occurring in the dynamically driven capping inversion case of 18 September. Here, the good results we obtain suggest that our model captures at least the minimum degrees of freedom needed to study roll circulations. Thus the geometry of roll circulations can now be adequately described by a spectral model for the generalized case of rolls extending into a capping inversion in a sheared environment.

In Chapter 2, we present the full spectral model for the combined thermal and dynamic instability mechanisms. In subsequent chapters we perform a standard stability analysis of the linearized system, and the resulting roll circulation modes are investigated using various idealized and observed wind and temperature profiles.

Chapter 2

MODEL DEVELOPMENT

As we mentioned in Chapter 1, there are four mechanisms known to affect the formation of horizontal rolls--three dynamic and one thermal. Two of the dynamic instabilities, the inflection point instability (Brown, 1980) and shear instability (Haack-Hirschberg, 1988), originate primarily from the effects of cross-roll vertical wind shear on perturbations in the basic flow. The third dynamic instability, parallel instability, originates from along-roll wind shear and rotation in the background flow owing to the Coriolis force (Shirer, 1986). Finally, the thermal instability occurs primarily when the effects of surface heating dominate the dynamic instabilities (Kuettner, 1971). To keep our model as simple as possible while retaining the major characteristics of the roll circulations, we choose to concentrate on the most common instabilities--inflection point and thermal (Brown, 1980). In doing so we are ignoring the parallel instability by neglecting the Coriolis force. This simplification can be justified since the time scale on which roll circulations exist is usually less than the time scale on which the Coriolis force is important (Brown, 1980). As we see in Chapter 4, the shear instability appears to be limited to atmospheric conditions having strong static stability.

Since our model includes both dynamic and thermodynamic forcing rates, we require the following shallow Boussinesq equations for the perturbations describing the rolls: the vertical and horizontal equations of motion, the thermodynamic equation, the ideal gas law and the incompressible form of the continuity equation. Shirer (1986) found that in the presence of sufficient background wind shear, the first perturbations to grow produce circulations that vary only in the cross-roll plane. This is the mode we seek since it forms at a minimum value of the forcing. Thus, variations along the roll axis may be assumed to be negligible, and so the system of equations reduces to a two-dimensional one. A set of spectral equations is then derived using appropriate Fourier expansions for the perturbations and the background wind and temperature profiles. Haack-Hirschberg (1988) gives an energetics analysis showing that the spectral system in the linear temperature profile case contains the dynamic and thermodynamic energy sources required to form roll circulations. When the capping inversion containing wind shear is included, we will find here that the basic energetics analysis remains essentially unchanged, with the inversion acting thermally as an energy sink but dynamically as an energy source.

2.1 The Partial Differential Equations

Because roll circulations are limited to very shallow depths of the atmosphere (less than about 4 kilometers), we invoke the Boussinesq approximation that is modified slightly to include arbitrary height-dependent background wind and temperature structures. In this system, as in all Boussinesq systems, the roll circulations are assumed to be perturbations imposed on a conductive basic state. The basic state is hydrostatic and consists of arbitrary, vertically varying, background temperature and horizontal wind profiles. We use the first six coefficients in a Fourier series to represent the background wind profile (Stensrud and Shirer, 1988) and three Fourier coefficients to represent the background temperature profile.

The basic flow has much larger spatial and temporal scales than the roll circulations. Therefore, we assume that time-independent background profiles lead to roll circulations that in turn may alter these background profiles. The fluid domain is assumed to be cyclically continuous in the x , or roll-perpendicular, direction. The y -axis defines the roll-parallel direction. Correspondingly, $u(z)$ is the cross-roll wind component and $v(z)$ is the along-roll wind component.

2.1.1 The Boussinesq System

The Boussinesq expansions for the dependent variables are

$$u(x,z,t) = U(z) + u'(x,z,t) \quad , \quad (2.1)$$

$$w(x,z,t) = w'(x,z,t) \quad , \quad (2.2)$$

$$T(x,z,t) = T_0(z) + T'(x,z,t) \quad , \quad (2.3)$$

in which

$$T_0(z) = T_{00} - \Delta_z T(\text{water-air})(z/z_T - 1) + H(z) \quad , \quad (2.4)$$

$$p(x,z,t) = p_{00} - \rho_0 g z + p'(x,z,t) \quad , \quad (2.5)$$

$$\rho(x,z,t) = \rho_0 + \rho'(x,z,t) \quad , \quad (2.6)$$

and in which the variables T_{00} , ρ_0 and p_{00} are constants, $\Delta_z T(\text{water-air})$ is the temperature difference between the ocean surface and the air above it and z_T is the domain or roll circulation height.

The forcing mechanism for the convection is the surface temperature difference $\Delta_z T(\text{water-air})$; thus this term must be positive in order for convective rolls to

form. In the absence of this forcing, the background air temperature profile is $T_{oo} + H(z)$ where $H(z)$ is defined as

$$H(z) = - \Delta_z T_{(air)} z / z_T + G(z) \quad , \quad (2.7)$$

in which

$$G(z) = T_1 \cos(\pi z / z_T) + T_2 \sin(2\pi z / z_T) + T_3 \cos(2\pi z / z_T) \quad , \quad (2.8)$$

and the coefficients T_i are constants. The first term on the right of (2.7) is the linear lapse rate of the observed temperature profile and is generally nonzero when the inversion is included; thus $|\Delta_z T_{(air)} / z_T|$ is usually less than the dry adiabatic lapse rate γ_d . The second term on the right of (2.7) is the harmonic part of the observed temperature profile and the Fourier expansion we use for it is given in (2.8). Including some of the harmonic portions allows for a representation of an arbitrary background temperature profile. Figure 2.1 displays a vertical temperature profile denoting the applicable variables. The solid line in Fig 2.1 depicts the temperature profile produced by including the harmonic terms in $H(z)$. Obviously, we see that three trigonometric terms cannot reproduce the original temperature profile exactly. However, the small deviations from the original profile

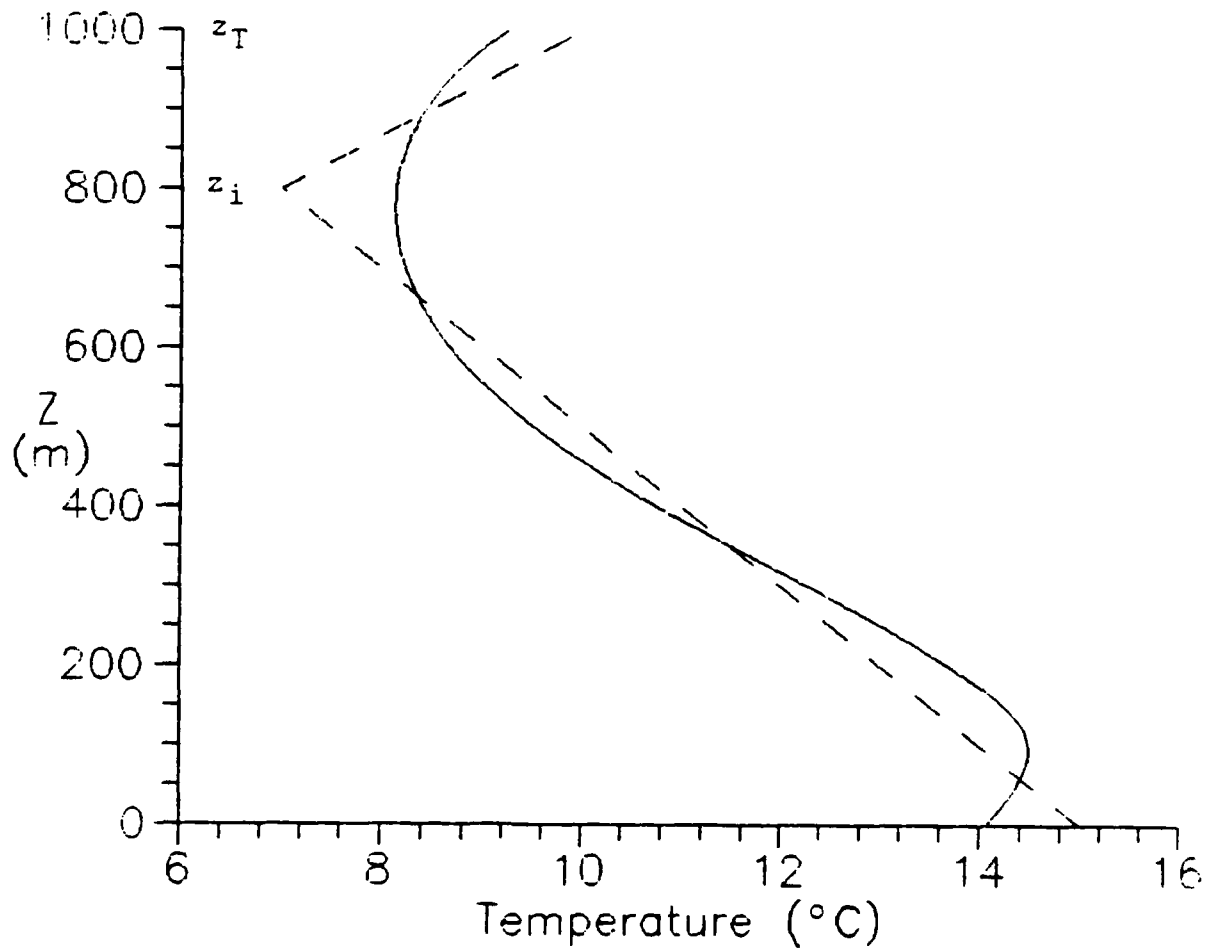


Fig. 2.1 A Typical Boundary Layer Temperature Profile. This profile is given by (4.6)-(4.7) (dashed line) and its approximation $H(z)$ is given by (2.7)-(2.8) (solid line). The air temperature near the surface decreases at the dry adiabatic lapse rate γ_d until the inversion base z_i and then increases within the inversion at the constant inversion lapse rate $\gamma_{(inv)}$ until the domain top z_T .

giving for example the apparent stable layer near the surface, are physically meaningless in this model because we use vertical wavenumbers one and two to represent the flow, necessarily filtering the effects of these small deviations. In Section 2.2 we show the relationship between $G(z)$ and the Fourier integrals of the temperature profile that define the coefficients T_i .

The primed variables in (2.1)-(2.5) denote the perturbations due to the rolls. Upon substituting these quantities into the complete partial differential system and discarding small terms, we obtain a set of modified Boussinesq equations in which the trivial solution represents the basic state and the nontrivial solutions represent the dynamic states, or roll circulations (Dutton, 1986).

We represent the wind flow with a streamfunction ψ in order to reduce our problem to one in the two variables ψ and T' . The following form of the streamfunction satisfies the continuity equation $\nabla \cdot \mathbf{y}' = 0$:

$$\frac{\partial \psi}{\partial z} = -u' \quad ; \quad \frac{\partial \psi}{\partial x} = w' \quad . \quad (2.9)$$

A vorticity equation is formed next. With the pressure gradient term eliminated, the Boussinesq equations may be

written as

$$\frac{\partial}{\partial t}(\nabla^2 \psi) + J(\psi, \nabla^2 \psi) - \frac{g}{T_0} \frac{\partial T'}{\partial x} - \frac{\partial \psi}{\partial x} \frac{\partial^2 U}{\partial z^2} + U \frac{\partial}{\partial x}(\nabla^2 \psi) - \nu \nabla^4 \psi = 0, \quad (2.10)$$

$$\frac{\partial T'}{\partial t} + J(\psi, T') - \frac{\partial \psi}{\partial x} B(z) + U \frac{\partial T'}{\partial x} - \kappa \nabla^2 T' = 0, \quad (2.11)$$

in which the nonlinear Jacobian operator J is defined as

$$J(f, g) = \frac{\partial f}{\partial x} \frac{\partial g}{\partial z} - \frac{\partial f}{\partial z} \frac{\partial g}{\partial x}, \quad (2.12)$$

ν is the coefficient of eddy viscosity and κ is the coefficient of eddy thermometric conductivity. The buoyancy term $B(z)$ is the difference between the background and dry adiabatic lapse rates and can be written as

$$\begin{aligned} B(z) &= - \frac{\partial T_0}{\partial z} - \gamma_d \\ &= \left[\Delta_z T(\text{water-air}) / z_T - \frac{\partial H}{\partial z} \right] - \gamma_d. \end{aligned} \quad (2.13)$$

2.1.2 Boundary Conditions

We assume that the horizontal flow is 2π -periodic since the vertical boundaries that define the horizontal

portion of the domain are cyclically continuous. This condition allows for the horizontal propagation of the roll circulations by the background wind--a necessary condition for modeling cloud streets. The width of the horizontal domain is given by a characteristic wavelength L , where $0 \leq x \leq L$; preferred values for L are given by a stability analysis (Chapter 3). In the vertical the rolls are confined to the region given by $0 \leq z \leq z_T$, where z_T specifies the top of the domain. Unlike in previous models, z_T is not necessarily at the bottom z_i of the inversion. Instead, the roll circulations in this model can extend into the capping inversion, provided that there is sufficient dynamic forcing. The value of z_T is variable, allowing rolls of various depths to be compared in order to see if their extension into the capping inversion is plausible (Chapter 5).

A well posed initial/boundary value problem must have appropriate boundary conditions if unique solutions are to exist. We will choose the vertical boundary conditions to be those that are frequently used and mathematically the simplest in this type of modeling: rigid, stress-free, and perfectly conducting (e.g., Shirer, 1986). The boundary conditions on ψ and T' are

$$\psi(0,z) = \psi(L,z) \quad , \quad (2.14)$$

$$\psi(x,0) = \psi(x,z_T) = \nabla^2 \psi(x,0) = \nabla^2 \psi(x,z_T) = 0 \quad , \quad (2.15)$$

$$T'(0,z) = T'(L,z) \quad , \quad (2.16)$$

$$T'(x,0) = T'(x,z_T) = 0 \quad . \quad (2.17)$$

Boundary conditions always limit the Fourier representation of the variables owing to the required choice of basis functions. However, the above boundary conditions force no unacceptable limitations since our physical problem allows full waves horizontally and half waves vertically.

2.1.3 Dimensionless Quantities

Using dimensionless forms for the variables in the model equations allows the parameters of interest to be revealed while producing the fewest number of parameters in the equations. *A priori*, we know the general form of the forcing rates in the system of equations, and we have generally accepted definitions of the dimensionless parameters. The goal of non-dimensionalizing is to choose appropriate forms for the variables so that the proper forms for the dimensionless parameters result in the dimensionless equations.

In the modified Boussinesq system, the Reynolds number Re , given by (2.31), and the effective Rayleigh number Ra_e ,

given by

$$Ra_e = Ra + Ra_i \quad , \quad (2.18)$$

are the control parameters. The terms on the right of (2.18) are defined in (2.32), (2.33) and (2.34), respectively. The Reynolds number represents the dynamic forcing rate, and the effective Rayleigh number represents the effectiveness of the thermal forcing in the presence of an inversion with its associated wind shear. As we discuss more below, necessary conditions for rolls to extend into an inversion are given by $Ra_e > 0$ and $Re > 0$; sufficient conditions are that the value of Ra_{ec} exceeds that of a critical effective Rayleigh number Ra_{ec} and that the value of Re exceeds that of a critical Reynolds number Re . The first term on the right of (2.18) is the standard Rayleigh number that represents the instability due to the thermal forcing by the sea surface water/air temperature difference. The second term on the right of (2.18) represents the average potential temperature lapse rate in the domain. As discussed in Chapter 1, a capping inversion containing sufficient wind shear can force boundary layer convection that reaches the bottom z_i of the inversion to extend somewhat into that inversion. Roll circulations that extend into the inversion necessarily have a non-zero value of Ra_i . Since the effect of the inversion is to

increase domain static stability, Ra_i is normally negative. Thus for rolls to extend into the inversion, $|Ra|$ must be greater than $|Ra_i|$ in order for $Ra_e > 0$ to occur. Of course, if the rolls do not extend into the inversion and if the boundary layer is well mixed, then $Ra_i = 0$ and $Ra_e = Ra$. As we discuss later, the rolls respond to these forcing rates by assuming preferred horizontal wavelengths and orientations with respect to the mean wind shear direction; as noted above, we can determine whether and how far the rolls may extend into the inversion by determining the dependence of Ra_{ec} and Re_c on z_T .

The definitions used to specify the dimensionless forms, which are denoted by asterisks, are

$$x = x^* L / 2\pi \quad , \quad (2.19)$$

$$z = z^* z_T / \pi \quad , \quad (2.20)$$

$$t = t^* z_T L / (2\pi^2 \kappa) \quad , \quad (2.21)$$

$$\psi = \psi^* \kappa \quad , \quad (2.22)$$

$$T' = T^* \pi^3 \nu \kappa T_0 / (g z_T^3) \quad , \quad (2.23)$$

$$U(z) = |\underline{V}(z_T)| U^*(z^*) \quad , \quad (2.24)$$

$$V(z) = |\underline{V}(z_T)| V^*(z^*) \quad , \quad (2.25)$$

$$\tilde{\nabla}^2 = a^2 \frac{\partial^2}{\partial x^{*2}} + \frac{\partial^2}{\partial z^{*2}} \quad (2.26)$$

For consistency, we note that (2.24) and (2.25) imply that

$$U^{*2}(\pi) + V^{*2}(\pi) = 1. \quad (2.27)$$

Finally, the aspect ratio is defined to be

$$a = 2z_T/L \quad (2.28)$$

Substituting the dimensionless forms (2.19)-(2.28) into the Boussinesq versions of the vorticity and thermodynamic equations (2.10)-(2.11) produces the following system that models shallow roll circulations:

$$\begin{aligned} \frac{\partial}{\partial t^*} (\tilde{\nabla}^2 \psi^*) + J^*(\psi^*, \tilde{\nabla}^2 \psi^*) - P \frac{\partial T^*}{\partial x^*} + P \text{Re} U^* \frac{\partial}{\partial x^*} (\tilde{\nabla}^2 \psi^*) \\ - P \text{Re} \frac{\partial \psi^*}{\partial x^*} \frac{\partial^2 U^*}{\partial z^{*2}} - \frac{P}{a} \tilde{\nabla}^2 \psi^* = 0 \quad , \quad (2.29) \end{aligned}$$

$$\begin{aligned} \frac{\partial T^*}{\partial t^*} + J^*(\psi^*, T^*) + P \text{Re} U^* \frac{\partial T^*}{\partial x^*} + \left(\frac{\partial G^*}{\partial z^*} - \text{Ra}_e \frac{\partial \psi^*}{\partial x^*} \right) \\ - \frac{1}{a} \tilde{\nabla}^2 T^* = 0 \quad . \quad (2.30) \end{aligned}$$

The control parameter Re is defined to be

$$Re = |V(z_T)| z_T / (\pi \nu) \quad . \quad (2.31)$$

The control parameter Ra_e originates from $B(z)$ in (2.13) and is defined in (2.19) to be $Ra_e = Ra + Ra_i$. Here, Ra is the surface-based thermal forcing defined as

$$Ra = \left\{ \Delta_z T(\text{water-air}) \right\} \left\{ \frac{g z_T^3}{\pi^3 T_o \nu \kappa} \right\} ; \quad (2.32)$$

Ra_i is the thermal contribution from the atmosphere and is defined as

$$Ra_i = \left\{ \frac{\Delta_z T(\text{air})}{z_T} - \gamma_d \right\} \left\{ \frac{g z_T^4}{\pi^3 T_o \nu \kappa} \right\} . \quad (2.33)$$

Using Poisson's equation, we may express (2.33) in terms of the potential temperature gradient $\Delta_z \theta(\text{air})$ via

$$Ra_i = - \left\{ \frac{\Delta_z \theta(\text{air})}{z_T} \right\} \frac{g z_T^4}{\pi^3 \theta_o \nu \kappa} . \quad (2.34)$$

Finally, the harmonic contribution to the lapse rate is given by

$$\frac{\partial G^*}{\partial z^*} = -T_1^* \sin(z^*) + 2T_2^* \cos(2z^*) - 2T_3^* \sin(2z^*) \quad . \quad (2.35)$$

Other than being dimensionless, equations (2.32)-(2.33) are analogous to $B(z)$ in (2.13) except that the background lapse rate $-\partial T_0/\partial z$ in (2.13) is now separated into two physically distinct terms: the positive forcing rate is placed in (2.32) and the thermally stabilizing portion is placed in (2.33). For convenience γ_d is placed in (2.33) so that a neutral lapse rate gives a well-mixed layer, or $Ra_i = 0$. This separation more clearly indicates that the effective Rayleigh number Ra_e can be viewed as having two mathematically distinct portions. In the special case, $G(z) = 0$, of no harmonic contribution, this system reduces to that of Haack-Hirschberg (1988), who considered an atmosphere with a stable lapse rate. Implicit in her model are both terms $\Delta_z T_{(water-air)} z/z_T$ and $\Delta_z T_{(air)} z/z_T$ in $T_0(z)$. The effective Rayleigh number Ra_e is analogous to her Rayleigh number, although our definitions clearly distinguish between the destabilizing water-air temperature difference that forces convection and the stabilizing air temperature difference that retards it.

Because we do not include latent heating effects in the model, we do not use the virtual potential temperature θ_v while recognizing that Laufersweiler and Shirer (1989) have shown that latent heating can significantly affect roll circulations. We do not consider this lack of degree of freedom as significant in our case studies presented in Chapter 5 because there, the value of θ is a reasonably

good approximation to θ_v and because we are emphasizing dynamic forcing effects.

The Prandtl number P is defined to be

$$P = \nu/\kappa \quad , \quad (2.36)$$

and the dimensionless Jacobian operator J^* is analogous to that of J except for the addition of asterisks indicating that it is operating on dimensionless variables. In the next section, we derive the spectral representations corresponding to the dimensionless system (2.29)-(2.30).

2.2 The Spectral Equations

The boundary conditions, as determined in the previous section, allow us to express the system (2.29)-(2.36) by ordinary differential equations that exploit the harmonic nature of the dependent variables in the system. We use the Galerkin technique (e.g., Higgins, 1987) to transform the Boussinesq equations into spectral form. The spatial character of the dependent variables ψ^* and T^* must be represented by orthogonal trigonometric basis functions. After Haack-Hirschberg (1988), we use the following truncated Fourier series to provide appropriate spectral expansions for ψ^* and T^* :

$$\begin{aligned}
\psi^*(x^*, z^*, t^*) = & \\
& \psi_1(t^*)\sin(x^*)\sin(qz^*) + \psi_2(t^*)\cos(x^*)\sin(qz^*) \\
& + \psi_3(t^*)\sin(x^*)\sin(nz^*) + \psi_4(t^*)\cos(x^*)\sin(nz^*) \\
& + \psi_5(t^*)\sin((q-n)z^*) + \psi_6(t^*)\sin((q+n)z^*) \quad , \quad (2.37)
\end{aligned}$$

and

$$\begin{aligned}
T^*(x^*, z^*, t^*) = & \\
& T_1(t^*)\cos(x^*)\sin(qz^*) + T_2(t^*)\sin(x^*)\sin(qz^*) \\
& + T_3(t^*)\cos(x^*)\sin(nz^*) + T_4(t^*)\sin(x^*)\sin(nz^*) \\
& + T_5(t^*)\sin((q-n)z^*) + T_6(t^*)\sin((q+n)z^*) \\
& + T_7(t^*)\sin(2qz^*) + T_8(t^*)\sin(2nz^*) \quad . \quad (2.38)
\end{aligned}$$

The spectral expansions (2.37)-(2.38) were chosen for both mathematical and physical reasons; the numerical subscripts are used for notational convenience to identify each of the dependent amplitude variables. The expansions (2.37)-(2.38) must satisfy the boundary conditions, must allow translation of the rolls through the horizontal domain by representing all possible horizontal phase relationships between the harmonic components (Pyle, 1987), and must capture the dynamic and thermal instability mechanisms (Stensrud and Shirer, 1988). Stensrud (1985) and Stensrud and Shirer (1988) showed that two vertical wavenumbers are required with $q = 1$ and $q < n$ in order to represent the infection point instability. Earlier researchers (i.e.,

Saltzman, 1962 and Lorenz, 1963) showed that only three spectral terms remained after long temporal integrations of a larger convective model without a background wind (Shirer, 1987b). In the spectral model (2.39)-(2.52), based on (2.37)-(2.38), four such triplet submodels (ψ_1, T_1, T_7) , (ψ_2, T_2, T_7) , (ψ_3, T_3, T_8) , and (ψ_4, T_4, T_8) are linked nonlinearly via $(\psi_5, \psi_6, T_5, T_6)$ in order that propagating rolls can be modeled. In (2.37)-(2.38) the streamfunction coefficients ψ_5 and ψ_6 and the temperature coefficients T_5 through T_8 represent the nonlinear modification of the background wind and temperature profiles by the roll circulations.

A 14-coefficient spectral model is obtained by substituting (2.37)-(2.38) into the dimensionless system (2.29)-(2.30) and taking the appropriate derivatives. Our system consists of rate equations $\dot{\psi}_i$ and \dot{T}_j for each of the amplitude coefficients ψ_i and T_j . The spatial dependence in the partial differential equations is eliminated by multiplying them by each one of the basis functions in (2.37)-(2.38) and integrating the result over the domain. Since we have expressed the dependent variables in terms of trigonometric functions, the orthogonality of the basis functions causes most of the terms in the resulting equation to vanish. The 14-coefficient model we obtain is similar to that of Haack-Hirschberg (1988) and is given by

$$\begin{aligned} \frac{\partial \psi_1}{\partial t^*} = & d_1 T_1 + \operatorname{Re}(a_1 \psi_2 + a_2 \psi_4) - P b_1 \psi_1 + c_1 \psi_4 \psi_5 \\ & + c_2 \psi_4 \psi_6, \end{aligned} \quad (2.39)$$

$$\begin{aligned} \frac{\partial \psi_2}{\partial t^*} = & -d_1 T_2 - \operatorname{Re}(a_1 \psi_1 + a_2 \psi_3) - P b_1 \psi_2 - c_1 \psi_3 \psi_5 \\ & - c_2 \psi_3 \psi_6, \end{aligned} \quad (2.40)$$

$$\begin{aligned} \frac{\partial \psi_3}{\partial t^*} = & d_2 T_3 + \operatorname{Re}(a_3 \psi_4 + a_4 \psi_2) - P b_2 \psi_3 + c_3 \psi_2 \psi_5 \\ & + c_4 \psi_2 \psi_6, \end{aligned} \quad (2.41)$$

$$\begin{aligned} \frac{\partial \psi_4}{\partial t^*} = & -d_2 T_4 - \operatorname{Re}(a_3 \psi_3 + a_4 \psi_1) - P b_2 \psi_4 - c_3 \psi_1 \psi_5 \\ & - c_4 \psi_1 \psi_6, \end{aligned} \quad (2.42)$$

$$\frac{\partial \psi_5}{\partial t^*} = -P b_3 \psi_5 + \frac{c_5}{2} (\psi_1 \psi_4 - \psi_2 \psi_3), \quad (2.43)$$

$$\frac{\partial \psi_6}{\partial t^*} = -P b_4 \psi_6 - \frac{c_6}{2} (\psi_1 \psi_4 - \psi_2 \psi_3), \quad (2.44)$$

$$\begin{aligned} \frac{\partial T_1}{\partial t^*} = & c_6 (\psi_5 T_4 - \psi_3 T_5) + c_5 (\psi_3 T_6 - \psi_6 T_4) + c_7 \psi_1 T_7 \\ & - \operatorname{Re}(a_5 T_2 + a_6 T_4) + (Ra_e + \varepsilon_1) \psi_1 \\ & + \varepsilon_2 \psi_3 - b_1 T_1, \end{aligned} \quad (2.45)$$

$$\begin{aligned} \frac{\partial T_2}{\partial t^*} = & c_6 (\psi_4 T_5 - \psi_5 T_3) + c_5 (\psi_6 T_3 - \psi_4 T_6) - c_7 \psi_2 T_7 \\ & + \operatorname{Re}(a_5 T_1 + a_6 T_3) - (Ra_e + \varepsilon_1) \psi_2 \\ & - \varepsilon_2 \psi_4 - b_1 T_2, \end{aligned} \quad (2.46)$$

$$\begin{aligned} \frac{\partial T_3}{\partial t^*} &= c_6(\psi_5 T_2 - \psi_1 T_5) + c_5(\psi_1 T_6 - \psi_6 T_2) + c_8 \psi_3 T_8 \\ &\quad - \text{Re}(a_6 T_2 + a_7 T_4) + \varepsilon_2 \psi_1 + (Ra_e + \varepsilon_3) \psi_3 \\ &\quad - b_2 T_3 \quad , \end{aligned} \quad (2.47)$$

$$\begin{aligned} \frac{\partial T_4}{\partial t^*} &= c_6(\psi_2 T_5 - \psi_5 T_1) + c_5(\psi_6 T_1 - \psi_2 T_6) - c_8 \psi_4 T_8 \\ &\quad + \text{Re}(a_6 T_1 + a_7 T_3) - \varepsilon_2 \psi_2 - (Ra_e + \varepsilon_3) \psi_4 \\ &\quad - b_2 T_4 \quad , \end{aligned} \quad (2.48)$$

$$\frac{\partial T_5}{\partial t^*} = \frac{c_6}{2}(\psi_1 T_3 + \psi_3 T_1 - \psi_4 T_2 - \psi_2 T_4) - b_3 T_5 \quad , \quad (2.49)$$

$$\frac{\partial T_6}{\partial t^*} = \frac{c_5}{2}(\psi_2 T_4 + \psi_4 T_2 - \psi_1 T_3 - \psi_3 T_1) - b_4 T_6 \quad , \quad (2.50)$$

$$\frac{\partial T_7}{\partial t^*} = \frac{c_7}{2}(\psi_2 T_2 - \psi_1 T_1) - b_5 T_7 \quad , \quad (2.51)$$

$$\frac{\partial T_8}{\partial t^*} = \frac{c_8}{2}(\psi_4 T_4 - \psi_3 T_3) - b_6 T_8 \quad . \quad (2.52)$$

The spectral equations (2.39)-(2.52) contain four sets of coefficients a_i , b_i , c_i , and d_i that are defined in Table 2.1. The coefficients denoted by a_i appear with the dynamic forcing parameter Re and originate from the inclusion of a height-dependent background wind $U(z)$ in the partial differential equations (2.10)-(2.11). These coefficients depend on the Fourier coefficients of the background wind profile that are defined in Table 2.2. The coefficients denoted by b_i originate from the

dissipative terms $\nabla^4 \psi$ and $\nabla^2 T'$ in (2.10)-(2.11). The coefficients c_i occur only in the nonlinear terms as a result of the Jacobian operator J in (2.10)-(2.11). Finally, the coefficients d_i appear in the thermodynamic energy conversion terms in the vorticity equation. The occurrence of these four types of terms in the ordinary differential spectral system indicates that all terms in the partial differential equations are represented in the spectral system (Haack-Hirschberg, 1988).

A special case occurs when $n = 3q$ because the spectral coefficients T_3 and T_7 are equal and opposite (Haack-Hirschberg, 1988). In this case, the 14-coefficient model reduces to a 13-coefficient one. Since we will be doing a linear analysis, this special case will not affect our results.

The effective Rayleigh number Ra_e appears in (2.45)-(2.48) together with the Fourier coefficients ε_i that represent the harmonic part $\partial G^*/\partial z^*$ of the background lapse rate. Together, these terms represent the entire stability term $B(z)$. In general these Fourier coefficients are defined as

$$\varepsilon_1 = -\frac{2}{\pi} \int_0^\pi \frac{\partial G^*}{\partial z^*} \sin^2(qz^*) dz^* , \quad (2.53)$$

Table 2.1

Coefficients in the Spectral Model (2.39)-(2.52).

These coefficients are functions of the aspect ratio a , the vertical wavenumbers q and n , the Fourier coefficients of the background wind Λ_i and Γ_i , and the Prandtl number P . The integrals Λ_i and Γ_i are given in Table 2.2

($s = a^2 + q^2$, and $t = a^2 + n^2$) (after Haack-Hirschberg, 1988).

i	a_i	b_i	c_i	d_i
1	$\frac{P}{s} (\Lambda_1 + \Gamma_1)$	$\frac{s}{a}$	$\frac{(n-q)}{2s} (q^2 - 2qn - a^2)$	$\frac{P}{s}$
2	$\frac{P}{s} (t \Lambda_2 + \Gamma_2)$	$\frac{t}{a}$	$\frac{(n+q)}{2s} (a^2 - 2qn - q^2)$	$\frac{P}{t}$
3	$\frac{P}{t} (t \Lambda_3 + \Gamma_3)$	$\frac{(n-q)^2}{a}$	$\frac{(n-q)}{2t} (n^2 - 2qn - a^2)$	---
4	$\frac{P}{t} (s \Lambda_2 + \Gamma_2)$	$\frac{(n+q)^2}{a}$	$\frac{(n+q)}{2t} (a^2 - 2qn - n^2)$	---
5	$P \Lambda_1$	$\frac{4q^2}{a}$	$\frac{(n+q)}{2}$	---
6	$P \Lambda_2$	$\frac{4n^2}{a}$	$\frac{(n-q)}{2}$	---
7	$P \Lambda_3$	---	q	---
8	---	---	n	---

Table 2.2

Fourier Coefficients of the Background Wind Profile.
The variable $U^*(z^*)$ is the dimensionless cross-roll wind component, and the variables q and n are vertical integral wavenumbers (after Haack-Hirschberg, 1988).

i	Λ_i	Γ_i
1	$\frac{2}{\pi} \int_0^\pi U^* \sin^2(qz^*) dz^*$	$\frac{2}{\pi} \int_0^\pi \frac{\partial^2 U^*}{\partial z^{*2}} \sin^2(qz^*) dz^*$
2	$\frac{2}{\pi} \int_0^\pi U^* \sin(qz^*) \sin(nz^*) dz^*$	$\frac{2}{\pi} \int_0^\pi \frac{\partial^2 U^*}{\partial z^{*2}} \sin(qz^*) \sin(nz^*) dz^*$
3	$\frac{2}{\pi} \int_0^\pi U^*(z^*) \sin^2(nz^*) dz^*$	$\frac{2}{\pi} \int_0^\pi \frac{\partial^2 U^*}{\partial z^{*2}} \sin^2(nz^*) dz^*$

$$\varepsilon_2 = - \frac{2}{\pi} \int_0^\pi \frac{\partial G^*}{\partial z^*} \sin(nz^*) \sin(qz^*) dz^* , \quad (2.54)$$

$$\varepsilon_3 = - \frac{2}{\pi} \int_0^\pi \frac{\partial G^*}{\partial z^*} \sin^2(nz^*) dz^* , \quad (2.55)$$

where q and n are vertical wavenumbers. Since we have

direct measurements of the observed temperature profile and not of the rate of change of the observed temperature profile, we will find it convenient to integrate these definitions by parts. The coefficients (2.53)-(2.55) then become

$$\varepsilon_1 = \frac{2}{\pi} \int_0^{\pi} G^*(z^*) q \sin(2qz^*) dz^* , \quad (2.56)$$

$$\varepsilon_2 = \frac{1}{\pi} \int_0^{\pi} \left\{ G^*(z^*) \left[(n+q) \sin((n+q)z^*) - (n-q) \sin((n-q)z^*) \right] \right\} dz^* , \quad (2.57)$$

$$\varepsilon_3 = \frac{2}{\pi} \int_0^{\pi} G^*(z^*) n \sin(2nz^*) dz^* . \quad (2.58)$$

For our specific representation (2.8) of $G^*(z^*)$ we find that ε_i and T_i^* are related by

$$\varepsilon_1 = \frac{8}{3\pi} T_1^* + T_2^* , \quad (2.59)$$

$$\varepsilon_2 = \frac{T_3^*}{\pi} \left[\frac{(n-q)^2}{(3-n)(1+n)} - \frac{(n+q)^2}{(n+3)(1-n)} \right] , \quad (2.60)$$

$$\varepsilon_3 = - \frac{8n^2}{\pi(1-4n^2)} T_1^* . \quad (2.61)$$

We will use these relationships in Chapters 4 and 5 when we use observations to determine values for the ε_i terms.

2.3. Orientation Angles

We now introduce the response parameter β , the orientation angle between the roll axis and a fixed reference direction. The orientation of the roll with respect to the background wind is probably the most distinguishable aspect of roll circulations and so it requires proper representation. The preferred roll geometry is determined by assuming that the preferred orientations and aspect ratios are those that yield the smallest values for the critical forcing parameters Ra_{ec} and Re_c . As mentioned earlier, the a_i terms contain integrals with respect to height of the background wind--more specifically, integrals of the mean background wind A_i and of the mean wind curvature Γ_i representing the wind shear. The wind component $U(z)$ in the integrals is defined to be along the cross-roll coordinate x .

It is well known that the rolls align approximately parallel to the mean wind direction in the boundary layer, or more accurately, parallel to the mean direction of vertical wind shear (Shirer, 1986; Stensrud, 1987). It is therefore important to know the cross-roll and along-roll components of the background wind. The background winds are measured in a standard reference system. In order to isolate the roll wind components from those in this reference system, it is advantageous to rotate the

reference system into the roll coordinate system. Figure 2.2 depicts the rotation procedure, where the wind vector \underline{V} has a component U_s parallel to the standard x_s -axis and a component V_s parallel to the standard y_s -axis. Upon performing the rotation, we introduce the orientation angle β that is defined to be the angle between the roll axis y and the standard x_s -axis. Thus the amount that the standard coordinate must be rotated in order for the background wind to be aligned parallel to the roll axis is given by $\beta - 90^\circ$. A right-handed coordinate system is used such that angles counterclockwise of the x_s -axis are designated positive and angles clockwise of the x_s -axis are designated negative. The x_s -axis can be chosen for convenience. For example, in dealing with observed wind profiles as in Chapter 5, we will use the mean wind direction to define x_s . Each wind component of the roll coordinate system has contributions from two wind components of the standard coordinate system. Thus we use the formulas

$$U^*(z^*) = U_s^*(z^*)\sin \beta - V_s^*(z^*)\cos \beta \quad , \quad (2.62)$$

$$V^*(z^*) = U_s^*(z^*)\cos \beta + V_s^*(z^*)\sin \beta \quad . \quad (2.63)$$

The restriction placed on the wind speed at the top of the domain given by (2.27) also applies to the standard winds.

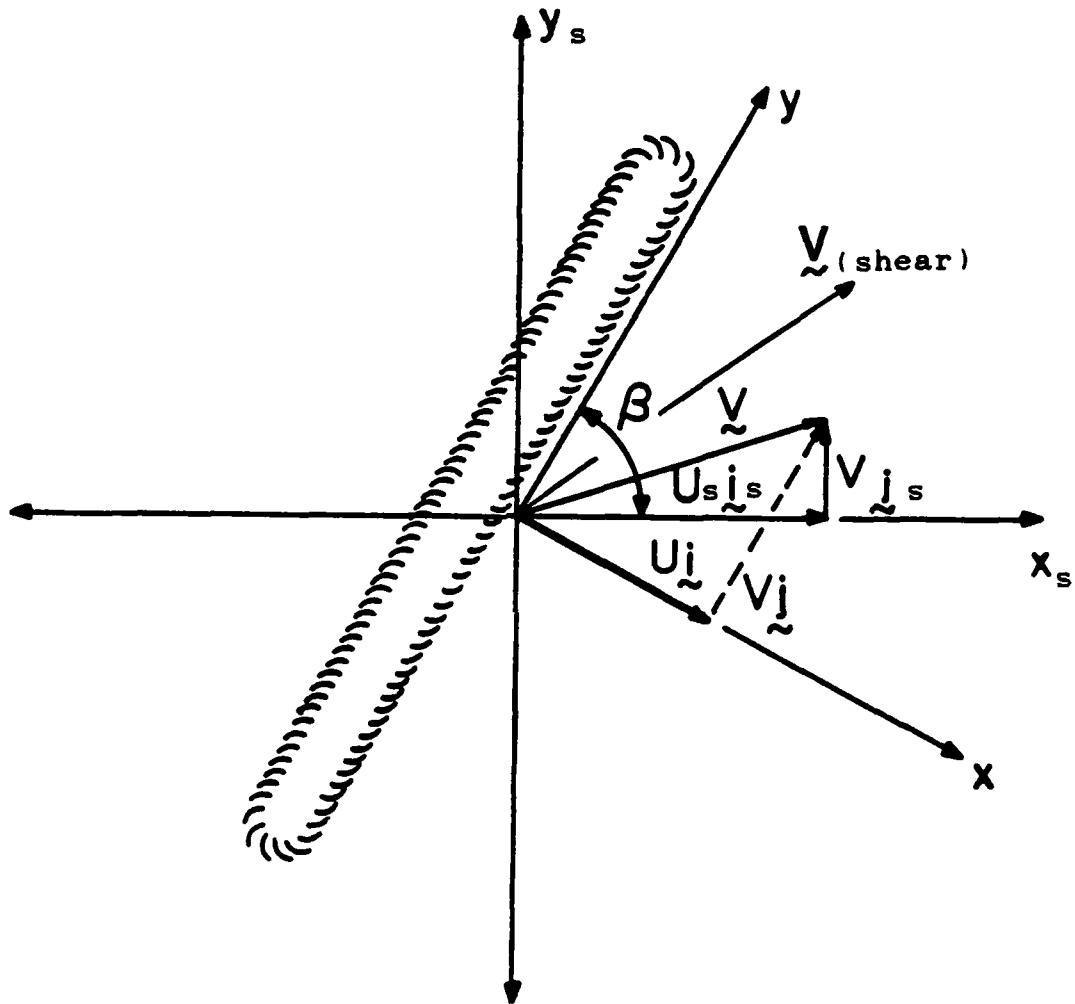


Fig. 2.2 Rotation of the Standard Coordinate Axes (x_s, y_s) into the Roll Coordinate Axes (x, y). The roll orientation β is the angle between the standard axis x_s and the roll axis y (after Pyle, 1987).

Thus the restriction on the standard winds become

$$U_S^{*2}(\pi) + V_S^{*2}(\pi) = 1 \quad . \quad (2.64)$$

To use the observed winds, we must first integrate the wind curvature terms Γ_i by parts to transform the integrals of $\partial^2 U^* / \partial z^{*2}$ into integrals of U^* . Since we have neglected the Coriolis force, the along-roll winds do not enter into problem. Thus we need only consider the cross-roll expression (2.62) when we relate the Fourier coefficients to the reference winds. The coefficients in Table 2.2 become

$$\Gamma_1 = \frac{4q^2}{\pi} \int_0^\pi U^*(z^*) \cos(2qz^*) dz^* \quad , \quad (2.65)$$

$$\Gamma_2 = \frac{1}{\pi} \int_0^\pi U^*(z^*) \left\{ (q+n)^2 \cos((q+n)z^*) - (q-n)^2 \cos((q-n)z^*) \right\} dz^* \quad , \quad (2.66)$$

$$\Gamma_3 = \frac{4n^2}{\pi} \int_0^\pi U^*(z^*) \cos(2nz^*) dz^* \quad . \quad (2.67)$$

All of the Fourier coefficients in our example can now be defined in terms of the reference coordinate system by substituting (2.62) into the forms in Table 2.2 for Λ_i and into (2.65)-(2.67) for Γ_i . These substitutions give (after Haack-Hirschberg, 1988)

$$\Lambda_1 = U_1 \sin \beta - V_1 \cos \beta , \quad (2.68)$$

$$\Lambda_2 = U_2 \sin \beta - V_2 \cos \beta , \quad (2.69)$$

$$\Lambda_3 = U_3 \sin \beta - V_3 \cos \beta , \quad (2.70)$$

$$\Gamma_1 = US_1 \sin \beta - VS_1 \cos \beta , \quad (2.71)$$

$$\Gamma_2 = US_2 \sin \beta - VS_2 \cos \beta , \quad (2.72)$$

$$\Gamma_3 = US_3 \sin \beta - VS_3 \cos \beta , \quad (2.73)$$

in which the U_i , V_i , US_i , and VS_i are integrals of the background wind components in the reference coordinate system and are defined in Table 2.3. The addition of the orientation angle via rotations in the Fourier coefficients of the background wind now make the spectral model complete.

2.4. Energetics Analysis

A thorough energetics analysis of the model equations for the special case $\varepsilon_i = 0$ can be found in Haack-Hirschberg (1988). We note that the $\varepsilon_i = 0$ case satisfactorily contains the energy sources for both dynamic and thermodynamic instability mechanisms, a conversion term and a dissipation term. Of particular interest to our

Table 2.3
Integrals of the Background Wind in
the Reference Coordinate System.

The variable $U_S^*(z^*)$ is the wind in the x_S -direction, and $V_S^*(z^*)$ is the component at right angles to $U_S^*(z^*)$. The variables q and n are vertical integral wavenumbers (after Haack-Hirschberg, 1988).

$$U_1 = \frac{2}{\pi} \int_0^\pi U_S^* \sin^2(qz^*) dz^* \quad US_1 = \frac{4q^2}{\pi} \int_0^\pi U_S^* \cos(2qz^*) dz^*$$

$$U_2 = \frac{2}{\pi} \int_0^\pi U_S^* \sin(qz^*) \sin(nz^*) dz^* \quad US_2 = \frac{(q+n)^2}{\pi} \int_0^\pi U_S^* \cos((q+n)z^*) dz^*$$

$$U_3 = \frac{2}{\pi} \int_0^\pi U_S^* \sin^2(nz^*) dz^* \quad - \frac{(q-n)^2}{\pi} \int_0^\pi U_S^* \cos((q-n)z^*) dz^*$$

$$US_3 = \frac{4n^2}{\pi} \int_0^\pi U_S^* \cos(2nz^*) dz^*$$

$$V_1 = \frac{2}{\pi} \int_0^\pi V_S^* \sin^2(2qz^*) dz^* \quad VS_1 = \frac{4q^2}{\pi} \int_0^\pi V_S^* \cos(2qz^*) dz^*$$

$$V_2 = \frac{2}{\pi} \int_0^\pi V_S^* \sin(qz^*) \sin(nz^*) dz^* \quad VS_2 = \frac{(q+n)^2}{\pi} \int_0^\pi V_S^* \cos((q+n)z^*) dz^*$$

$$- \frac{(q-n)^2}{\pi} \int_0^\pi V_S^* \cos((q-n)z^*) dz^*$$

$$V_3 = \frac{2}{\pi} \int_0^\pi V_S^* \sin^2(nz^*) dz^* \quad VS_3 = \frac{4n^2}{\pi} \int_0^\pi V_S^* \cos(2nz^*) dz^*$$

model is the effect of the capping inversion. As mentioned earlier, the capping inversion increases atmospheric stability and so it acts as a thermal sink. In addition, it increases atmospheric instability due to its associated wind shear and so it acts as a dynamic source. The effective Rayleigh number Ra_e represents the thermal stability of the atmosphere and is composed of the sum of the destabilizing effect of the water/air surface temperature difference and the stabilizing effect of the linear component of the temperature profile. Because the contribution of the linear component may be over- or underestimated by the inclusion of the harmonic terms as depicted by Fig. 2.1, the contribution of the harmonic portion of the temperature profile may cause a phenomenon known as "ringing". Ringing may be caused by undulations about the linear function that introduce spurious energy sources/sinks.

The rate of change of total roll energy, which is given by the sum of the total kinetic and available potential energy rates of change, can be written schematically as

$$\begin{aligned} \frac{\partial(E)}{\partial t} &= \frac{\partial(KE)}{\partial t} + \frac{\partial(APE)}{\partial t} \\ &= RS + G(APE) - INV - D(KE + APE) \quad , \quad (2.74) \end{aligned}$$

in which the Reynolds stress term RS is defined as (from Haack-Hirschberg, 1988)

$$RS = P \text{ Re } \Lambda_2 \left[(n^2 - q^2) \psi_1 \psi_4 + (q^2 - n^2) \psi_2 \psi_3 \right] , \quad (2.75)$$

the generation term is defined as

$$G(\text{APE}) = P \text{ Ra} / (-\text{Ra}_i) (T_1 \psi_1 - T_2 \psi_2 + T_3 \psi_3 - T_4 \psi_4) , \quad (2.76)$$

and the inversion effect is given by

$$\begin{aligned} \text{INV} = & - P / (-\text{Ra}_i) (\varepsilon_1 T_1 \psi_1 - \varepsilon_1 T_2 \psi_2 + \varepsilon_3 T_3 \psi_3 \\ & - \varepsilon_3 T_4 \psi_4 + \varepsilon_2 \psi_3 T_1 - \varepsilon_2 \psi_4 T_2 + \varepsilon_2 \psi_1 T_3 - \varepsilon_2 \psi_2 T_4) . \end{aligned} \quad (2.77)$$

Since a steady-state condition $\partial(E)/\partial t = 0$ exists for roll circulations (Haack and Shirer, 1989), the rolls are maintained when energy sources balance energy sinks. Thus in this case (2.74) can be written as

$$D(\text{KE} + \text{APE}) + \text{INV} = \text{RS} + G(\text{APE}) . \quad (2.78)$$

If the rolls are to be maintained in the presence of dissipation and an inversion, then for fixed $G(\text{APE})$ (i.e., sea surface/air temperature difference or Ra), RS must

increase in value. Thus in order for rolls to extend into an inversion, there must be sufficient wind shear acting on the rolls to overcome the thermal retarding effects in INV. The only way this may occur is if the rolls are driven from above by the shear, and from below by the sea surface/air temperature difference.

In Chapter 3, the roll modes will be determined by the manner in which the rolls capitalize on the various energy sources. These modes are found from a linear stability analysis of the conductive solution and will be shown to arise from a Hopf bifurcation to a periodic solution.

Chapter 3

LINEAR STABILITY ANALYSIS

Now that the spectral system of equations (2.39)-(2.52) has been developed, the next step in determining the conditions under which horizontal rolls may form is to conduct a linear stability analysis of the system. As mentioned in Chapter 2, rolls form only when the dynamic and thermodynamic forcing rates Re and Ra_e overcome the dissipative effects by exceeding their critical values Re_c and Ra_{ec} .

A means of representing these critical values is to form a curve in (Ra, Re) -parameter space; such a curve is also a function of the response parameters--the aspect ratio a , the orientation angle β and the domain height z_T . Because we wish to plot only the thermal forcing rate Ra , we must first subtract any thermal contribution of the atmosphere, which is given by $Ra_i < 0$, from the effective thermal forcing rate Ra_e that our model calculates, as can be seen by (2.18). The method by which the contribution from the atmosphere is removed from Ra_e is demonstrated in Chapter 5.

An example of a stability curve, as described above, is shown in Fig. 3.1. To find the bifurcation points from which roll solutions emanate, we perform a linear stability

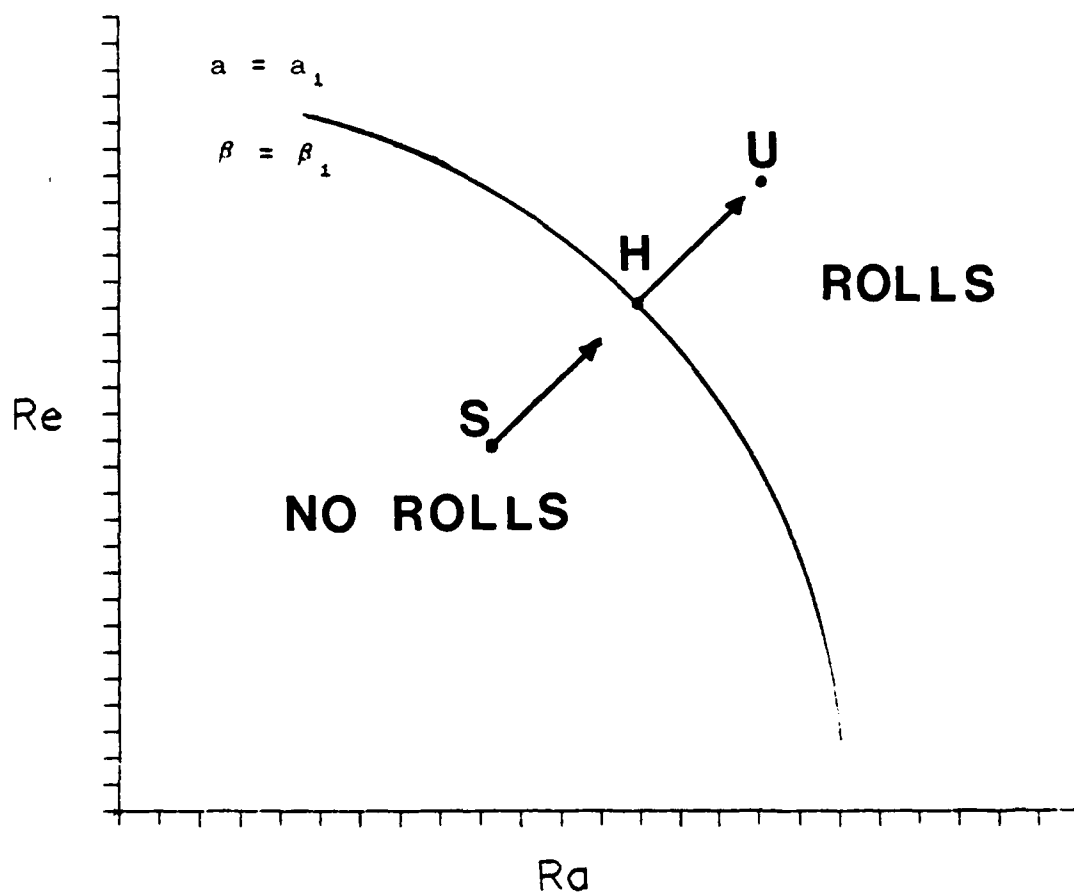


Fig. 3.1 Schematic of a Hopf Bifurcation Curve. The critical values of the forcing rates Ra_c and Re_c are determined from particular values of aspect ratio a_1 , orientation angle β_1 and domain height z_T (from Haack-Hirschberg, 1988).

analysis of the conductive solution of (2.39)-(2.52). Because the solutions branching from these bifurcation points apparently are supercritical (Haack and Shirer, 1989), all values of forcing in the region below and to the left of the curve (e.g., point S), represent perturbations that damp to the conductive or trivial solution. Here, roll circulations are not excited. As the forcing rates increase to the critical values $Re = Re_c$ and $Ra = Ra_c$ (in this example, the magnitude of the dynamic and the thermodynamic forcing rates are equal), a bifurcation to a new solution occurs. This bifurcation point (point H) signals an exchange of stability from one solution to another. In our case, H is known as a Hopf bifurcation point, as will be discussed later. Perturbations do not grow or decay until the forcing rates exceed those for the Hopf bifurcation points. At these values, the perturbations amplify and the conductive solution becomes unstable (point U). If the new solutions emanating from the Hopf bifurcation points are supercritical, then they will be stable temporally periodic ones and so they will represent propagating roll circulations.

In previous studies of roll circulations (Shirer, 1980; Stensrud, 1985, 1987; and Stensrud and Shirer, 1988) it was found that, usually, temporally periodic solutions emanated from the bifurcation point even though a bifurcation to a stable steady solution is in general also

a possibility. Steady solutions were possible, but only as special cases of the temporally periodic ones. Thus, we will only consider Hopf bifurcation points that signal an exchange of stability from the conductive solution to a temporally periodic one (Marsden and McCracken, 1976; Pyle, 1987).

As discussed by Haack-Hirschberg (1988), her full model contains the special cases of the two-vertical wavenumber pure inflection point instability mechanism (Stensrud, 1987; Stensrud and Shirer, 1988), and the single-vertical wavenumber model of the thermal instability mechanism (Shirer, 1986; Stensrud, 1987). In Section 3.3 we confirm that our modification to the Haack-Hirschberg model maintains these two submodels.

3.1 The Linear Spectral System

In this section we linearize and reduce the spectral system of equations in order to simplify and perform the stability calculations. According to Hartman's Theorem, a nonlinear system can be adequately represented by its linear component at points arbitrarily close to the bifurcation point (technically a hyperbolic fixed point) of the nonlinear system (Devaney, 1987). In addition, a linear solution that is stable is also nonlinearly stable

to sufficiently small perturbations, while unstable linear solutions are nonlinearly unstable to any perturbation (Hirsch and Smale, 1974). In general a linear stability analysis is devised to find the unstable wave mode that grows the fastest. This mode is the most unstable and dominant one and it is also the most unstable one for the nonlinear system. The method used to find this mode consists of assigning the dependent variables in our linearized system the form $\hat{A} e^{\lambda t}$, in which \hat{A} is the amplitude and λ is a complex eigenvalue or characteristic exponent. Using Euler's relation, we can show that the real part λ_r of λ represents growth or decay, while the imaginary part λ_i represents the frequency of the branching temporally periodic solution (Pyle, 1987). To indicate a bifurcation point at which there is no growth or decay, we want solutions for which $\lambda_r = 0$. In addition to the case $\lambda_r = 0$, if $\lambda_i = 0$ then a bifurcation to a steady solution occurs. In our problem, such a bifurcation is possible but we did not find any in our analysis. However, if $\lambda_i \neq 0$ then a Hopf bifurcation to a temporally periodic solution results. As noted earlier, a temporally periodic solution is the one of interest in studies of horizontal rolls and is the only one we discuss here.

As stated in Chapter 2, the linear system consists of 14 equations that resulted after the nonlinear terms were neglected. These 14 equations can be decoupled into two

independent systems, one with eight equations and the other with six. Since the latter system has only dissipation terms that do not contribute to the exchange of stability, it cannot contribute to a bifurcation point and so it can be eliminated from consideration. Thus, the 14 equations reduce to eight. The system can be reduced further by expressing the spectral components in terms of complex variables (Pyle, 1987). The result is two decoupled systems in which one is the conjugate of the other: one system gives solutions corresponding to the $-i\lambda_i$ root, and the other gives solutions corresponding to the $+i\lambda_i$ root. The negative set of complex conjugates yields the following linear system represented by the variables $\tilde{\psi}_1$, $\tilde{\psi}_2$, \tilde{T}_1 , and \tilde{T}_2 :

$$\begin{aligned} \dot{\tilde{\psi}}_1 = \dot{\psi}_1 - i\dot{\psi}_2 &= (\text{Re } ia_1 - P b_1)\tilde{\psi}_1 + \text{Re } ia_2 \tilde{\psi}_2 \\ &\quad + id_1 \tilde{T}_1 \quad , \quad (3.1) \end{aligned}$$

$$\begin{aligned} \dot{\tilde{\psi}}_2 = \dot{\psi}_3 - i\dot{\psi}_4 &= (\text{Re } ia_3 - P b_2)\tilde{\psi}_2 + \text{Re } ia_4 \tilde{\psi}_1 \\ &\quad + id_2 \tilde{T}_2 \quad , \quad (3.2) \end{aligned}$$

$$\begin{aligned} \dot{\tilde{T}}_1 = \dot{T}_2 - i\dot{T}_1 &= (\text{Re } ia_5 - b_1)\tilde{T}_1 + \text{Re } ia_6 \tilde{T}_2 \\ &\quad - i(\text{Ra}_e + \varepsilon_1)\tilde{\psi}_1 - i\varepsilon_2 \tilde{\psi}_2 \quad , \quad (3.3) \end{aligned}$$

$$\begin{aligned} \dot{\tilde{T}}_2 = \dot{T}_4 - i\dot{T}_3 &= (\text{Re } ia_7 - b_2)\tilde{T}_1 + \text{Re } ia_8 \tilde{T}_1 \\ &\quad - i\varepsilon_2 \tilde{\psi}_1 - i(\text{Ra}_e + \varepsilon_3)\tilde{\psi}_2 \quad . \quad (3.4) \end{aligned}$$

The coefficients a_i , b_i , and d_i are given in Table 2.1.

To solve the linearized spectral system (3.1)-(3.4), we use the following form of the temporally dependent amplitude coefficients that was noted above:

$$\tilde{\psi}_j = \hat{\psi}_j e^{\lambda t} \quad ; \quad \tilde{T}_j = \hat{T}_j e^{\lambda t} \quad , \quad (j = 1, 2) \quad . \quad (3.5)$$

Substituting the forms (3.5) into (3.1)-(3.4) and taking the temporal derivatives yield four linear equations in $\hat{\psi}_j$ and \hat{T}_j . After canceling the common factor $e^{\lambda t}$, we find that the characteristic exponent λ is the only term remaining on the left side of (3.1)-(3.4). These four equations can be made into homogeneous equations by moving λ to the right side. If the system (3.1)-(3.4) has nontrivial solutions, then two or more of the equations in the system must be dependent so that the determinant of the matrix of coefficients must vanish. The determinant of (3.1)-(3.4) can be written in the following form:

$\tilde{\psi}_1$	$\tilde{\psi}_2$	\tilde{T}_1	\tilde{T}_2	
Re $ia_1 - Pb_1 - \lambda$	Re ia_2	id_1	0	
(A)			(B)	
Re ia_4	Re $ia_3 - Pb_2 - \lambda$	0	id_2	
				= 0
$-i(Ra_e + \epsilon_1)$	$-i\epsilon_2$	Re $ia_5 - b_1 - \lambda$	Re ia_6	
(C)			(D)	
$-i\epsilon_2$	$-i(Ra_e + \epsilon_3)$	Re ia_6	Re $ia_7 - b_2 - \lambda$	

. (3.6)

Expanding the determinant (3.6) gives a fourth-degree characteristic equation in λ , which is given schematically by

$$C_4 \lambda^4 + C_3 \lambda^3 + C_2 \lambda^2 + C_1 \lambda + C_0 = 0 \quad . \quad (3.7)$$

The coefficients C_i are polynomials and are functions of the forcing parameters Re and Ra_e , the aspect ratio a , the Fourier coefficients ε_i , Λ_i and Γ_i (which depend on the domain height z_T), the wavenumbers q and n , and the Prandtl number P . The coefficients C_i are complicated and lengthy. To obtain their expressions, we used the symbolic manipulator CFORMAC, which is available on the IBM 3090 at Penn State. After the determinant is expanded, CFORMAC allows us to find the coefficients that multiply a designated variable. Appendix A shows a portion of the commands that were used to find the coefficients in the (3.12), which is derived from (3.7).

3.2 The Hopf Bifurcation Points

Since we seek values of the forcing rates for which a temporally periodic solution emanates from the conductive one, a signal for a Hopf bifurcation must be introduced into the characteristic equation (3.7). The Hopf

Bifurcation Theorem states that a temporally periodic solution emanates from a steady solution when a complex conjugate pair of characteristic exponents crosses the imaginary axis with nonzero speed (Marsden and McCracken, 1976; Haack-Hirschberg, 1988). As the forcing rate approaches its critical value, the real part of the exponent λ_r vanishes, and the imaginary part λ_i gives the limiting dimensionless frequency ω_0^* (as Ra_e approaches Ra_{ec} and Re approaches Re_c) of the periodic solution (Pyle, 1987). A Hopf bifurcation, therefore, is signaled in equation (3.7) by setting

$$\lambda = i\lambda_i = i\omega_0^* . \quad (3.8)$$

This substitution produces a fourth-degree polynomial equation in ω_0^* containing both real and imaginary terms. The resulting equation is expressed schematically as

$$R + iI = 0 , \quad (3.9)$$

in which the imaginary part I is a cubic equation and the real part R is a quartic equation, given respectively by

$$\begin{aligned} I = & A_i \omega_0^{*3} + B_i Re_c \omega_0^{*2} + (D_i Re_c^2 + C_i + Ra_{ec} F_i) \omega_0^* \\ & + G_i Re_c^3 + H_i Ra_{ec} Re_c + E_i Re_c = 0 , \quad (3.10) \end{aligned}$$

$$\begin{aligned}
R = & J_r \omega_o^{*4} + K_r Re_c \omega_o^{*3} + (L_r Re_c^2 + M_r + N_r Ra_{ec}) \omega_o^{*2} \\
& + (Q_r Re_c^3 + S_r Ra_{ec} Re_c + T_r Re_c) \omega_o^* + U_r Re_c^4 \\
& + (V_r + W_r Ra_{ec}) Re_c^2 + X_r Ra_{ec}^2 \\
& + Y_r Ra_{ec} + Z_r = 0 \quad . \quad (3.11)
\end{aligned}$$

The forcing values Ra_e and Re have been set to their critical values Ra_{ec} and Re_c , since these are the values at the Hopf bifurcation point that signal branching solutions having frequency ω_o^* .

Our goal in this analysis is to find the minimum values of the forcing rates Ra_{ec} and Re_c that give a Hopf bifurcation. To accomplish this goal, we must choose the variables that will be expressed in terms of the others. Both equations (3.10) and (3.11) are functions of Ra_{ec} , ε_i , Re_c , and ω_o^* , as well as the response parameters a , Λ_i , Γ_i , q , n and P ; the dependence on z_T is incorporated implicitly into the values of Λ_i , Γ_i and ε_i . However, if we choose values for Re_c and the response parameters, then there are two unknowns in two equations: Ra_{ec} and ω_o^* . Since (3.10) is linear in Ra_{ec} , we may easily find an expression for it. This value of Ra_{ec} is the one required to make the imaginary part of the characteristic equation vanish and it

is given by

$$Ra_{ec} = - \left[\frac{A_i \omega_o^{*3} + B_i Re_c \omega_o^{*2} + (D_i Re_c^2 + C_i) \omega_o^* + G_i Re_c^3 + E_i Re_c}{H_i Re_c + F_i \omega_o^*} \right] \quad (3.12)$$

This expression for Ra_{ec} is then substituted into (3.11) to make the real part of the characteristic equation vanish. The result is a sixth-degree equation in both ω_o^* and Re_c . Finally, we solve for ω_o^* as functions of Re_c and the response parameters. This final equation is named the Hopf bifurcation equation and is given by

$$\begin{aligned} d_{13} \omega_o^{*6} + d_{12} Re_c \omega_o^{*5} + (d_{11} Re_c^2 + d_{10}) \omega_o^{*4} + (d_9 Re_c^3 + d_8 Re_c) \omega_o^{*3} \\ + (d_7 Re_c^4 + d_6 Re_c^2 + d_{14}) \omega_o^{*2} + (d_5 Re_c^5 + d_4 Re_c^3 + d_3 Re_c) \omega_o^* \\ + (d_2 Re_c^6 + d_1 Re_c^4 + d_0 Re_c^2) = 0 \quad (3.13) \end{aligned}$$

in which

$$d_k = f_k(\Lambda_i, \Gamma_i, \varepsilon_i, a, q, n, P) \quad , \quad \begin{cases} k=0, \dots, 14 \\ i=1, 2, 3 \end{cases} \quad (3.14)$$

Before obtaining the ω_o^* roots, we must find numerical values for each of the coefficients d_k in addition to specifying each value of Re_c . We recall from (2.62)-(2.67) that

$$\left. \begin{aligned} \Lambda_i &= g_i(U_i, V_i, \beta) \\ \Gamma_i &= h_i(US_i, VS_i, \beta) \end{aligned} \right\}, \quad i=1,2,3, \quad (3.15)$$

where the integrals U_i , V_i , US_i and VS_i of the wind are defined in Table 2.3. Thus we must specify the following quantities: values for z_T , q , n and P ; an idealized or observed wind profile to obtain values for U_i , V_i , US_i , and VS_i ; an idealized or observed temperature profile to obtain values for ε_i ; and appropriate ranges for the values of Re_c , β and a . For given values of Re_c , β and a , the solutions to (3.13) yield six complex roots for ω_0^* . Of the six possible roots, only real ones are acceptable. We find numerically acceptable results by requiring that the imaginary root be no larger than 10^{-9} times the real root and that the residual in (3.13) be no larger than 10^{-9} times the largest coefficient. The critical effective Rayleigh number Ra_{ec} for each combination of Re_c , β , a and ω_0^* may now be found by substituting the acceptable value of ω_0^* into the imaginary part of the characteristic equation (3.12). Because this equation is linear in Ra_{ec} , we find that expressing the Hopf bifurcation equation in terms of ω_0^* permits unambiguous identification of the common roots to (3.10)-(3.11). Finally, it is important to note that we may now sort the calculated values of Ra_{ec} from the smallest or preferred, to the largest values for each value of Re_c . This final step allows clear identification of the

preferred modes and saves a tremendous amount of research time.

The values of Re_c and Ra_{ec} describe the minimum rates of dynamic and thermodynamic forcing needed to drive roll circulations and they depend upon the geometry of the rolls that are described by the response parameters a and β (and z_T via the Fourier coefficients Λ_i , Γ_i and ϵ_i). Numerous transition curves resulting from various combinations of a and β cross the line where Re_c is constant; three such possible curves are depicted in Figure 3.2. However, only the curve containing the smallest value $Ra_{c(\min)}$ of Ra_c yields the relevant preferred Hopf bifurcation point because the atmosphere generally evolves from a stable to an unstable state by reaching the smallest values of Ra_c and Re_c first. Similarly, the preferred Hopf bifurcation point occurs at a unique minimum value $Re_{c(\min)}$ of Re_c that is on a line of constant Ra_c . As before, we subtract Ra_i from Ra_{ec} to obtain the transition curve in (Ra, Re) -parameter space. The dotted line in Figure 3.2 shows the curve given by the minimum values of Ra_c and their corresponding values of Re_c . This curve is often called a preferred or expected curve because it marks the transition in (Ra, Re) -parameter space between the region where rolls are possible and the region where they are not; it is preferred because this curve is the first one encountered in the transition between solutions.

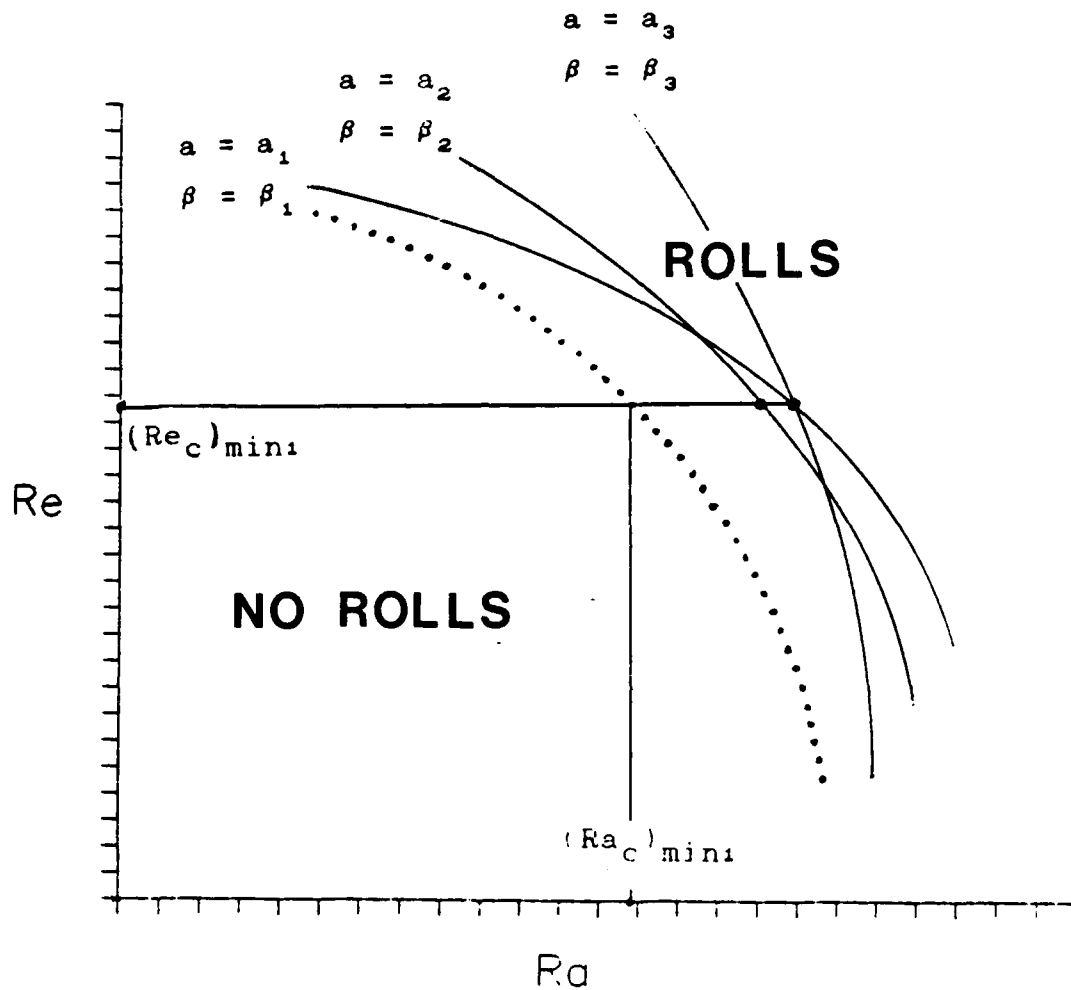


Fig. 3.2 Schematic Illustration of Three Hopf Bifurcation Curves. Each curve is associated with fixed values of aspect ratio a , orientation angle β and domain height z_T . Points on the transition curve (dotted line) represent the minimum values of both Ra_c and Re_c (from Haack-Hirschberg, 1988).

Figure 3.3 isolates the expected transition curve. The state of the atmosphere can evolve from the region where rolls do not form (left of a curve) to the region where they can form (right of a curve) along an infinite number of paths. The path that the atmosphere takes depends on the evolution of the dynamic and thermodynamic forcing rates. For fixed values of z_T , the values of a and β given by the intersection of the paths with the expected transition curve gives the preferred values of the roll geometry for a roll of depth z_T . If the atmospheric forcing rates Re and Ra are to the right of the transition curve and evolve along path 1, then at the crossing point on the curve, horizontal rolls will develop having roll characteristics given by $a_p = a_1$ and $\beta_p = \beta_1$; along path 3, rolls will develop having characteristics $a_p = a_3$ and $\beta_p = \beta_3$. Thus by knowing how the atmospheric values of Re and Ra have evolved, we may determine if roll circulations are possible and if so, what their preferred roll characteristics will be. If the atmospheric values far exceed the values on the transition curve, as shown by paths 2 and 3 in Figure 3.3, then the expected roll geometry is uncertain. However, the geometry of the rolls may be estimated by using the values a_p and β_p given by the closest Hopf bifurcation point. Here, the expected roll geometry would be approximated by the values of a_2 and β_2 for path 2 and by the values a_3 and β_3 for path 3. The

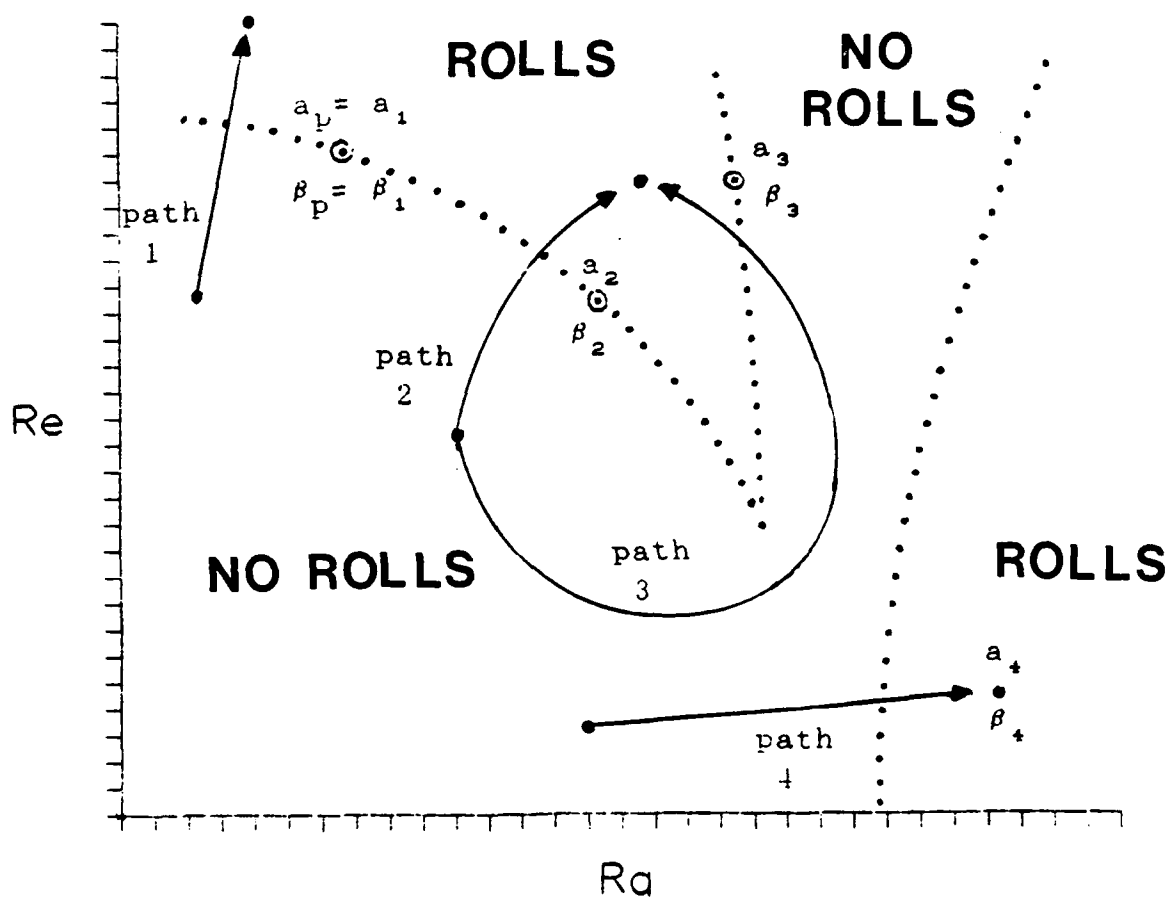


Fig. 3.3 Schematic Illustration of Possible Hopf Bifurcation Curves Associated with Fig. 3.2. For a given value of Re_c , the preferred set of roll parameters a_p and β_p is the one that yields the minimum value of Ra_c . For a particular instability mode, this curve denotes the transition in (Ra, Re) -parameter space between the roll-free state and the roll state (after Haack-Hirschberg, 1988).

accuracy of this approximation is related to the rate of change of a_p and β_p along the transition curve.

In our numerical analysis of the thermal and inflection point modes, we find that it is often difficult to determine where one mode ends and another begins in (Ra, Re) -parameter space. It appears that a generally smooth or at least ambiguously located, transition occurs between the modes. However, for a constant value of Re_c we can sometimes find portions of our ordered list of Ra_c values in which an abrupt change in Ra_c or another parameter value occurs that signals the end of one mode and the beginning of another mode. The corresponding location in (Ra, Re) -parameter space depicts the right-most side of the mode demarcating the largest value of Ra_c for which that mode can occur. When this right-most side is impossible to identify, we indicate only the left-most preferred transition curve for each mode (see Fig. 3.3).

We have derived a governing Hopf bifurcation equation (3.13) for the spectral equations developed in Chapter 2. In Chapters 4 and 5, this equation will be used to identify the roll modes that may develop from an idealized and two observed wind profiles. In the next section we will confirm that the special case $\varepsilon_i \neq 0$ contains the separate special cases of the inflection point and thermal instability mechanisms given by Haack-Hirschberg (1988), and we will discuss the case $\varepsilon_i \neq 0$ in a calm environment.

3.3 Special Cases

The stability results of the linear spectral model (3.1)-(3.4) can be verified by checking that the results of special, limiting cases agree with those of previous, simpler roll circulation models. The model derived by Haack-Hirschberg (1988) represents the two dominant instability mechanisms in one system. She compares her two single-wavenumber thermodynamic instability mechanisms with those occurring in a model of moist convection in a sheared environment (Shirer, 1986). She then isolates the pure inflection point instability mechanism and compares it with the instability results obtained by Stensrud and Shirer (1988) in a neutral environment. Both of these studies allow analytic and numerical comparisons. The results from Haack-Hirschberg (1988) confirmed that the dynamic and thermodynamic instabilities were the same as those obtained by Stensrud and Shirer (1988) and Shirer (1986). To prove that our model accurately represents these two instability mechanisms, we must compare the linear case ($\varepsilon_i = 0$) and the nonlinear case ($\varepsilon_i \neq 0$) with the linear case given by the Haack-Hirschberg (1988) dynamic and thermodynamic model.

3.3.1 Pure Inflection Point Case

The pure inflection point instability mechanism is driven by dynamic forcing alone. Thus we may eliminate the thermodynamic forcing by setting both the effective Rayleigh number Ra_e and the harmonic components ε_i to zero in (3.9), which together imply neutral static stability. After performing this step, we obtain the same Hopf bifurcation equation as that found by Haack-Hirschberg (1988); it is given by

$$\text{Re}_c^2 \left[(a_1 - a_3)^2 b_1 b_2 + (a_2 a_4) (b_1 + b_2)^2 \right] + P^2 (b_1 + b_2)^2 b_1 b_2 = 0 \quad , \quad (3.15)$$

and the limiting frequency is given by

$$\omega_0^* = \text{Re}_c \left[\frac{a_1 (a^2 + q^2) + a_3 (a^2 + n^2)}{(2a^2 + q^2 + n^2)} \right] \quad . \quad (3.16)$$

In this case the limiting frequency ω_0^* is a function of the product of Re_c and the weighted average of the Fourier coefficients a_1 and a_3 . Thus ω_0^* is a function of the relative contributions of the cross-roll wind $U^*(z^*)$ and cross-roll wind shear $\partial U^*/\partial z^*$. Since b_1 and b_2 are positive, the only way a real value of Re_c can occur is for $a_2 a_4 < 0$. Because this product can be negative only

when $q \neq n$, then it follows that two vertical wavenumbers q and n are needed in the model in order to capture the inflection point instability mechanism (Stensrud, 1985).

We use the results from the analytical version of the inflection point special case as a standard against which we may check the results from the full model. For given wind and temperature profiles and set values of the parameters Re_C , z_T , q , n and P , the values of Ra_{ec} , a_p , β_p , and ω_0^* obtained numerically should assume values very close to those given analytically. In addition, the numerical results obtained from the $\varepsilon_i \neq 0$ case should assume reasonable values compared with those obtained from the $\varepsilon_i = 0$ case. The differences that we get from this special case are assumed to be due to the effect of wind shear within the inversion. We use idealized wind and temperature profiles to make this numerical comparison in Chapter 4.

3.3.2 Single-Wavenumber Thermal Special Cases

In this section we verify that the Hopf bifurcation equation of the thermal model obtained with the harmonic portion ε_i of the temperature profile included is analogous to that obtained by Haack-Hirschberg (1988). The thermal case can be isolated from the inflection point case because the use of only one vertical wavenumber filters the

inflection point instability mechanism; but as we will see, it does not filter the thermal one. When the mixed wavenumber terms Γ_2 and Λ_2 are assumed to vanish, Haack-Hirschberg (1988) shows that her full model contains two single-wavenumber thermal q- and n-submodels. These submodels are identical except in vertical wavenumber. Here, in order to decouple the two submodels, we must set $\varepsilon_2 = 0$ in the full model as an additional requirement. The remaining ε_1 and ε_3 terms act to modify the resulting critical value of Ra_e .

A determinant representing each of the single-wavenumber thermal q- and n-submodels is given by re-expressing (3.6) as

$$\begin{vmatrix}
 \tilde{\psi}_1 & \tilde{T}_1 & \tilde{\psi}_2 & \tilde{T}_2 \\
 \text{Re } ia_1 - Pb_1 - \lambda & id_1 & & \\
 (E) & & & \\
 -i(Ra_e + \varepsilon_1) & \text{Re } ia_5 - b_1 - \lambda & & 0 \\
 0 & & \text{Re } ia_3 - Pb_2 - \lambda & id_2 \\
 & & (F) & \\
 & & -i(Ra_e + \varepsilon_3) & \text{Re } ia_7 - b_2 - \lambda
 \end{vmatrix}
 = 0, \quad (3.17)$$

where a_2 , a_4 and a_6 are set to zero because they depend only on Λ_2 and Γ_2 . Upon completing the stability analysis for each submodel, we obtain similar equations for the

critical effective Rayleigh numbers and the limiting frequencies of the periodic solutions. From the stability analysis of $|E| = 0$, we obtain

$$Ra_{ec} = Re_c^2 \left[\frac{P(a_5 - a_1)^2}{d_1(P+1)^2} \right] + \frac{P b_1^2}{d_1} - \varepsilon_1, \quad (3.18)$$

and

$$\omega_o^* = Re_c \frac{(a_1 + a_5 P)}{(P+1)}, \quad (3.19)$$

governing the thermal q-submodel. From a stability analysis of $|F| = 0$, we obtain

$$Ra_{ec} = Re_c^2 \left[\frac{P(a_7 - a_3)^2}{d_1(P+1)^2} \right] + \frac{P b_2^2}{d_2} - \varepsilon_3, \quad (3.20)$$

and

$$\omega_o^* = Re_c \frac{(a_3 + a_7 P)}{(P+1)}, \quad (3.21)$$

governing the thermal n-submodel.

After substituting the definitions of a_i , b_i and d_i into (3.18) and (3.19), we obtain the following Hopf bifurcation and frequency equations for the q-submodel:

$$Ra_{ec} = Re_c^2 \left[\frac{p^2 \Gamma_1^2}{(a^2 + q^2)(P + 1)^2} \right] + \frac{(a^2 + q^2)^3}{a^2} - \varepsilon_1, \quad (3.22)$$

and

$$\omega_o^* = Re_c P \left[\Lambda_1 + \frac{\Gamma_1}{(a^2 + q^2)(P + 1)} \right]. \quad (3.23)$$

Similar substitutions for the thermal n-submodel yield

$$Ra_{ec} = Re_c^2 \left[\frac{p^2 \Gamma_3^2}{(a^2 + n^2)(P + 1)^2} \right] + \frac{(a^2 + n^2)^3}{a^2} - \varepsilon_3, \quad (3.24)$$

and

$$\omega_o^* = Re_c P \left[\Lambda_3 + \frac{\Gamma_3}{(a^2 + n^2)(P + 1)} \right]. \quad (3.25)$$

Since the critical Rayleigh numbers (3.22) and (3.24) differ only in vertical wavenumber, we combine them into the following general wavenumber Hopf bifurcation and frequency equations:

$$Ra_{ec} = Re_c^2 \left[\frac{p^2 \Gamma_m^2}{(a^2 + m^2)(P + 1)^2} \right] + \frac{(a^2 + m^2)^3}{a^2} - \varepsilon_m, \quad (3.26)$$

and

$$c_o^* = Re_c P \left[\Lambda_m + \frac{\Gamma_m}{(a^2 + m^2)(P + 1)} \right] , \quad (3.27)$$

in which m represents a general wavenumber. The generalized Fourier coefficients Λ_m and Γ_m become

$$\left. \begin{aligned} \Lambda_m &= \Lambda_1 \\ \Gamma_m &= \Gamma_1 \end{aligned} \right\} \text{and } \varepsilon_m = \varepsilon_1 \text{ when } m = q ;$$

$$\left. \begin{aligned} \Lambda_m &= \Lambda_3 \\ \Gamma_m &= \Gamma_3 \end{aligned} \right\} \text{and } \varepsilon_m = \varepsilon_3 \text{ when } m = n . \quad (3.28)$$

As noted by Shirer (1986), owing to the dynamic effects, the smallest critical Rayleigh number occurs in two special situations giving $\Gamma_m = 0$: the first is when there is an appropriately placed inflection point in the cross-roll wind component U^* so that $\Gamma_m \propto \partial U^* / \partial z^*$ vanishes. The second special situation occurs for a unidirectional wind profile. For example, when Γ_m is integrated by parts and rotated into the reference coordinate system using (2.62), $\Gamma_m = 0$ becomes

$$\Gamma_m = US_m \sin(\beta_p) - VS_m \cos(\beta_p) = 0 . \quad (3.29)$$

Equation (3.29) is satisfied if, for example, $US_m = 0$ and $\beta_p = 90^\circ$. For the single-wavenumber thermal special cases, (3.29) produces preferred values of the orientation angle

β_p that minimize the effects of the cross-roll component of the wind shear $\partial U^*/\partial z^*$. These preferred angles are given by

$$\tan(\beta_p) = \frac{VS_m}{US_m} . \quad (3.30)$$

For the preferred orientation angle cases, the Hopf bifurcation and frequency equations (3.26)-(3.27) reduce to

$$Ra_{ec} = \frac{(a^2 + m^2)^3}{a^2} - \varepsilon_m , \quad (3.31)$$

$$Ra_c = \frac{(a^2 + m^2)^3}{a^2} - \varepsilon_m - Ra_i = Ra_{ec} - Ra_i , \quad (3.32)$$

$$\omega_o^* = Re_c P \Lambda_m . \quad (3.33)$$

When $\varepsilon_m = 0$, the two thermal submodels reduce to those of Haack-Hirschberg (1988). Thus the thermal instability mechanism is retained in the full model. Significantly, just as a condition on Γ_m gives a preferred orientation angle, a condition on ε_m will give the preferred circulation depth z_{Tp} . From (3.32) it is clear that for convection to occur, then the critical value of the forcing rate Ra_c must be larger than the critical value Ra_{ec} because the heating rate must overcome the effect of the

inversion term $Ra_i < 0$. Depending on the form of $G(z)$ in (2.8), ε_m may be either positive or negative. So, as we stated in Chapter 2, the harmonic component of the vertical temperature profile may act as an energy source or sink and thus decrease or increase the value of Ra_{ec} . However, as we will see in Chapters 4 and 5, the magnitude of the harmonic term ε_m is on the order of 10^2 times the other term in (3.31) and its sign is usually negative. Therefore, the value of Ra_{ec} can be approximated by using this value of the (negative) ε_m term.

When a well-mixed layer is capped by an inversion, as shown in Fig. 2.1, then $\varepsilon_m = 0$ and $Ra_i = 0$ holds for all heights z_T that are less than the height z_i of the inversion base, while $Ra_i < 0$ and $\varepsilon_m < 0$ hold for all $z_T \geq z_i$. From (3.32) we conclude that the deepest circulation giving the minimum value of Ra_c occurs when $z_T = z_i$. Thus the height of the inversion base caps the roll circulations in the purely convective case, as expected.

The preferred aspect ratio is found by setting the derivative $\partial(Ra_c)/\partial a^2$ to zero when $Ra_i = 0$ and $\varepsilon_i = 0$. The expression for the preferred value of a_p is therefore given by

$$a_p^2 = \frac{m^2}{2} \quad (3.34)$$

After obtaining a_p , we find the smallest critical

Rayleigh number for any given wavenumber m by using (3.32). Because the smallest vertical wavenumber produces the smallest value of Ra_C , we choose $m = q = 1$. Hence we obtain the value $a_p = \sqrt{2}/2 \approx 0.707$ from (3.34). The corresponding smallest value of Ra_C is therefore $(Ra_C)_{\min} = 6.75$; should we consider the nonpreferred thermodynamic case, we get $(Ra_{ec})_{\min} = 6.75 - \epsilon_1$. Wavenumber one is the gravest mode and so it is always the preferred wavenumber for any thermal case. Therefore, $q < n$ must always equal one. Wavenumber n , however, may be any integer not equal to one. For the case $n = 2$ we obtain the values $a_p \approx 1.41$ and $(Ra_C)_{\min} = 108.00$, and for $n = 3$, we obtain the values $a_p \approx 2.21$ and $(Ra_C)_{\min} = 546.75$.

Here, we have seen that allowing only single-wavenumber representations in the Hopf bifurcation equation (3.13) eliminates the dynamic energy source and separates the full model into two single-wavenumber thermal ones. In the full model we obtain values of $(Ra_{ec})_{\min}$, a_p , β_p and ω_o^* for given wind and temperature profiles and set of parameters Re_C , z_T , q , n and P ; by varying the magnitudes of both Re_C and z_T we obtain their preferred values as well. We compare these values from the full model with those given by the single-wavenumber analytic equations (3.31)-(3.33). In Chapters 4 and 5 we perform this numerical verification for idealized and observed wind and temperature profiles.

3.3.3 Steady Pure Thermal Special Case

The final special case that we consider is one that gives the critical effective Rayleigh number for boundary layer convection occurring in an environment with no background wind ($U^*(z) = 0$) but with a temperature inversion that includes all three harmonic portions ($\varepsilon_i \neq 0$) of the temperature profile. Physically, in this case, the convection would not be organized into rolls or cloud streets; instead they would take on a tessellated pattern and our two-dimensional model would predict that there is no preferred orientation angle β_p . Because $U^*(z^*) = 0$, the critical Reynolds number Re_c must equal zero as well. In addition, without a background wind, the rolls cannot propagate through the domain. Although a Hopf bifurcation is in principle possible (e.g., for gravity waves), we did not find any during the numerical computations. With no background wind, the roll frequency ω_0^* must also equal zero, and this forces the imaginary part of the characteristic exponent λ_i to vanish.

Thus we consider bifurcation to steady convection so that the characteristic exponent λ_r equals zero. The determinant (3.6) for the special case of $Re_c = \lambda = 0$ and $\varepsilon_i \neq 0$ is given by

$\tilde{\psi}_1$	$\tilde{\psi}_2$	\tilde{T}_1	\tilde{T}_2
$-P b_1$	0	id_1	0
0	$-Pb_2$	0	id_2
$-i(Ra_e + \varepsilon_1)$	$-i\varepsilon_2$	$-b_1$	0
$-i\varepsilon_2$	$-i(Ra_e + \varepsilon_3)$	0	$-b_2$

= 0 . (3.35)

Upon expanding the determinant (3.35), we obtain the following quadratic bifurcation equation in Ra_{ec} :

$$\begin{aligned}
 Ra_{ec}^2 (d_1 d_2) + Ra_{ec} (\varepsilon_1 d_1 d_2 + \varepsilon_3 d_1 d_2 - P b_1^2 d_2 - P b_2^2 d_1) \\
 - \varepsilon_1 P b_2^2 d_1 - \varepsilon_3 P b_1^2 d_2 + \varepsilon_1 \varepsilon_3 d_1 d_2 \\
 + P^2 b_1^2 b_2^2 - \varepsilon_2^2 d_1 d_2 = 0 . \quad (3.36)
 \end{aligned}$$

When the ε_2 term equals zero in (3.36), we obtain the same expressions for Ra_{ec} as those given by (3.31) and (3.32). When $\varepsilon_2 \neq 0$, it is easy to show that the discriminant of (3.36) is positive, implying that critical effective Rayleigh numbers exist for any inversion. Moreover, for the case of an inversion capping a well-mixed layer, the minimum value of Ra_c is given by $Ra_i = 0$ and $\varepsilon_i = 0$ so that the preferred value z_{Tp} of the circulation depth is the height z_i of the inversion base (Section 3.3.2).

In this chapter we have seen that our full model,

which includes an arbitrary vertical temperature profile, can be reduced to several special analytic cases. These analytic cases are analogous to those obtained by Haack-Hirschberg (1988). Not only do the special cases provide useful information about the dynamic and thermal instability mechanisms, they also provide a basis upon which to check the numerical results that are obtained from the full model. We will use the values obtained from these special case equations to identify the inflection point and thermal modes within the full model results presented in the next chapter.

Chapter 4
MODEL RESULTS USING IDEALIZED
WIND AND TEMPERATURE PROFILES

Up to this point, we have developed a system of spectral equations that models boundary layer rolls. We then derived its resulting Hopf bifurcation polynomial (3.13) giving the critical values for the various roll modes. After examining (3.13), we learned that its solutions were dependent on the background wind and temperature profiles (via their Fourier coefficients), the orientation angle, the cell aspect ratio, the Prandtl number and the vertical wavenumbers of the circulation. In this chapter we study how idealized background temperature and wind profiles affect the solutions of (3.13). The idealized profiles serve to specify the values of the Fourier coefficients Λ_i , Γ_i and ϵ_i . To determine how the temperature and wind profiles affect the solutions of (3.13), we must solve it using a range of values for some of the parameters listed above. To resolve all of the known features of the billows profile, we have found it necessary to use a high resolution grid defined by incrementing Re_c every 2 units, β every 5° and a every 0.05. Together with the Fourier coefficients, this range of variables allows us to adequately find the various transition curves in (Ra, Re) -parameter space.

The results using idealized profiles provide a conceptual framework guiding the interpretation of the results for more complicated, observed profiles. Here, we find it convenient to consider idealized wind profiles having characteristics that approximate the wind in the boundary layer and produce modes that have been documented by others. We will check our model results using an idealized billows wind profile that supports the inflection point instability mechanism (Brown, 1980). We are not aware of other researchers who have studied the effects of a generalized wind profile interacting with an arbitrary vertical temperature profile on horizontal rolls that do not interact with the free atmosphere. Hence we can make only qualitative comparisons with some work by others pertaining to certain aspects of our problem. For example, Brown (1972) studied Ekman profiles in stratified boundary layers and has shown that the inflection point mode exists only near neutral stratification; Asai (1972) provides evidence of the existence of an inflection point mode in slightly unstable stratification. Thus we must rely mostly on analytic checks to determine model accuracy. Once we have verified the numerical results for the linear or nonharmonic temperature profile case ($\varepsilon_i = 0$) with that of Haack-Hirschberg (1988), we will determine the effects of a nonlinear or harmonic temperature profile ($\varepsilon_i \neq 0$) that contains significant wind shear in a capping inversion.

We find that our model produces all of the expected roll modes: the shear mode (Haack-Hirschberg, 1988) that occurs only in a stably stratified regime ($Ra_{ec} < 0$); the inflection point mode that is characterized by a neutral stratification ($Ra_{ec} = 0$); and the single-wavenumber q - and n -thermal modes that are restricted to the statically unstable regime ($Ra_{ec} > 6.75$). In this chapter, we investigate the dominant characteristics of each of the instability modes for the complete two-harmonic case with general thermal and dynamic forcing rates. However, we will not examine the single-wavenumber n -thermal mode since we know it displays the same qualitative features as the physically more relevant single-wavenumber q -thermal mode that we do investigate (Haack-Hirschberg, 1988). In the next chapter, we use the results obtained from the idealized profiles to help identify the modes that likely existed on two days of the 1981 KonTur field experiment.

4.1 Billows Wind Profile

In this section we develop a simple unidirectional billows wind profile that is known to support the inflection point mode (Brown, 1980). We choose a wind profile for which the inflection point may be located at any height z_{ip}^* in the domain and at any value e of $V^*(z_{ip}^*)$. Such a billows profile is given by

$$U^*(z^*) = 0 \quad , \quad (4.1)$$

$$V^*(z^*) = d(z^* - z_{ip}^*)^{1/3} + e \quad . \quad (4.2)$$

To satisfy the restriction (2.64) for the dimensionless form for the wind, the variable d must obey

$$d = (1 - e)(\pi - z_{ip}^*)^{-1/3} \quad , \quad (4.3)$$

Substituting (4.3) into (4.2) gives the following form for a billows profile having an arbitrary inflection point height:

$$U^*(z^*) = 0 \quad , \quad (4.4)$$

$$V^*(z^*) = (1 - e) \left[\frac{(z^* - z_{ip}^*)}{(\pi - z_{ip}^*)} \right]^{1/3} + e \quad (4.5)$$

Although e is defined as the value of $V^*(z_{ip}^*)$, we may also choose e so that $V(0) = 0$ (see Section 4.3).

4.2 Idealized Temperature Profile

To complete the idealized model, we specify a simple vertical temperature profile. Adding this degree of freedom to our spectral model allows us to examine the

effect of a temperature inversion on the transition curves and roll characteristics given by the above simple unidirectional billows wind profile. The temperature profile consists of two parts. In the part of the atmosphere below the capping inversion, the temperature decreases linearly at the dry adiabatic rate. Within the inversion, the temperature increases linearly at a rate we can specify arbitrarily. A dimensional profile depicting such a vertical temperature structure is given by

$$T_o(z) = T_{oo} - \Delta_z T(\text{dry}) z/z_T + \delta \Delta_z T(\text{inv}) (z - z_i)/(z_T - z_i) , \quad (4.6)$$

in which T_{oo} is the temperature at the surface $z = 0$, $\Delta_z T(\text{dry})/z_T$ is the dry adiabatic lapse rate, the height of the inversion base is given by z_i , $\Delta_z T(\text{inv})$ is the total temperature change within the inversion and δ is given by

$$\begin{aligned} \delta &= 0 , & 0 < z < z_i , \\ \delta &= 1 , & z_i \leq z \leq z_T . \end{aligned} \quad (4.7)$$

The third term on the right of (4.6) is an analytic version of the $H(z)$ term in (2.7) and $\Delta_z T(\text{dry})/z_T$ is a version of $\Delta_z T(\text{air})/z_T$ in (2.7). The Fourier coefficients ϵ_i in this case are specified using (2.56)-(2.58) by

$$\varepsilon_1 = -\frac{\gamma^*(\text{inv})}{\pi} \left[(\pi - z_i^*) + \frac{\sin(2qz_i^*)}{2q} \right], \quad (4.8)$$

$$\varepsilon_2 = -\frac{\gamma^*(\text{inv})}{\pi} \left[\frac{1}{(n+q)} \sin((n+q)z_i^*) - \frac{1}{(n-q)} \sin((n-q)z_i^*) \right], \quad (4.9)$$

$$\varepsilon_3 = -\frac{\gamma^*(\text{inv})}{\pi} \left[(\pi - z_i^*) + \frac{\sin(2nz_i^*)}{2n} \right], \quad (4.10)$$

in which $\gamma^*(\text{inv})$ is the dimensionless version of the lapse rate $\gamma(\text{inv}) = \Delta_z T(\text{inv}) / (z_T - z_i)$ in the temperature inversion.

In the next section, we analyze the stability of (3.13) using both the wind profile (4.4)-(4.5) and the temperature profile (4.6)-(4.7). After comparing the linear temperature profile case ($\varepsilon_i = 0$) with that of Haack-Hirschberg (1988), we examine the effect of two statically stable potential temperature profiles ($\varepsilon_i \neq 0$) on the roll modes that are produced by the billows wind profile.

4.3 Stability of the Billows Wind Profile with and without a Capping Inversion

To simulate physically realistic conditions, we would like to locate the inflection point in the wind profile at the same height as that of the base of the temperature inversion since the inversion is where the wind speed usually begins to increase significantly. This situation would allow us to investigate the forcing of rolls by the shear within the inversion. However, for the wind profile (4.4)-(4.5), our model does not yield an inflection point mode for $z_{ip}^* > 0.6\pi$. This effect is consistent with that found by Brümmer and Latif (1985) who show that the inflection point instability becomes more difficult to initiate as the level of the inflection point moves away from the center of the domain. In addition, owing to the numerical procedure we used, we find only spurious results when $z_{ip}^* = 0.5\pi$. Therefore, we choose an inflection point level at the upper limit of the acceptable range, which is $z_{ip}^* = 0.6\pi$. For this value of z_{ip}^* , $e = 0.534$ produces the condition $V^*(0) = 0$ and $d = -0.479$. We place the base of the inversion z_i in the temperature profile (4.6)-(4.7) at $z_i = 0.8z_T$ ($z_i^* = 0.8\pi$) and set the inversion strength $\gamma(inv) = \Delta_z T(inv)/(z_T - z_i)$ at a moderate value of $5^\circ\text{C}/100\text{ m}$. Figures 4.1 and 4.2 show the potential temperature

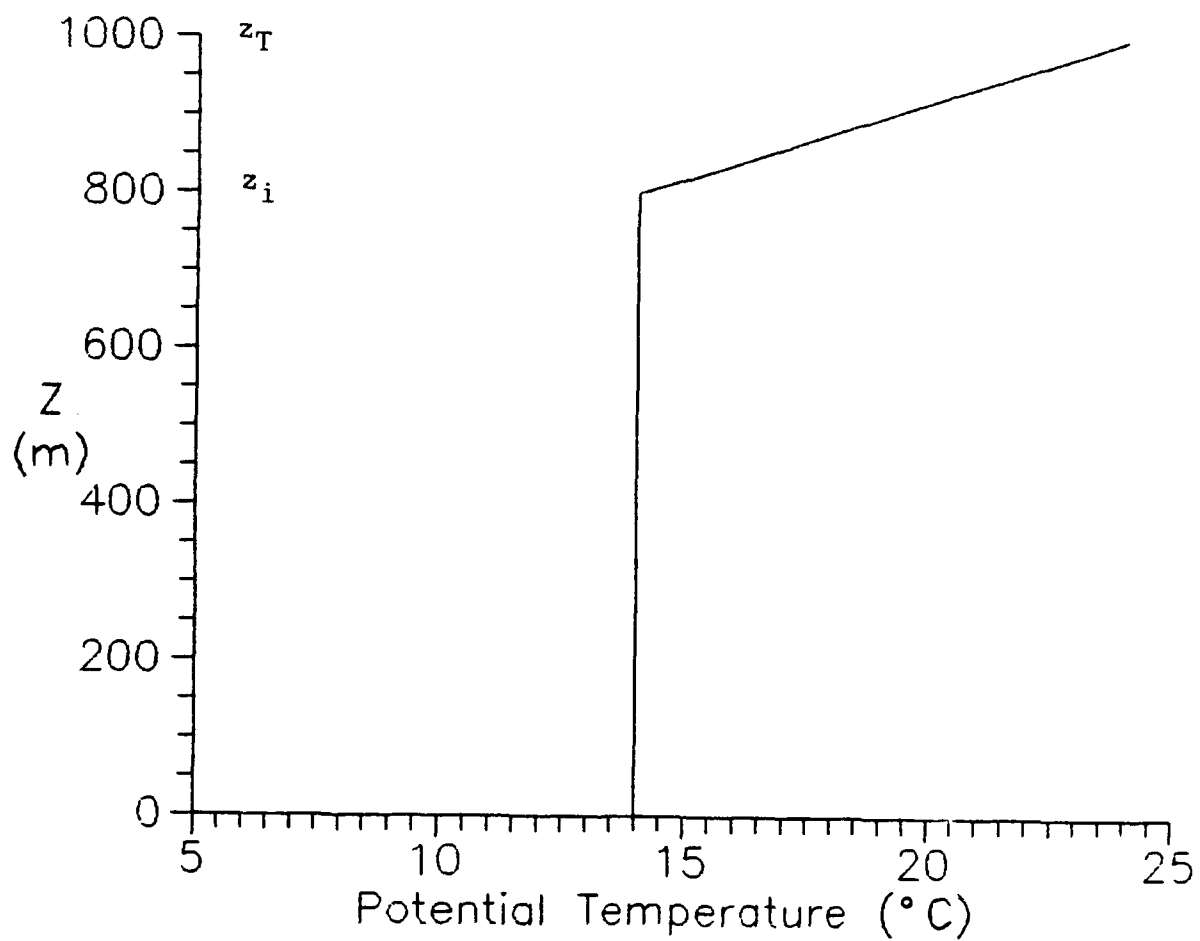


Fig. 4.1 Vertical Profile of the Potential Temperature Used in the Billows Stability Analysis. The temperature decreases linearly at the dry adiabatic lapse rate to the base z_i of the inversion and then increases at the rate $\gamma(\text{inv})$ within the inversion.

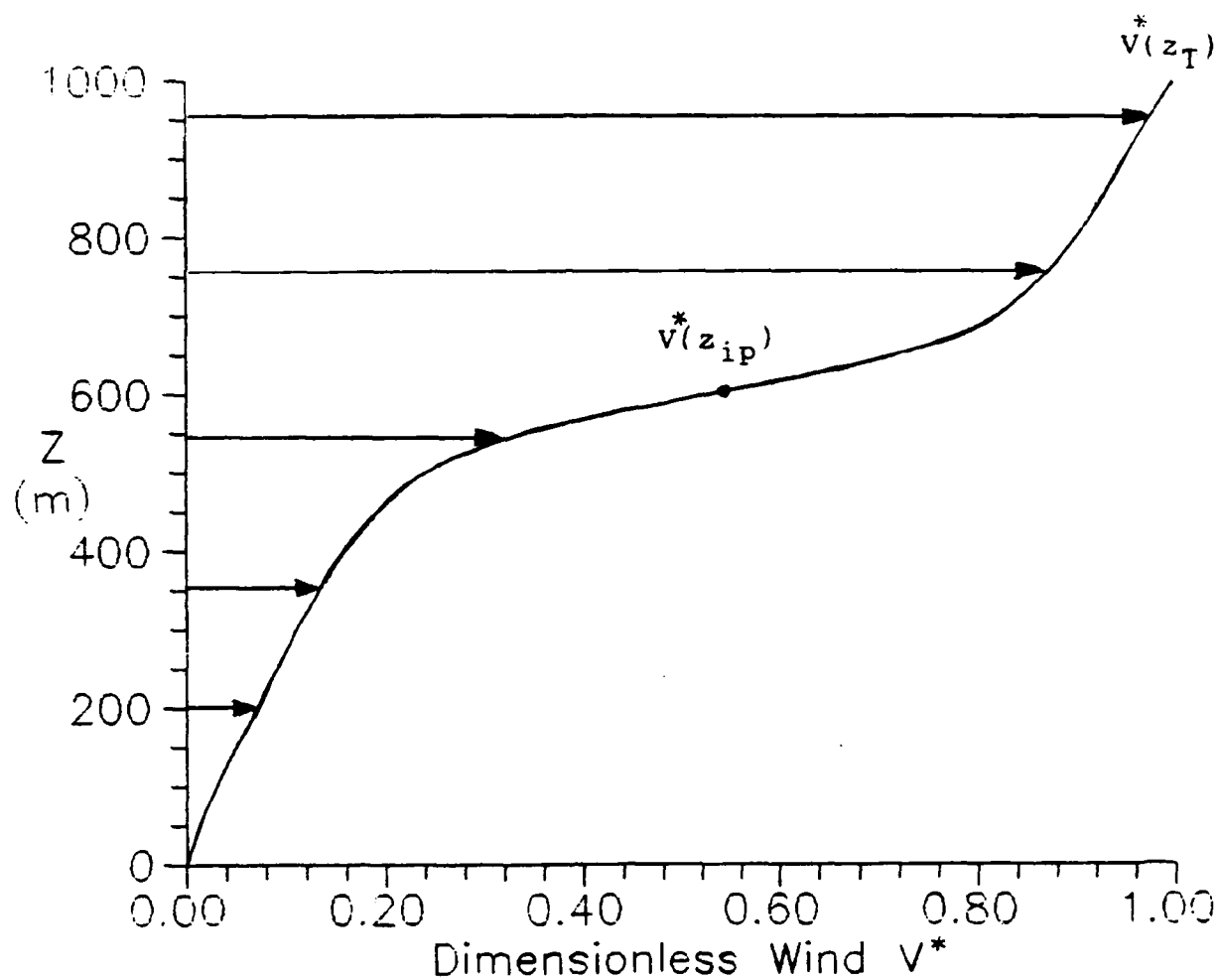


Fig. 4.2 Billows Wind Profile Given by (4.4)-(4.5). The dimensionless wind speed $v^*(z_{ip})$ at the height z_{ip} of the inflection point equals e equals 0.534. The dimensionless wind speed $v^*(z_T)$ at the domain top z_T is unity.

and wind profiles given by (4.6)-(4.7) and (4.4)-(4.5) respectively. By comparing Figs. 4.1 and 4.2, we see that there is a relatively large amount of wind shear located near the inflection point height z_{ip} as well as within the capping inversion itself. In the next subsection, we analyze the importance of this shear.

4.3.1 The Linear ($\varepsilon_i = 0$) Temperature Profile Case

The transition curves and the preferred values of a , β and $|\omega_0^*|$ resulting from the profiles (4.4)-(4.7) for the linear temperature profile case ($\varepsilon_i = 0$) are shown in Fig. 4.3 and an enlarged version of these transition curves is depicted in Fig. 4.4. We find that our model produces the three expected instability modes: the shear mode, the inflection point mode and the thermal q-mode. Our results, in general, agree qualitatively with the billows results obtained by Haack-Hirschberg (1988). We do not get the same quantitative results as obtained by Haack-Hirschberg (1988) because we wanted to check the effect of changing the height z_{ip} of the inflection point. We set z_{ip}^* at 0.6π and the corresponding value of e at 0.534, while Haack-Hirschberg set z_{ip}^* at the value of 0.50π and e at 0.500. Table 4.1 shows the effects of increasing the level of the inflection point. The point in (Ra, Re) -parameter space

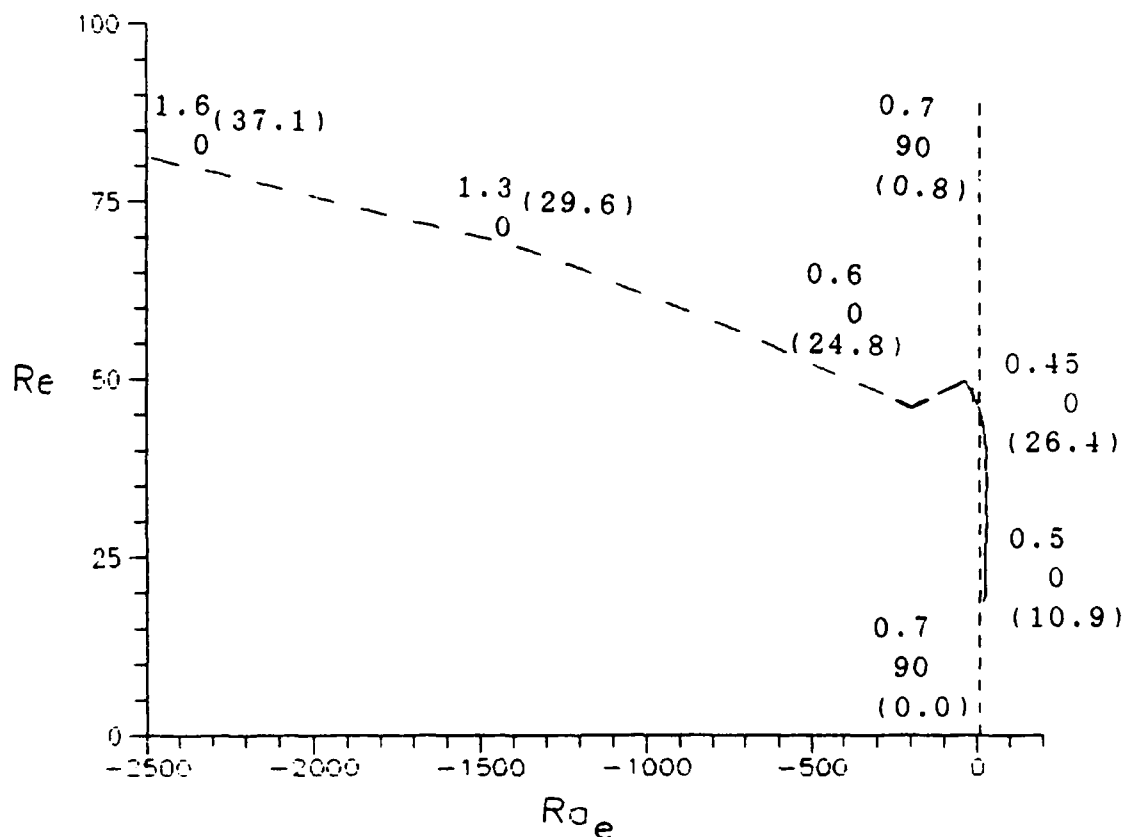


Fig. 4.3 Mode Diagram for the Billows Wind Profile (4.4)-(4.5) Illustrated in Fig. 4.2 for the $\epsilon_i = 0$ Case Given by the Temperature Profile (4.6) Illustrated in Fig. 4.1. The thermal q-mode is denoted by the small dashed line, the inflection point mode is denoted by the solid line and the shear mode is denoted by the large dashed line. Preferred values of a are given above preferred values of β (in degrees). Preferred values of $|\omega_0^*|$ are shown in parentheses. Here, $q = 1$, $n = 2$, $P = 1$, $z_{Tp} = 1000$ m.

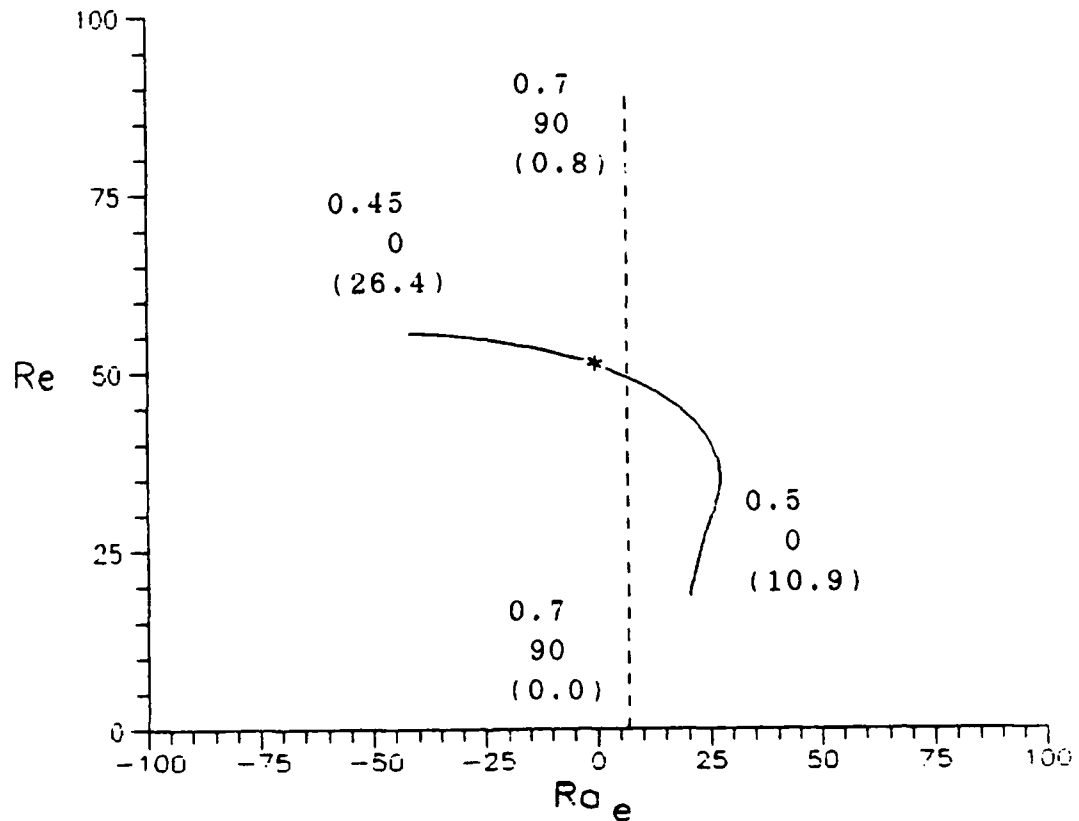


Fig. 4.4 Enlarged Version of Fig. 4.3 Isolating the Thermal (dashed line) and Inflection Point (solid line) Modes. The asterisk denotes the pure inflection point mode given by neutral stratification ($Ra = 0$); here, $Re_c = 52.46$. Preferred values of a are given above preferred values of β (in degrees). Preferred values of $|\omega_0^*|$ are shown in parentheses.

Table 4.1

Effects of Varying the Level of the Inflection Point
on the Inflection Point Mode.
(at $Ra_{ec} = 0$)

Model	$(Re_c)_{min}$	β_p	a_p	$ \omega_o^* $
Haack-Hirschberg ($z_{ip}^* = 0.50\pi$)	24.93	0°	0.6	12.5
current ($z_{ip}^* = 0.60\pi$)	52.46	0°	0.45	26.1

that we choose to make this comparison is where the inflection point mode crosses the line $Ra_{ec} = 0$. The most notable difference is that both $(Re_c)_{min}$ and $|\omega_o^*|$ double in value when the inflection point is moved from 0.50π to 0.60π , in general agreement with the results of Brümmer and Latif (1985).

We show these effects of the inflection point height using the inflection point mode because it is the more physically relevant of the dynamic modes; similar changes in the preferred values are seen for the shear mode. The thermal mode, being only weakly dependent on the wind

shear, is not affected by changes in the inflection point height. Although we have shown analytically that the thermal mode is independent of the background wind when there is only one vertical wavenumber, we get a slight increase in the value of Ra_{ec} as the magnitude of Re_c increases. This dependence may be physical or it just may be due to numerical approximation. In either event, we do not consider this small dependence to be significant. For clarification, we restate that our model, or any model considering non-neutrally stratified conditions, gives stability results in terms of the effective Rayleigh number Ra_e and so the transition curves are most conveniently plotted in (Ra_e, Re) -parameter space (as is done in this chapter). However, when comparing model results with observations or with other model results (as we do in Chapter 5), we find it more physically meaningful to express the results in (Ra, Re) -parameter space because, as noted in Section 5.4.1, the sea surface/air temperature difference that forces the solutions determines Ra rather than Ra_e .

Another important reason for the difference between our results shown in Fig. 4.3 and those of Haack-Hirschberg (1988) is due to the grid resolution that we used to solve (3.13). We have discovered that using a high resolution grid allows us to separate the single Haack-Hirschberg (1988) billows inflection point mode into an inflection

point mode and a shear mode that she did not find.

Apparently, the grid resolution used by Haack-Hirschberg may not have been sufficient to separate the shear and inflection point modes. She incremented Re_c in units of 20, β every 10° and a in units of 0.10 while we used 2, 5° and 0.05 respectively.

As seen in Figs. 4.3 and 4.4, the inflection point mode (solid line) is distinguished from the shear mode (large dashed line) by having aspect ratios that are less than $1/2$ those of the shear mode as well as by it being the mode that occurs near neutral stability. In Fig. 4.4 we can follow the inflection point mode well into the thermal mode regime. Because the inflection point mode appears at larger values of Re_c than the thermal mode, its transition curve gives a local rather than a global minimum in parameter space and so is not as physically important. Eventually, however, as Re_c decreases in magnitude, the inflection point mode becomes more difficult to identify. Beginning at $Re_c \approx 21$, the inflection point mode becomes indistinguishable from the thermal mode. The inflection point mode is also difficult to identify when $Re_c > 56$ because it interacts with the shear mode. We call the regime in Fig. 4.3 where the inflection point mode interacts with the shear mode the dynamic mode regime since we cannot unambiguously identify which dynamic mode would be expected.

The mode characteristics that most clearly identify the inflection point from the shear and thermal modes in our model are relatively abrupt changes in the frequency, aspect ratio, orientation angle or critical effective Rayleigh number. Table 4.2 shows a portion of the sorted model output illustrating where the shear mode clearly ends and the inflection point mode begins. Here, the beginning of the inflection point mode is identified by the dramatic increase from -117.51 to -12.48 in consecutive values of Ra_{ec} , from 24.798 to 27.021 in values of $|\omega_o^*|$ and a drop in

Table 4.2

A Portion of the Model Output

Showing a Clear Mode Transition.

(at $Re_c = 56$, $\epsilon_i = 0$)

Ra_{ec}	$ \omega_o^* $	a_p	β_p
-129.26	24.416	0.65	-6.0
-124.18	24.529	0.65	4.0
-121.08	24.610	0.65	-1.0
-117.51	24.798	0.60	-1.0
-12.48	27.021	0.45	-1.0
-11.33	26.989	0.45	4.0
-9.87	26.945	0.45	-6.0
-7.10	27.466	0.40	-1.0

a_p from 0.60 to 0.45. The preferred orientation angle β_p does not change, however, because the wind profile is unidirectional.

However, as happens frequently during the transition between preferred modes, distinct mode characteristics are not so clearly defined. Recall from Fig. 3.3 that the first transition curve encountered is the physically most relevant one and that a path that the atmosphere follows may cross more than one curve in parameter space. We confirm Haack-Hirschberg's general suggestion that values of a_p , β_p and Ra_{ec} that identify the shear mode are virtually identical to those for the inflection point mode. Thus it is difficult to determine where one mode ends and the other begins. In addition, we find that a smooth transition occurs between the inflection point mode and the thermal mode as found by Haack-Hirschberg (1988) for the sinusoidal wind profile. This smooth transition is probably the reason why the shear and the inflection point modes are not distinguishable with the courser grid resolution and this effect may be related to why mixed modes are found typically in the atmosphere. In the (Ra_e, Re) -parameter range where it is difficult to determine the preferred mode, local minima in the critical values interact making it impossible to label a particular mode. Thus there is no physical relevance in separating them.

Because the thermal mode (small dashed line) depends

only weakly on the unidirectional wind, its transition curve as shown in Fig. 4.3 is virtually independent of Re_c . Table 4.3 compares the values of $(Ra_{ec})_{min}$, β_p , a_p and $|\omega_0^*|$ obtained from the single-wavenumber thermal q-mode with those obtained from the two-wavenumber representation of the full model for the linear ($\varepsilon_i = 0$) and nonlinear ($\varepsilon_i \neq 0$) cases discussed below. We find that the single-wavenumber $\varepsilon_i = 0$ analytic results match those of the single-wavenumber, special case of the full model, which is given in both cases by $\Lambda_2 = \Gamma_2 = \varepsilon_i = 0$. Thus the thermal q-mode may be numerically identified within the full model and we may now have confidence that deviations from these values in the $\varepsilon_i \neq 0$ case are due only to consideration of the more complicated nonlinear vertical temperature profile.

4.3.2 The Nonlinear ($\varepsilon_i \neq 0$) Temperature Profile Case

The case of the billows profile with a capping inversion included ($\varepsilon_i \neq 0$) is shown in Fig 4.5. We get the same three instability modes as in the non-inversion ($\varepsilon_i = 0$) case. Here, we see that the shear mode generally occurs at smaller values of Re_c than it does in the non-inversion case, and that unexpectedly, the preferred values of Ra_{ec} throughout a large part of the shear mode are only weakly dependent on the value of Re_c . This result

Table 4.3

The Thermal Special Cases Using a
Billows Wind Profile and an
Idealized Temperature Profile.

($q=1$, $n=2$, $P=1$, $z_{ip}^*=0.6\pi$, $z_i^*=0.8\pi$, $\gamma_{(inv)}=10$ °C/200 m)

Model	$(Ra_{ec})_{min}$	β_p	a_p	$ \omega_o^* $
q-mode	(6.75)*	--	0.71	0.0
analytical expressions ($\varepsilon_i = \Lambda_2 = \Gamma_2 = 0$) (3.30)-(3.34)				
q-mode	(6.75)*	--	0.71	0.0
full model representation ($\varepsilon_i = \Lambda_2 = \Gamma_2 = 0$)				
two-wavenumber full model representation ($\varepsilon_i = 0$, $Re_c = 1$)	6.75	90°	0.7	0.0
two-wavenumber full model representation ($\varepsilon_i \neq 0$, $Re_c = 1$)	36.37	90°	1.2	0.0

[* Ra_{ec} is independent of β
-- indeterminate: no preferred values of β

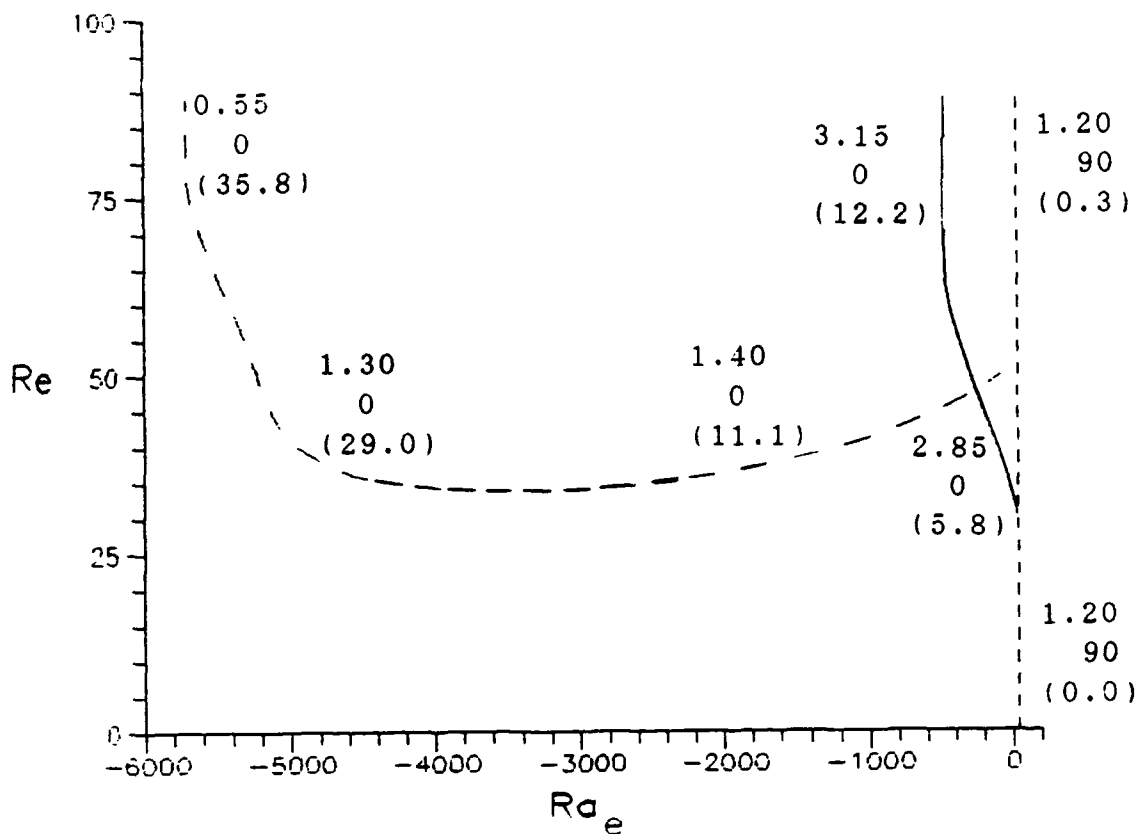


Fig. 4.5 Mode Diagram for a Billows Wind Profile (4.4)-(4.5) Illustrated in Fig 4.2 for the $\epsilon_i \neq 0$ Case Given by the Temperature Profile (4.6) Illustrated in Fig. 4.1. The thermal q-mode is denoted by the small dashed line, the inflection point mode is denoted by the solid line and the shear mode is denoted by the large dashed line. Preferred values of a are given above preferred values of β (in degrees). Preferred values of $|\omega_0^*|$ are shown in parentheses. Here, $q = 1$, $n = 2$, $P = 1$ and $z_{TP} = 1000$ m.

implies that the shear in the inversion is driving the rolls and produces the preferred mode since its critical Reynolds numbers are smallest in magnitude. Another contrast between the non-inversion and inversion cases is that the aspect ratios are larger for all modes when the inversion is included. This increase in aspect ratio is most apparent in the inflection point mode, where they increase from about 0.45 to 3.0. The reason for this increase in aspect ratio may be due to the increased thermal stratification when the inversion is included, as well as the increased values of z_{Tp} occurring when wind shear in the inversion forces deeper rolls to exist. A more stable atmosphere will induce a larger restoring force on the roll circulations and so will cause the circulations to decrease their radius. That is, the upward portion of the circulation will be turned down sooner than would occur in a less stable environment, and the downward portion of the circulation will be turned up sooner. Thus the roll wavelength decreases or the roll aspect ratio increases.

Using the methods for identifying mode transitions mentioned earlier, we are able to follow the shear mode for a short distance into the preferred inflection point region. In contrast to the non-inversion case, the inflection point mode remains clearly defined in Fig. 4.5. The range of (Ra_e, Re) values for which the inflection point mode occurs is much larger than for the $\epsilon_1 = 0$ case shown

in Fig. 4.3, implying that this instability mechanism is more dominant for the $\epsilon_i \neq 0$ case than for the $\epsilon_i = 0$ case. However, this phenomenon may be related to the large change in aspect ratio that simply provides a clear separation in dynamic mode characteristics in the $\epsilon_i \neq 0$ case. The inflection point mode shown in Fig 4.5 becomes independent of the value of Ra_e at $Ra_e \approx -500$ as Re_c increases past a value of $Re \approx 70$. This result is consistent with a result of Brown (1972) who found that one of the two dynamic instability mechanisms disappeared as the thermal forcing rate became less than a certain value or as the wind shear became greater than a certain value. Like the linear temperature profile case, the inflection point mode is characterized by neutral stability and we can follow this mode into the $Ra_{ec} > 0$ region, as shown by Asai (1972). However, we cannot identify the inflection point mode once it intersects the thermal q-mode at $(Ra_{ec})_{min} = 39.37$.

Figures 4.6 and 4.7 combine the transition curves from Figs. 4.3 and 4.5 as an aid in comparing the inversion and non-inversion cases. Here, we see that the thermal transition curves shift to more positive values of Ra_{ec} for the $\epsilon_i \neq 0$ case as compared with the $\epsilon_i = 0$ case. Another distinguishing feature of the $\epsilon_i \neq 0$ case is that the dynamic modes are excited at smaller values of Re_c than for the $\epsilon_i = 0$ case while the inflection point mode is shifted to more negative values. Thus while the thermal modes are

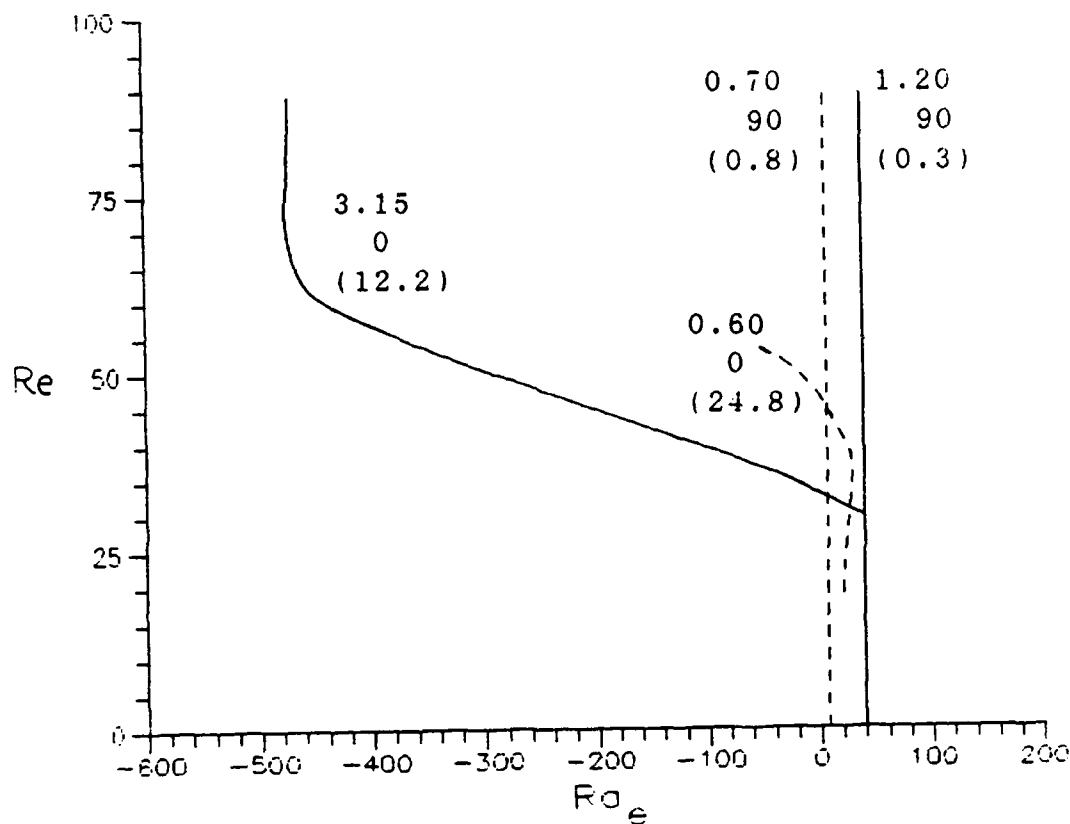


Fig. 4.6 Mode Diagram for a Billows Wind Profile (4.4)-(4.5) Illustrated in Fig. 4.2 Comparing the $\epsilon_i = 0$ and $\epsilon_i \neq 0$ Cases Given by the Temperature Profile (4.6) Illustrated in Fig. 4.1. The thermal and inflection point modes from Figs. 4.3 ($\epsilon_i = 0$, dashed lines) and 4.5 ($\epsilon_i \neq 0$, solid lines) are shown. As in these figures, a few selected preferred values of a , β and $|\omega_0^*|$ are given next to the curves.

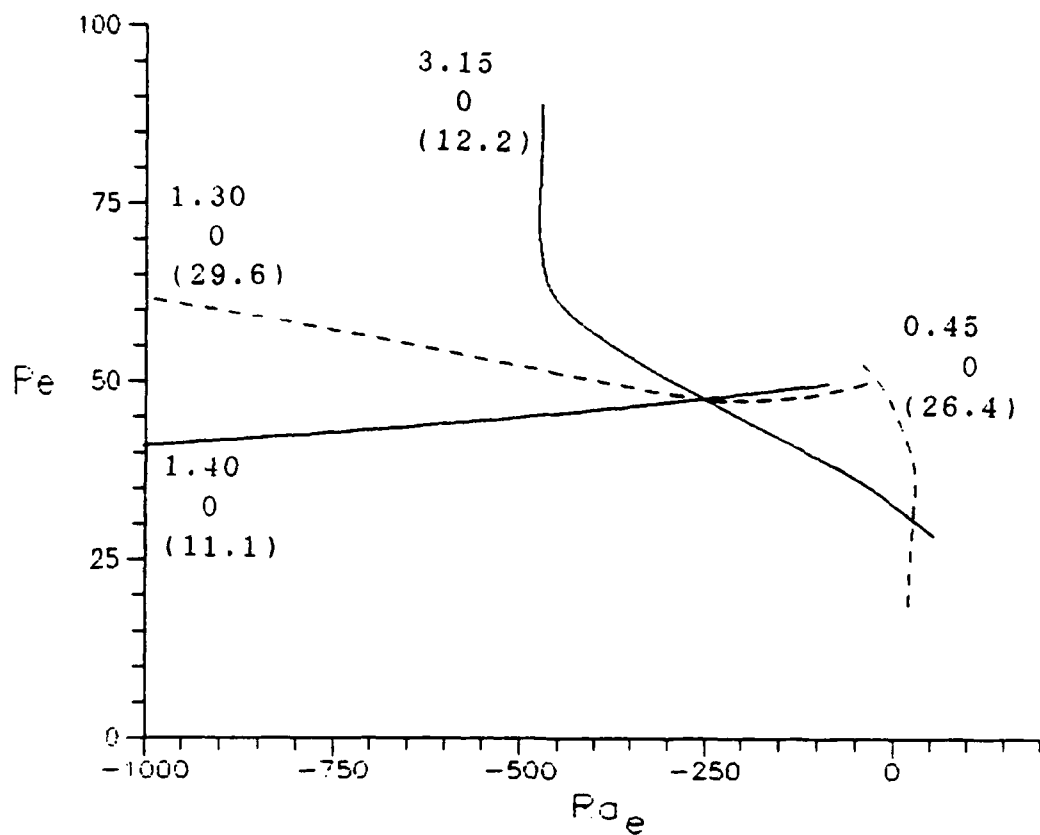


Fig. 4.7 Same as Fig. 4.6 Except for the Shear and Inflection Point Modes.

suppressed by the inversion, the inflection point mode is excited by interacting with it. The shear mode occurs at significantly smaller values of Re for the $\varepsilon_i \neq 0$ case than for the $\varepsilon_i = 0$ case and it also becomes independent of Ra_{ec} .

When the inversion height is lowered from 800 m ($z_i^* = 0.8\pi$) to 600 m ($z_i^* = 0.6\pi$) while maintaining the same inversion strength $\gamma_{(inv)}$, the preferred mode has the following characteristics:

- a_p increases by a factor of 2
- $(Re_c)_{min}$ for the dynamic modes decreases by a factor of 2
- $(Ra_{ec})_{min}$ of the thermal mode increases by approximately an order of magnitude
- $(Ra_{ec})_{min}$ of both dynamic modes increase by about 40 percent (i.e. these values become more positive)

With the inversion now 400 m deep, more surface heating would be needed to produce a thermal mode. Thus, as we discussed in Section 3.3, it is apparent that rolls associated with this mode would not extend into the inversion at existing levels of thermal forcing and the preferred value of z_T is z_i for the thermal mode. When we use observed data in the next chapter, we can vary the value of z_T as an aid in determining which instability mode is preferred. If the best model results come from using a value of z_T that is at or below the height of the inversion

base, then this indicates that the thermal mode may dominate. In contrast, because the magnitude of $(Re_c)_{min}$ has dropped in half, rolls that extend into the inversion are preferred for the dynamic mode. Indeed, because $Ra_{ec} \leq 0$, the appropriate view may be that the rolls originate in the inversion and extend down into the well-mixed layer. We conclude this because the observed value of Ra_e can be negative only if the sea surface/air temperature is negative so that there is no thermal forcing. Because of the large magnitude of the wind shear associated with the billows profile, the dominant instability mechanism is the inflection point instability for weak to moderate values of sea surface/air temperature contrasts so that $Ra_{ec} > -500$, and is the shear mode for large negative temperature contrasts. We hypothesize that if large wind shear exists in the inversion and $Ra_e \approx 0$, then the inflection point rolls extending into the inversion are preferred over the thermal rolls that remain below the inversion within the mixed layer.

From Figs. 4.4 and 4.5 we see that the thermal mode has a frequency $|\omega_0^*|$ on the order of 0.1, implying that these rolls are virtually stationary. In contrast, the inflection point mode shown in Figs. 4.3 and 4.4 has much larger frequencies implying significant roll translation. Physically, it is clear that the rolls produced by the thermal instability would not translate since these rolls

are aligned parallel to the background wind. In contrast, the rolls produced by the inflection point mode would be expected to translate since these rolls are oriented normal to the background wind.

An important test of our model is to determine whether it gives physically realistic roll propagation periods for each instability mode. These periods can be calculated by using the definition $T_p^* = 2\pi/\omega^*$ for the dimensionless period T_p^* of a wave and then substituting the general dimensionless form (2.21) for time t^* . The dimensional period T_p is

$$T_p = \frac{z_T L P}{\pi \nu \omega^*} , \quad (4.11)$$

and the dimensional phase velocity is

$$c = \frac{L}{T_p} , \quad (4.12)$$

where L is the domain width that is related to a and z_T by $L = 2 z_T/a$. The following typical values for the inflection point mode without an inversion ($\varepsilon_i = 0$) are used to calculate the propagation period: $Re_c = 54$, $|\omega_0^*| = 27.0$, $a = 0.45$, $z_T = 1$ km, $P = 1$ and $\nu = 20$ m²/s. These values, which also characterize the shear mode, give a typical period of 44 minutes and a phase velocity of 1.7

m/s. For the inversion case ($\varepsilon_i \neq 0$) at $Re_c = 54$, we use the following typical values: $|\omega_o^*| = 12.9$, $a = 3.10$, $z_T = 1$ km, and $\nu = 20$ m²/s. These values give a typical period of 13.3 minutes. Typical periods for the inflection point mode in this case are generally one-third to one-half the periods of the shear mode. In calculating the roll periods for the inversion ($\varepsilon_i \neq 0$) and non-inversion ($\varepsilon_i = 0$) cases, we used the value of ν as reported by Brümmer (1985), which as noted by Laufersweiler and Shirer (1989), would be appropriate for a well-mixed layer. Owing to the model formulation, we must assume that a boundary layer with an inversion has the same values for ν and κ as an atmosphere without an inversion, even though it makes more sense to assume that the values of ν and κ decrease with height in the inversion.

We see that including the inversion in our model has reduced the propagation period for the inflection point mode to one-third of its non-inversion value. Thus roll propagation is due to the dynamic forcing of the mean wind and due to an oscillation caused by the additional restoring force introduced by the inversion. In contrast to the inflection point mode, the phase speed of the thermal mode is essentially zero in both cases with a period on the order of three days.

Haack-Hirschberg (1988) suggests that the shear mode she found may be a gravity wave mode, which has a

characteristic period of oscillation in the range of 6 to 35 minutes (Dutton, 1976). Her reasoning is that the propagation period of the shear mode is on the same order as that of a gravity wave oscillation. We find that both the shear mode and the inflection point mode have periods on the order of a gravity wave oscillation for the $\epsilon_1 \neq 0$ case and so this criteria alone may not be sufficient to explain the shear mode. This result implies that gravity waves influence roll propagation rates when the rolls are driven by shear within the inversion. The extent to which gravity waves excited by the capping inversion influence roll propagation rates is not yet clear. As recognized by Haack-Hirschberg (1988), however, both the shear mode and the gravity wave mode, but not the inflection point mode, occur in strongly stratified conditions. The only part of the vertical domain that is strongly stratified (see Fig. 4.1) is the portion within the inversion. If a gravity wave occurs, then it will probably be restricted to this region. The shear mode then may only be physically relevant in the capping inversion and may not be appropriately viewed as extending down into the boundary layer; to be sure however, we must find the nonlinear solutions to this problem, which is task beyond the scope of this thesis.

Using the squared Brunt-Väisälä frequency given by

$$\omega_g^2 = (g/\theta_0)(\partial\theta/\partial z)_0, \quad (4.13)$$

and the temperature profile given by Fig. 4.1, we may calculate the period of a gravity wave as a further check of its relevance to the shear mode. A gravity wave occupying the entire vertical domain in Fig 4.1 with an inversion strength of 5 °C/100 m would respond to a linear temperature gradient of approximately 3 °C/1000 m. In this case, the period given by (4.13) and the definition of a wave period $T_p = 2\pi/\omega$ is 10.3 minutes. A gravity wave with this period of oscillation would be indistinguishable from the periods of the shear and the inflection point modes. As noted above, it is possible that any shear modes produced by the model may be most appropriately interpreted as gravity waves that occur only within the inversion. In this case a typical gravity wave having vertical scales of $z_T - z_i \approx 100$ m would have a period of oscillation of 2.6 minutes, which is clearly distinguishable from that for the boundary layer filling dynamic modes.

In the next chapter, we use observed wind and temperature profiles to compare the full model results with observations of horizontal rolls taken during the KonTur 1981 field experiment. Good agreement between any one of the three instability modes and the observations indicates that the full model contains appropriate background representations for modeling observed roll circulations.

Chapter 5
MODEL RESULTS USING OBSERVED
WIND AND TEMPERATURE PROFILES

In Chapter 4 we used idealized wind and temperature profiles to verify that the Hopf bifurcation equation (3.13) that governs the stability of the linear spectral model (3.1)-(3.4) produced three of the known instability modes: the shear mode, the inflection point mode and the thermal q -mode. In this chapter, the full model is tested further by using observed wind and temperature data. The roll modes that are excited by the observed wind and temperature profiles are identified numerically through the use of the features and characteristics discovered in Chapter 4.

5.1 The KonTur 1981 Observations

The observations used below in (3.13) were taken over the North Sea off the coast of West Germany as part of the West German field experiment KonTur that was conducted during September and October 1981. The purpose of KonTur was to supply a data base for detailed modeling of mesoscale and smaller scale convective processes. On three days, 18 September, 20 September and 26 September, horizontal roll circulations were observed and the data

were analyzed (Brümmer, 1985). On 20 September, the rolls occurred in statically unstable air ahead of an advancing cold front and they did not extend into the capping inversion. On 18 and 26 September, the rolls occurred in statically stable air ahead of an approaching warm front. In the first case, approximately one third of the roll circulation extended into the capping warm frontal inversion overlying the well-mixed portion of the boundary layer, while in the second case the rolls were restricted to a weakly stratified boundary layer. On 18 September, cloud streets were visible during the entire time that the measurements were taken. In contrast, on 26 September cloud streets were visible for only a short while after data collection began. Afterwards, the roll circulations were made visible by quasi-linear patterns in the boundary layer haze. Of the three days that measurements were taken, 20 September was the only day that was characterized by a mixed layer that filled the entire depth of the roll circulations. The vertical wind shear on this day was very weak; hence the height z_T of the roll circulations essentially must be limited to the height z_i of the inversion base, as observed. Since we are interested in the effect that wind shear in an inversion has on roll circulations, we limit our study to the days of 18 and 26 September.

Of the measurements that were taken during KonTur, the

relevant ones for our use are the vertical soundings of potential temperature, mixing ratio and horizontal wind components that were taken by two instrument-equipped aircraft. The coordinate system that was used to express the measured winds assigns the x-direction to the along-roll wind component and the y-direction to the cross-roll wind component. Figures 5.1 and 5.2 display these observed vertical profiles for 18 and 26 September, respectively. On 18 September the potential temperature profile reveals a well defined mixed-layer capped by a strong inversion; on 26 September, a strong inversion caps a weaker one that extended through most of the boundary layer. The tops z_T of the observed roll circulations, which are indicated by the solid horizontal lines, extended well above the inversion base z_i on the 18th; in contrast, on the 26th the rolls extended very little above the base of the inversion. As we note below, the values of z_T were reported to be $530 \text{ m} \pm 50 \text{ m}$ on the 18th and $500 \text{ m} \pm 50 \text{ m}$ on the 26th. Brümmer (1985) estimates that the heights z_{ip} of the inflection points in the wind profiles were at approximately $450 \text{ m} \pm 50 \text{ m}$ on 18 September and at $440 \text{ m} \pm 50 \text{ m}$ on 26 September. An energetics analysis by Brümmer (1985) revealed that the roll circulations on both the 18th and 26th were driven by the inflection point instability since the buoyancy terms were predominantly negative. To verify Brümmer's energetics work, our model should produce roll

18 SEPTEMBER 1981 0855 - 0909 UTC

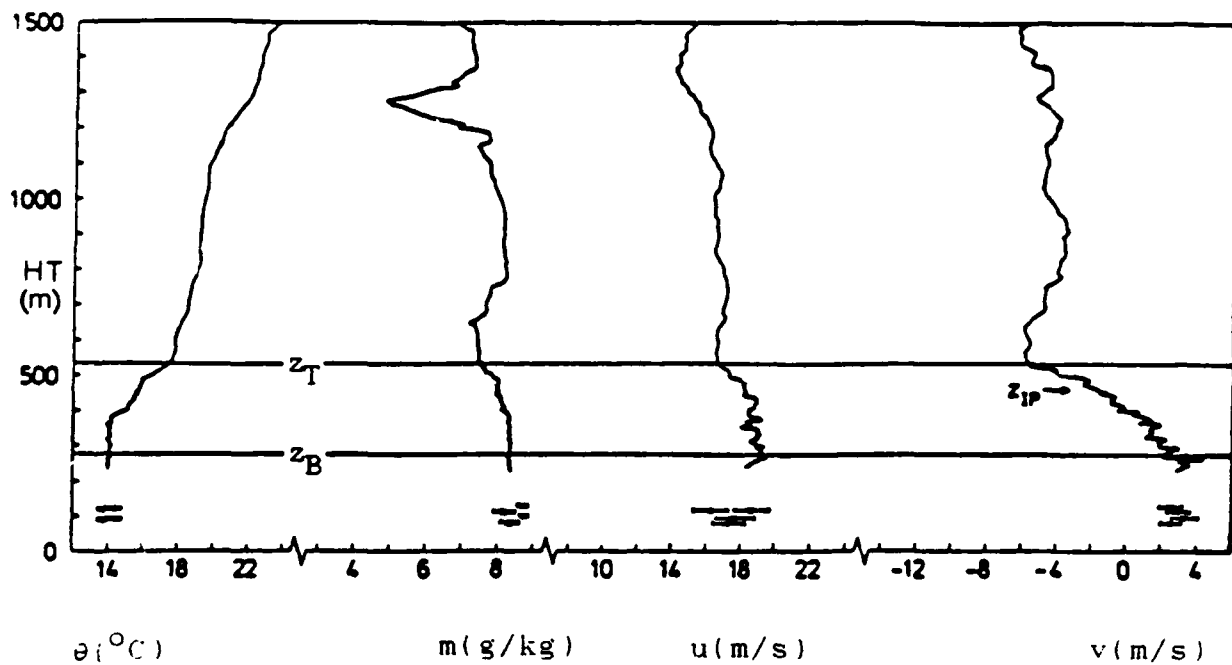


Fig. 5.1 Vertical Profiles of Potential Temperature θ , Mixing Ratio m , Along-roll Wind u and Cross-roll Wind v Measured on 18 September 1981 During KonTur. The solid horizontal lines give estimates of the cloud base z_B and circulation top z_T . The inflection point in the cross-roll wind is denoted by z_{ip} (after Brümmer, 1985; Haack-Hirschberg, 1988).

26 SEPTEMBER 1981 1120 - 1127 UTC

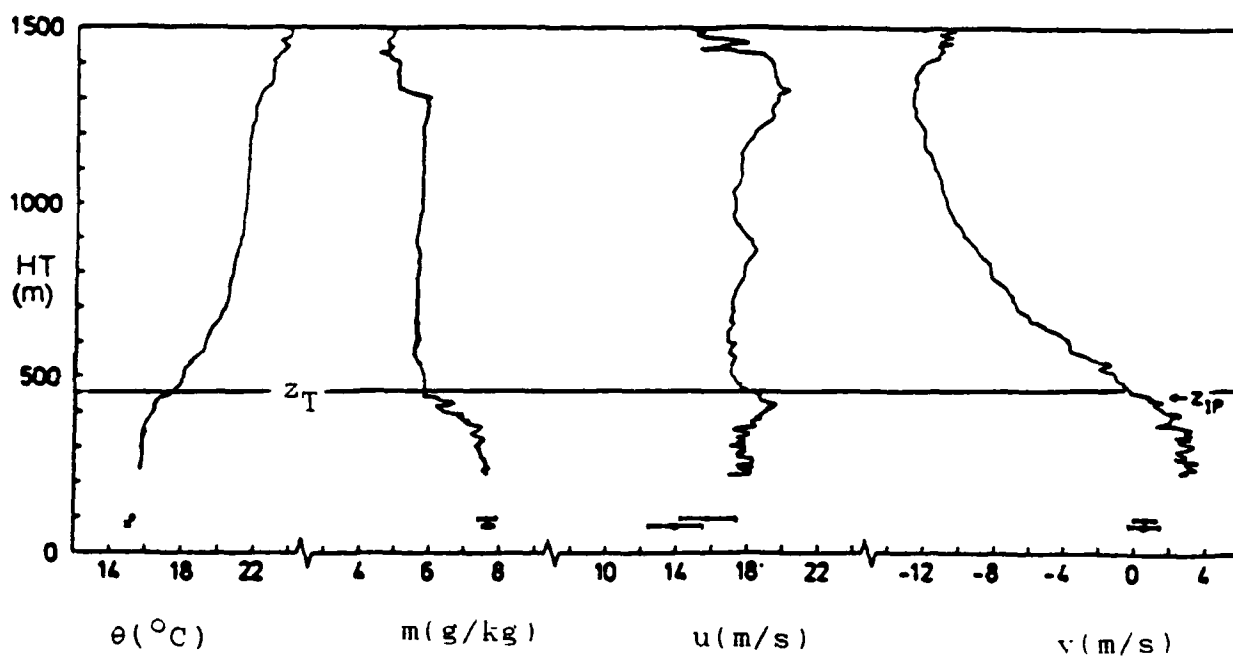


Fig. 5.2 Vertical Profiles of Potential Temperature θ , Mixing Ratio m , Along-roll Wind u and Cross-roll Wind v Measured on 26 September 1981 During KonTur. The solid horizontal line gives an estimate of the circulation top z_T . The inflection point in the cross-roll wind is denoted by z_{ip} (after Brummer, 1985; Haack-Hirschberg, 1988).

characteristics that are similar to this dynamic mode.

The measured horizontal wind components u and v have an accuracy of ± 1 m/s (Shirer and Brümmer, 1986). Using the profiles that were measured by the aircraft and the estimated magnitude of the eddy viscosity ν as given by Brümmer (1985), and assuming $\nu = \kappa$, we calculated the observed ranges of the dynamic and thermodynamic forcing rates Re and Ra using the respective definitions given by (2.31) and (2.32). Owing to the difficulty in estimating values for κ (Brümmer, 1985), it is normally set equal to the value of ν . The uncertainties in the estimates of ν vary from one-half to twice the values reported by Brümmer (1985) and so the ranges in the observed values of Re and Ra can be large. For example, on both days, the values of ν range from about 10 to 30 m^2/s . When plotted in (Ra, Re) -parameter space, these ranges appear as elongated, tilted areas that are shown in Figs. 5.7 and 5.8 (Section 5.4) for each of the two roll cases.

The observed average roll heights z_T on both days had a 50 meter margin of error, so we varied z_T to determine the height that provided the best results; in this way we are able to find z_{T_v} for the mode describing rolls extending into the inversion. On 18 September, we varied z_T from 575 m to 475 m and got results that did not represent the observed roll geometry until we used a roll top of 525 m; the observed roll height was reported at 530

m (Fig. 5.1). On 26 September, there were no roll clouds visible and so the average roll top height was assumed to be the highest level of significant turbulence (Shirer and Brümmer, 1986). Brümmer (1985) reported z_T on 26 September to be 500 m; however, this height apparently applies to the 0920 UTC soundings that were incomplete. Instead, we use the soundings that were taken at 1120 UTC for which a domain height of 450 m seems more appropriate (Fig. 5.2). We verified that this height was more representative of the observation because we varied z_T from 550 m to 400 m and got the best results with $z_T = 450$ m.

The sea surface temperature on 18 September was reported by Brümmer (1985) to be 15 °C and on 26 September it was 16 °C. On both days, Brümmer (1985) estimated that the sea surface/air temperature difference at the surface was between +0.5 °C and +1.0 °C.

Roll wavelength L and orientation angle β are two other important features that indicate whether the model successfully captures an instability mechanism. Ranges for these values were determined visually by the mission scientist on each flight. The estimates of the wavelengths were compared with measurements of the radiative flux and mixing ratio that were taken during the cross-roll flight legs. The reported ranges in L were obtained from these comparisons. On both days, these comparisons revealed that L varied by about a factor of three: on the 18th L ranged

from 1200 m to 3300 m, and on the 26th L ranged from 800 m to 2700 m (Shirer and Brümmer, 1986). We use this range in values of L to make our model comparisons.

The roll wavelengths are combined with the domain height to calculate the range of observed aspect ratios. The observed roll orientation angles were expressed in terms of the direction of the mean boundary layer wind. This wind direction was estimated to be along the roll axis, producing an observed orientation angle β of 90° . The uncertainty in the orientation angles was estimated by Shirer and Brümmer (1986) to be $\pm 10^\circ$. When we compare the orientation angle produced by our model with that of the observations, we use the directions corresponding to those for the mean wind shear and the mean wind direction. For both days, the observed roll characteristics are summarized in Tables 5.2 and 5.3 in Section 5.4.

Using the observed wind and temperature profiles for each roll case, we solve the Hopf bifurcation equation (3.13). The resulting transition curves are then graphed in (Ra, Re) -parameter space producing mode diagrams similar to those given in Chapter 4. In this chapter, we find it more convenient to use Ra rather than Ra_e ; further explanation is provided in Section 5.4.1. We consider the model results to be in agreement with observations if:

- 1) the (Ra_c, Re_c) transition curve for a mode passes through or just to the left of the observed (Ra, Re) -parameter region, indicating that the atmospheric values of Ra and Re were greater than the minimum values of Ra_c and Re_c that would be needed to excite that mode, and if
- 2) the preferred roll characteristics a_p and β_p for that mode fall within the observed ranges of a and β , and if
- 3) the preferred circulation depth z_{Tp} falls within the reported range of z_T , and if
- 4) the roll periods T_p given by the model are physically realistic.

In the remainder of this chapter, we use the KonTur wind and temperature profiles to compare our model results with the observations in order to determine which of the instability modes most likely generated the roll circulations.

5.2 Results from Two Previous Models

In this section, we summarize the results obtained from two previous spectral models of roll circulations: the two-wavenumber pure inflection point instability model of Stensrud and Shirer (1988), and the two-wavenumber dynamic/thermal model of Haack-Hirschberg (1988).

Stensrud and Shirer (1988) derived a spectral model from a two-harmonic expansion; a similar two-harmonic expansion was adopted for the present study. Since the Stensrud and Shirer model lacked thermodynamics, it was restricted to cases of neutral static stability. They considered only the data measured on the 26th and they performed an interpolation of two wind profiles that were taken two hours apart; in contrast, we use the later, more complete observed profile. Because the wind data were interpreted differently from ours, we can make only qualitative comparisons with their results.

The essential findings of Stensrud (1985) and Stensrud and Shirer (1988) are that the observed characteristics on 26 September may be described by the pure inflection point instability mode. The values of the roll geometry produced by their model were in general agreement with the observations. Stensrud's (1985) results on the 18th, however, are not as revealing as those on the 26th. He concludes that the inflection point mode played little or no role in the formation of the rolls on this day while recognizing that this conclusion contradicts the results of Brümmer (1985). As we show below, the reason for Stensrud's inconclusive results must be due to the neglect of the basic state temperature profile.

The model of Haack-Hirschberg (1988) extended that of Stensrud and Shirer (1988) to include a simple case of

thermal stratification. Our model is similar to Haack-Hirschberg's except that we have added the ϵ_i terms into the definition of the temperature profile in order to account for a more general vertical temperature structure. Although the observed winds are represented more accurately in our model (we used values at 25 m intervals versus Haack-Hirschberg's 50 m intervals), we feel that the differences in observed data used by both models are not significant.

Haack-Hirschberg concludes that the shear mode gives the best representation of the observed forcing rates and roll characteristics on both 18 and 26 September. To support her conclusion, she used the observed ranges for the atmospheric values of Ra_{ec} given by Shirer and Brümmer (1986). Shirer and Brümmer calculated these observed ranges by estimating the linear contribution to the vertical temperature profile and by incorporating the effects of latent heating. Because an inversion occurred on each day, this linear contribution to the vertical temperature profile gave a positive slope and therefore, the ranges of their atmospheric Rayleigh numbers were negative. In contrast, we calculate the ranges of the observed Rayleigh numbers by using the magnitude of the surface forcing that is given by the water/air temperature difference $\Delta_z T(\text{water-air})$ that was positive. This method gives atmospheric ranges of the Rayleigh number that we

feel are physically more realistic. If this is the case, then we show below that the shear mode is too far to the left of the observed atmospheric ranges in (Ra, Re) -parameter space to adequately represent the forcing mechanisms that occurred on 18 and 26 September. (Of course the shear mode is still a possible instability mechanism since it is to the left of the atmospheric ranges.) Instead, we conclude in agreement with Stensrud and Shirer (1988) and Brümmer (1985) that the inflection point instability mechanism played a more important role on these two days.

5.3 Fourier Representation of the Profiles

Before we analyze the stability results from the KonTur cases, we first must ensure that the Fourier coefficients of the background wind profile (Λ_j and Γ_j) and the temperature profile (ε_j) adequately represent the observed data. In this section we test the accuracy of the Fourier coefficients in the model by using them to construct approximations of the vertical profiles. Mathematically, it is easy to obtain the optimal Fourier coefficients. However, to ensure that these coefficients represent physically realistic conditions, the approximate profiles obtained by using the mathematically calculated coefficients must give good visual fits to the observed

data. Once we obtain this good fit to the data, we may have confidence that the effects of the wind and temperature profiles on the stability analysis are properly represented.

To approximate the wind and temperature profiles, we use an IMSL least squares program. This program gives the optimum amplitudes of the coefficients for user-defined functions that best fit the observed data. We interpolate the data given in Figs. 5.1 and 5.2 at 25 m intervals. We choose the following Fourier expansion to represent each wind profile on 18 and 26 September:

$$\begin{aligned} \underline{v}^*(z^*) = & \underline{v}_0^* + \underline{v}_1^* \sin(z^*) + \underline{v}_2^* \cos(z^*) + \underline{v}_3^* \sin(2z^*) \\ & + \underline{v}_4^* \cos(2z^*) + \underline{v}_5^* \sin(3z^*) \quad , \end{aligned} \quad (5.1)$$

in which $\underline{v}^*(z^*)$ is the dimensionless height-dependent background wind that has components in the x^* - and y^* -directions. We are limited to six amplitude coefficients in (5.1) since we have six Fourier coefficients Λ_j and Γ_j , with $j=1,2,3$. We choose the particular trigonometric functions given in (5.1) because they are the lowest order functions of the more complete Fourier series and because their coefficients have the largest magnitudes.

We approximate the observed temperature profiles using the same method as that for the wind profiles. Here, since

we have three Fourier coefficients ϵ_i of the temperature with $i=1,2,3$, we can only use three trigonometric functions. The Fourier expansion that we use to represent each potential temperature profile for the 18 and 26 September cases is given by

$$\theta(z^*) = \Delta_z \theta(\text{air}) z^* + \theta_2 \cos(z^*) + \theta_3 \sin(2z^*) + \theta_4 \cos(2z^*) \quad . \quad (5.2)$$

As we discuss below, inclusion of a constant term θ_0 in (5.2) gives a poorer qualitative fit to the data, while the linear term $\Delta_z \theta(\text{air})$ is required to estimate with (2.34) the value Ra_i in order to calculate Ra_c from Ra_{ec} . Finally, the coefficients θ_2 , θ_3 , and θ_4 have the same meaning as T_1^* , T_2^* and T_3^* in (2.8) because both represent deviations from a linear background profile.

Figures 5.3 and 5.4 display the observed wind profiles (dashed lines) and the approximated wind profiles (solid lines) for 18 and 26 September, respectively. Here, the u-wind is the cross-roll component and the v-wind is the along-roll component. We see that the approximate wind profiles provide accurate representations of the observed wind profiles. The potential temperature profiles are displayed in Figs. 5.5 and 5.6. These approximate profiles (solid lines), although not as accurate as the approximate wind profiles, provide visually adequate representations,

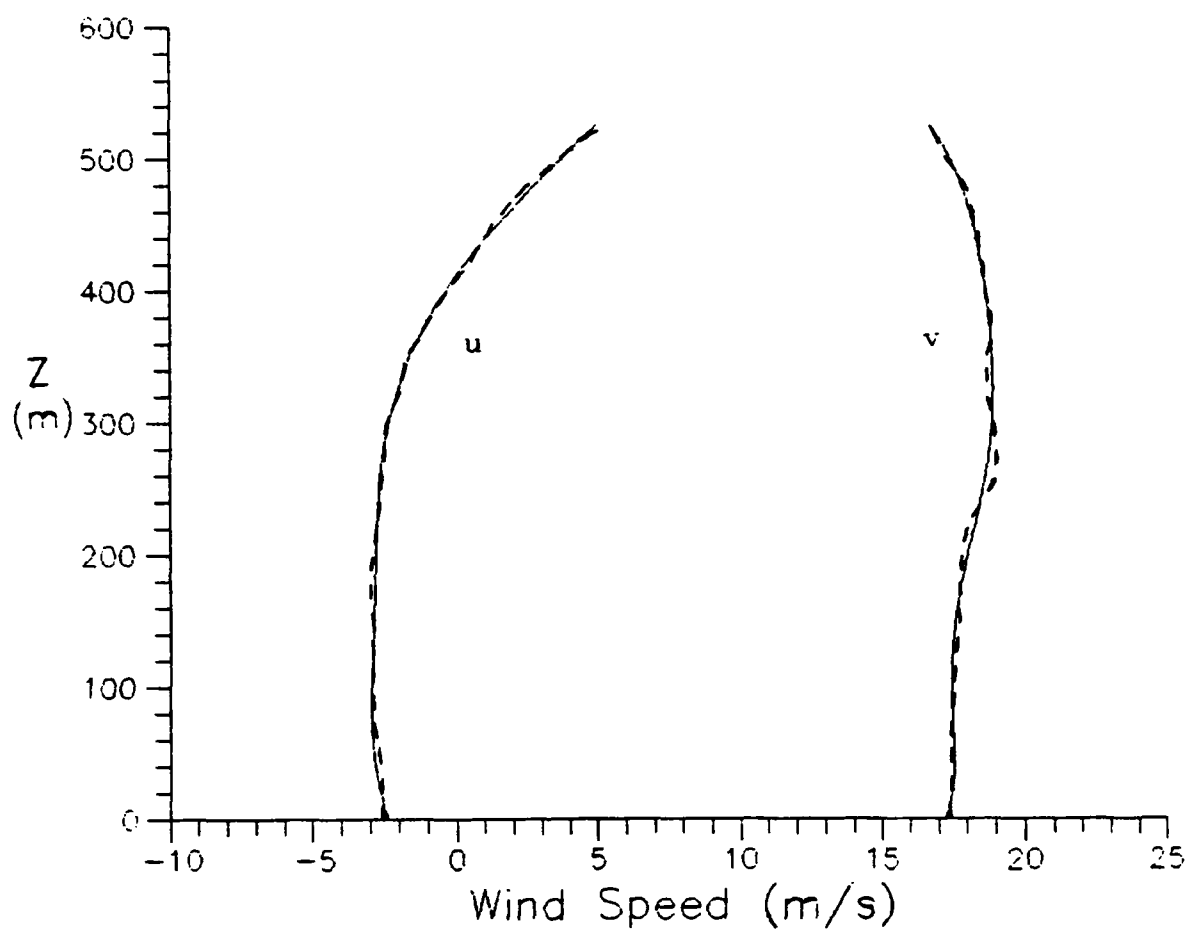


Fig. 5.3 A Comparison of the Observed Profiles (Fig. 5.1; dashed lines) and the Approximate Profiles (solid lines) of the Along-roll Wind v and the Cross-roll Wind u on 18 September 1981. The appropriate Fourier coefficients are given in Table 5.1.

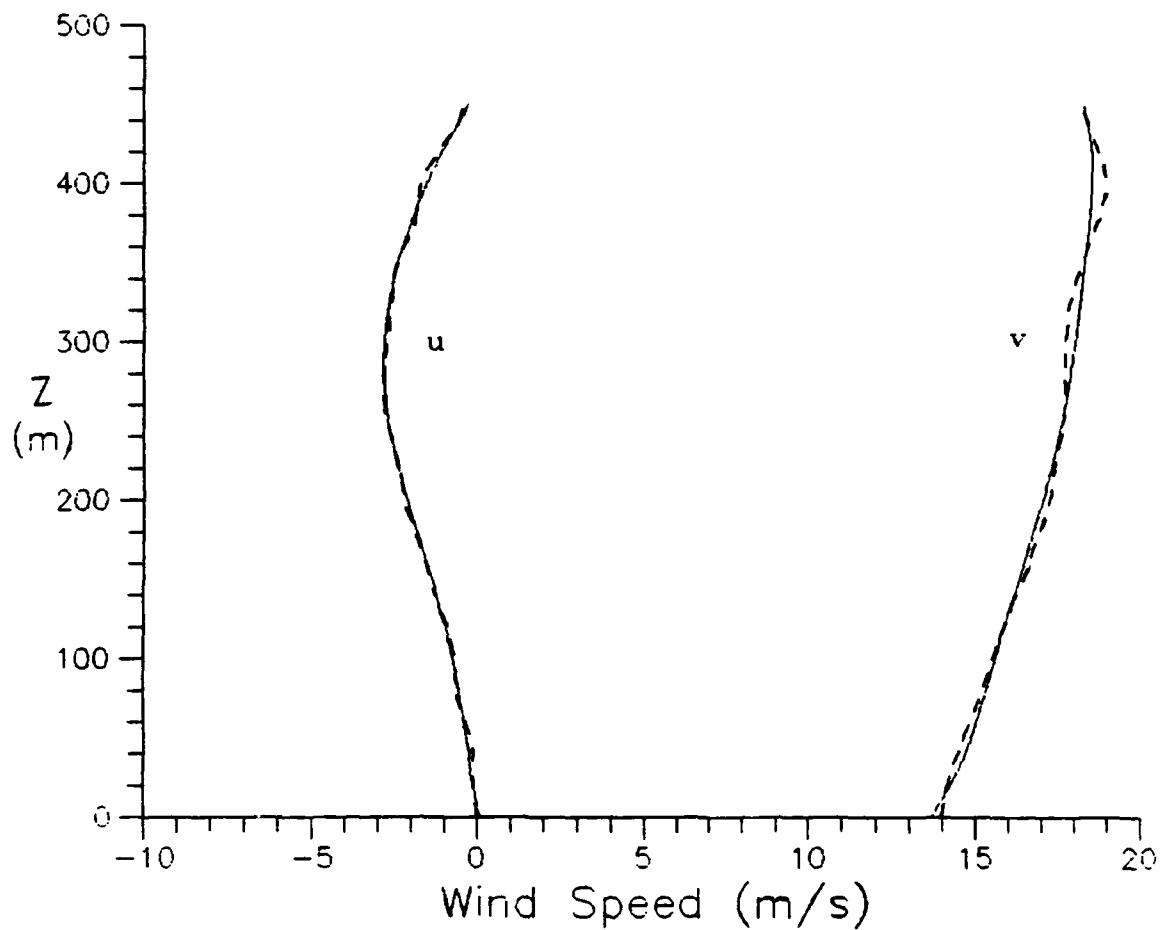


Fig. 5.4 A Comparison of the Observed Profiles (Fig. 5.2: dashed lines) and the Approximate Profiles (solid lines) of the Along-roll Wind v and the Cross-roll Wind u on 26 September 1981. The appropriate Fourier coefficients are given in Table 5.1.

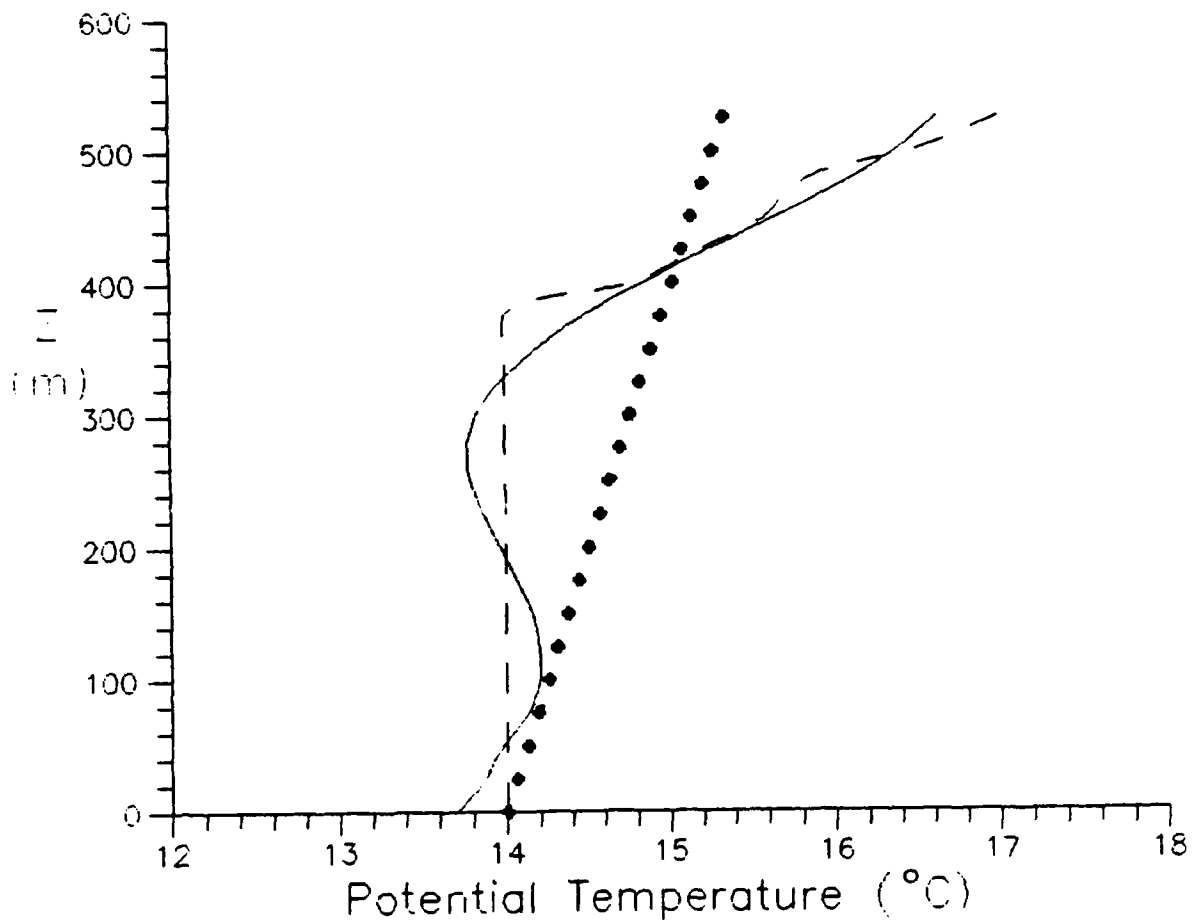


Fig. 5.5 A Comparison of the Observed Potential Temperature Profile (Fig. 5.1; dashed line), the Approximate Profile of Potential Temperature (solid line), and Its Linear Component (dotted line) for 18 September 1981. The appropriate Fourier coefficients are given in Table 5.1.

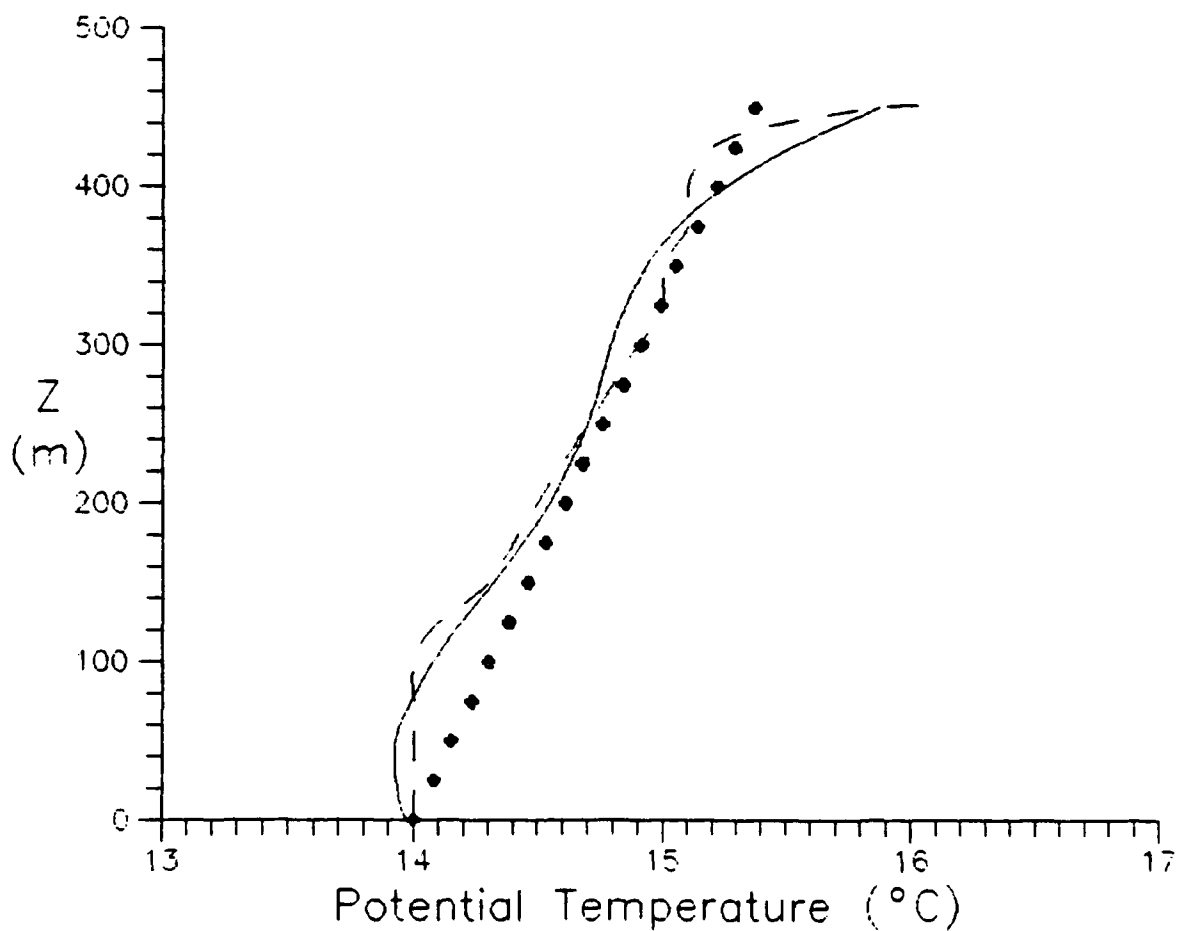


Fig. 5.6 A Comparison of the Observed Potential Temperature Profile (Fig. 5.2; dashed line), the Approximate Profile of Potential Temperature (solid line), and Its Linear Component (dotted line) for 26 September 1981. The appropriate Fourier coefficients are given in Table 5.1.

in addition to being the mathematically optimal representations, of the observed potential temperature profiles (dashed line). As with the profile depicted in Fig. 2.2, the deviations from the observed values are on a small enough scale that they do not significantly affect the model results. We see that on 26 September the linear component (dotted line) of the temperature profile gives a good approximation to the observed profile. On 18 September, however, only the full expansion provides an adequate representation to the observed data.

In addition to the trigonometric functions that we use to approximate the wind and temperature profiles that are shown in Figs. 5.3 through 5.6, we must also consider constant and linear functions in order to represent the mean value and the trend in the data. For the wind profile, we find that a Fourier expansion including only the constant term in the expansion gives the best fit to the observed data. In contrast, for the temperature profile, we find that the Fourier expansion containing the linear function gives the best fit to this data. Since the number of Fourier functions that we may use to represent the temperature profile is severely limited, we cannot include enough terms from a sine or cosine series to adequately approximate a linear function. Thus the linear term is required to produce an adequate fit. Physically, the linear component of the expansion represents the

buoyancy term $B(z)$ that is given in (2.13) by the difference between the background temperature lapse rate $-\partial T_0/\partial z$ and the adiabatic lapse rate γ_d . The wind profiles, however, include the first three terms of a sine series in z^* and so it can adequately represent the linear components of the observed data.

We approximated the temperature profile by including the constant term and found no significant improvement in the results. In fact, the approximated potential temperature profile including the constant term for 26 September did not provide as good a qualitative fit as did the profile without it. Thus the Fourier coefficients of the potential temperature that we predominantly use in the model do not contain the contributions from a constant coefficient. In the next section, we will illustrate the effects of including the constant term in the Fourier potential temperature expansion by showing how much the preferred transition curves vary in (Ra, Re) -parameter space.

It is understandable that the least squares fit to the potential temperature curve is not as good as the least squares fit to the wind because we have only three trigonometric functions, that is three Fourier coefficients, available to fit the observed potential temperature curve. In addition, the vertical variation in potential temperature is much greater than that of the

wind, thus making it more difficult for a limited expansion to accurately fit the curve. We note that increasing the number of coefficients in the spectral expansion (2.38) for the temperature would improve the fit to the potential temperature profile. It follows that a better representation of the background potential temperature would produce model results that are in better agreement with the observations.

We have discovered that using the vertical wavenumbers $q = 1$ and $n = 2$ in the Fourier definitions gives a more accurate least squares fit to the wind profile on both 18 and 26 September than the vertical wavenumbers of $q = 1$ and $n = 3$ that Haack-Hirschberg (1988) used. This result is important since we also get the best least squares fit to the observed potential temperature profiles when we use vertical wavenumbers of $q = 1$ and $n = 2$. In addition, these vertical wavenumbers give good results for the preferred roll geometry on both 18 and 26 September, and so we feel that these wavenumbers are the most appropriate ones for this analysis.

As mentioned earlier, the expansions (5.1)-(5.2) that are used to approximate the wind and temperature profiles included either a linear term or a constant term in addition to the trigonometric terms that we use to define the Fourier coefficients for the stability analysis. Including the non-trigonometric terms in the least squares

analysis causes the magnitudes of the amplitudes multiplying the trigonometric terms to change according to the contributions from the non-trigonometric terms. The dimensionless Fourier coefficients of the temperature ε_i contain only trigonometric functions whose values are dependent on those for the non-trigonometric functions. For example, on 18 September, the least squares values for the Fourier coefficients ε_i without the effect of the constant term are given by $\varepsilon_1 \approx -87.5$, $\varepsilon_2 \approx 175.4$ and $\varepsilon_3 \approx -180.7$. With the constant term included in the least squares analysis, these coefficients become $\varepsilon_1 \approx -34.2$, $\varepsilon_2 \approx 165.5$ and $\varepsilon_3 \approx -125.1$. We see that the more complete expansion causes the magnitudes of the trigonometric terms to decrease considerably. While the effect of the temperature inversion as represented by the ε_i terms decreases in this case, the amplitude of the linear term increases so that the variation in background temperature $H(z)$ given by (2.7) remains essentially unchanged.

Now that the background wind and temperature profiles are represented properly by our model, we may conduct a stability analysis using the Fourier coefficients derived from the observed data; the values for these coefficients are shown in Table 5.1. With these Fourier coefficients in our model, we have confidence that the dynamic and thermodynamic forcing rates are represented properly.

Table 5.1

Values of the Fourier Coefficients Used in the Model.

18 Sep		26 Sep	
Wind	Temperature	Wind	Temperature
$u(1) = -0.12262$	$\varepsilon(1) = -34.23$	$u(1) = -0.11332$	$\varepsilon(1) = -50.31$
$u(2) = -0.04979$	$\varepsilon(2) = 165.49$	$u(2) = 0.03075$	$\varepsilon(2) = 35.04$
$u(3) = -0.09078$	$\varepsilon(3) = -125.12$	$u(3) = -0.09057$	$\varepsilon(3) = -56.93$
$u(4) = 0.17638$		$u(4) = 0.10660$	
$u(5) = -0.11655$		$u(5) = -0.10841$	
$u(6) = 0.19605$		$u(6) = 0.06242$	
$v(1) = 1.04944$		$v(1) = 0.94147$	
$v(2) = -0.02284$		$v(2) = -0.04747$	
$v(3) = 1.03445$		$v(3) = 0.92937$	
$v(4) = -0.06614$		$v(4) = -0.04882$	
$v(5) = 0.11485$		$v(5) = -0.00178$	
$v(6) = -0.02476$		$v(6) = -0.00167$	

The coefficients of the wind $u(1)$ - $u(6)$ and $v(1)$ - $v(6)$ form the Fourier coefficients that are β -dependent. (*cf.*

(2.68)-(2.73))

5.4 Stability Results

In order to obtain our model results for 18 and 26 September, we specify the values of the Prandtl number P , vertical wavenumbers, q and n , domain height z_T and coefficient of eddy viscosity ν and then compare them with the observed values as given by Table 5.2. As shown below, we get good model results using the observed values of z_T for both days. Unlike in the $\varepsilon_i = 0$ case, the results for the $\varepsilon_i \neq 0$ case depend much more on ν and P . On 26 September, we get good results using the observed value of ν with either the $\varepsilon_i = 0$ case or the $\varepsilon_i \neq 0$ case. On 18 September, however, we found it necessary to increase the magnitude of ν to the upper limit of the observed range in order to get good results for the $\varepsilon_i \neq 0$ case. Increasing the value of ν on the 18th improved the orientation angles by about 25 percent. The good model results on the 18th using a larger value of ν than observed suggests that either there is a problem with our model or that the observed value of ν is actually larger than reported. Since our model gave good results using the rest of the observed data, we feel that the value of ν is likely larger than reported.

In testing different values for the parameter ν in order to achieve the best model results, we found for both

Table 5.2

Comparisons of Values Specified in the Model
with the Observed Values.

Case	Prandtl no.	wave no.		z_T (m)		ν (m^2/s)	
	P	q	n	Obs	Model	Obs	Model
18 Sep	1	1	2	530	525	15	30
						(10-30)	
26 Sep	1	1	2	450	450	17	17
						(10-30)	

days that the values of Re_c , $|\omega_0^*|$, β_p and a_p are all sensitive to the value chosen for ν . As the value of ν is increased from its lower observed limit to its upper observed limit, the values of Re_c become more positive, the values of $|\omega_0^*|$ decrease, the values of a decrease and the values of β increase. Also, choosing larger values of ν force both the range of atmospheric values and the preferred modes toward larger values of Re_c . The primary effect of varying the Prandtl number P is to vary the preferred values of $|\omega_0^*|$. Doubling the value of P from 1 to 2 causes the value of $|\omega_0^*|$ to double. We note that estimating the value of κ was not even attempted by Brümmer (1985), implying that there is a great deal of uncertainty

in the values of the roll periods by (4.11).

We find for the KonTur cases, that an adequate grid resolution needed to differentiate the dominant roll modes involves increments of 20 in Re , 5° in β and 0.05 in a . Because our y -axis is aligned parallel to the rolls, we must rotate clockwise the roll coordinate system used in KonTur (Figs. 5.1 and 5.2). Thus the winds in our model are related to the KonTur winds by the following rotation: $v(\text{our model}) = u(\text{KonTur})$ and $u(\text{our model}) = -v(\text{KonTur})$. Our orientation angle β measures the angle between the roll axis and the standard x_s -direction. Thus an orientation angle of $\pm 90^\circ$ corresponds to a roll axis that is parallel to the mean wind direction.

5.4.1 The Linear ($\varepsilon_i = 0$) Temperature Profile Case

The two mode diagrams for the linear ($\varepsilon_i = 0$) cases are given in Figs. 5.7 and 5.8. In each figure, the observed range in Ra and Re is enclosed by the tilted box and the observed values of a and β are noted above the mode diagrams. A few preferred values of a , β and $|\omega_0^*|$ are listed along each transition curve. The stippled regions next to the transition curves in these figures represent the variations in the values of Ra_c that occur when the constant term is added to the $\varepsilon_i = 0$ version of the

26 SEPTEMBER 1981 1120 UTC

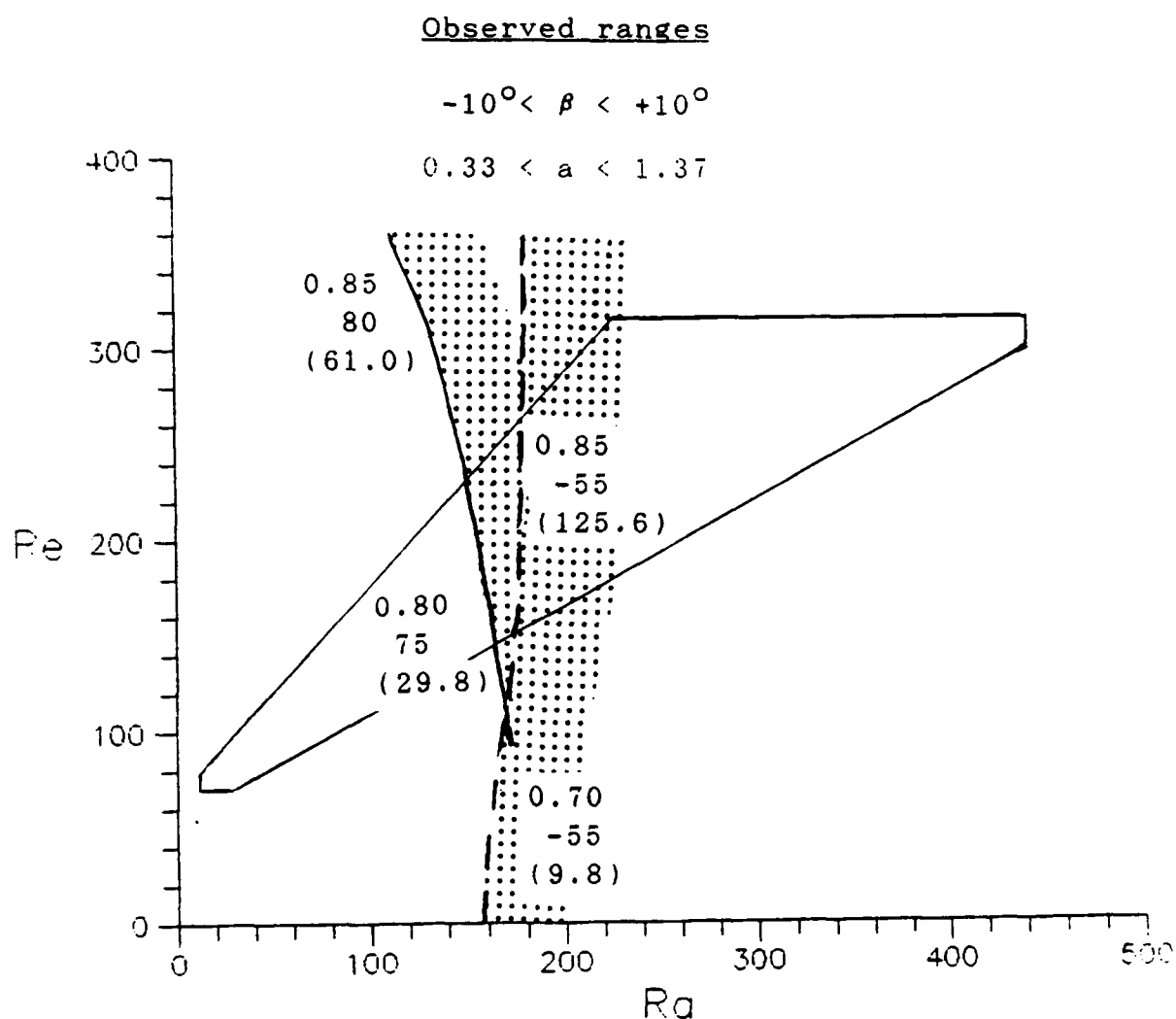


Fig. 5.7 Mode Diagram for the $\varepsilon_i = 0$ Case on 26 September 1981. The observed (Ra, Re) -forcing region is denoted by the tilted box and the stippled region near the transition curves denote the uncertainty in the locations of the curves owing to the method of determining the values of ε_i (see text). The thermal q-mode is denoted by a dashed line and the inflection point mode is denoted by a solid line. Preferred values of a are given above preferred values of β (in degrees). Preferred values of $|\omega_0^*|$ are shown in parentheses. Here $q = 1$, $n = 2$, $P = 1$, $z_{Tp} = 450$ m.

18 SEPTEMBER 1981 0855 UTC

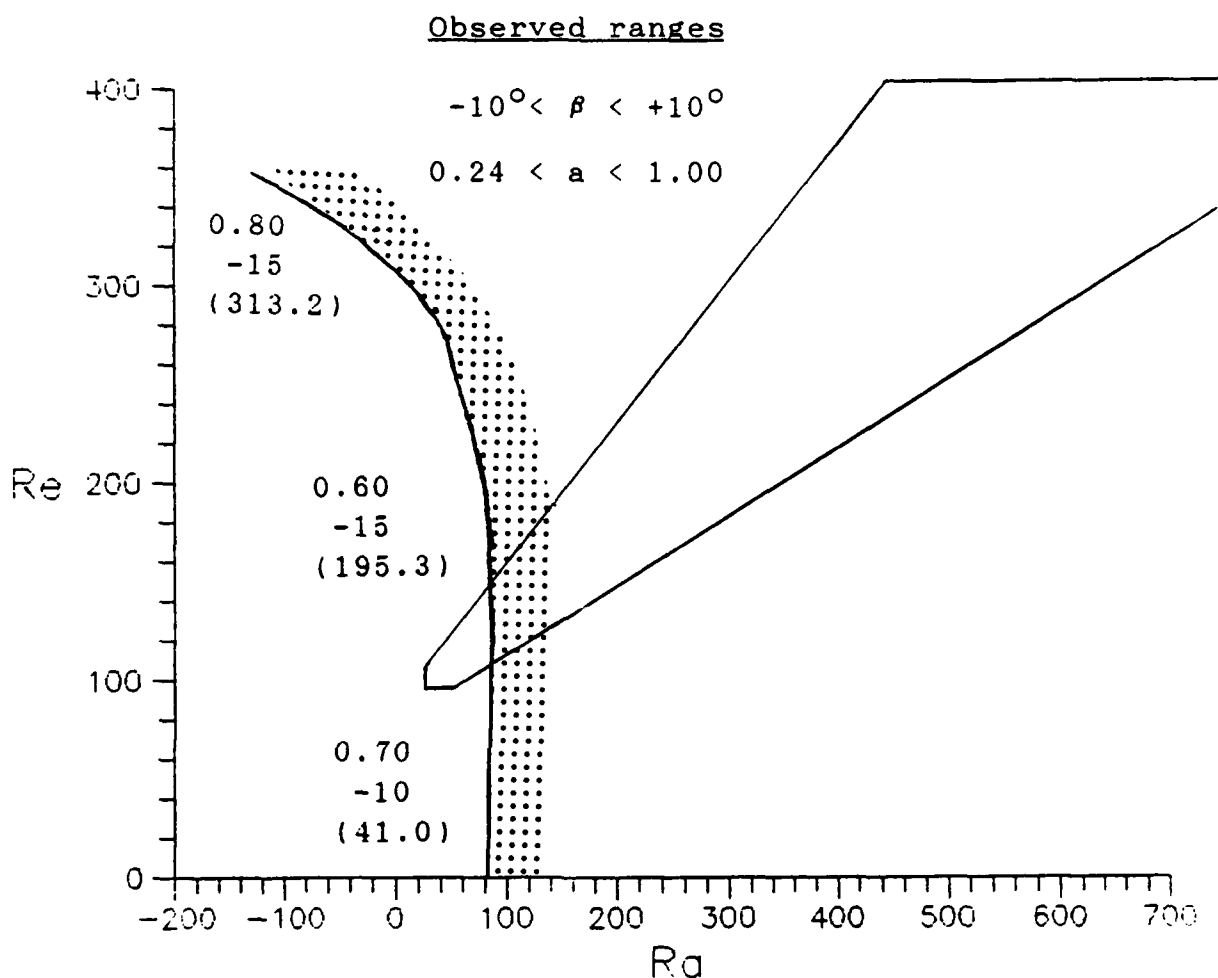


Fig. 5.8 Mode Diagram for the $\varepsilon_i = 0$ Case on 18 September 1981. The observed (Ra, Re)-forcing region is denoted by the tilted box and the stippled region near the transition curve denotes the uncertainty in the location of the curve owing to the method of determining the values of ε_i (see text). Here, the preferred transition curve is the only one that exists and is probably a hybrid of the thermal q-mode and the inflection point mode. Preferred values of a are given above preferred values of β (in degrees).

Preferred values of $|\omega_0^*|$ are shown in parentheses. Here $q = 1$, $n = 2$, $P = 1$, $z_{Tp} = 525$ m.

potential temperature expansion (5.2). Normally, a constant term is needed in any least squares fit to data. However, not including the constant in (5.2) ties the nonharmonic portion of the potential temperature profile to the observed value at the surface (dotted lines in Figs. 5.5 and 5.6; further explanation is provided below).

The linear component $\Delta_z \theta_{(air)}$ gives two effects that are related. First, it makes the approximate temperature profile more representative of the observed values. Second, the linear contribution affects the values of the critical thermal forcing Ra_c that must be determined from our model-calculated values of Ra_{ec} . Because we used the sea surface/air temperature difference to estimate the values of Ra for the atmosphere, we want values of Ra_c rather than values of Ra_{ec} in order to compare the observed and modeled cases. Using (2.18), we must subtract from Ra_{ec} the contribution Ra_i due to the linear component of the profile. On both 18 and 26 September, the linear components of the potential temperature profiles are positive, and so by (2.34) we have $Ra_i \propto -\Delta_z \theta_{(air)} < 0$; thus the resulting adjustments to Ra_{ec} are positive. Hence we must shift the transition curves to the right in Figs. 5.7 and 5.8 (and also in Figs. 5.10 and 5.12 in Section 5.4.2). Thus, as mentioned in Section 2.1.3, the values of $Ra_c > 0$ must be larger than the values of Ra_{ec} given by the model in order for dynamically driven rolls to occur in a

statically stable environment.

Including the constant term θ_0 , in addition to the linear term $\Delta_z \theta_{(air)}$, in the Fourier temperature expansion (5.2) produces the stippled regions in Figs. 5.7 and 5.8 (and also in Figs. 5.10 and 5.12 in Section 5.4.2). The stippled regions in Figs 5.7 and 5.8 are direct results of not explicitly representing the vertical temperature profile in the stability analysis. In both cases, the transition curves are shifted to the right in (Ra, Re) -parameter space by an amount equal to the contribution of only the linear term $\Delta_z \theta_{(air)}$ in the expansion (5.2) of the potential temperature profile. The width of the stippled regions to the right of transition curves is proportional to the magnitude of the linear term when a constant term is added to the expansion (5.2). Including the constant term increases the magnitude of the linear term and maintains its positive sign; for example, on 18 September the linear term increases from a value of 0.43 to 0.72 °C and on 26 September it increases from a value of 0.44 to 0.55 °C. These stippled regions, therefore, depict the amount of uncertainty in the location of the transition curves when slightly different expansions are chosen to determine the magnitude of the linear contribution to the potential temperature profile. For the $\epsilon_i = 0$ case, it appears that the constant term is relatively important; the uncertainty in the location of

the transition curves equals a variation in Ra of about 40 to 50.

For the case of 26 September shown in Fig. 5.7, we can easily identify the two physically relevant roll modes. The thermal q-mode is identified in the statically unstable regime (dashed line). The inflection point mode (solid line) is normally characterized by its being the mode that crosses the line $Ra = 0$; however, since we use Ra rather than Ra_e , the curves are shifted toward positive values of Ra as noted above. The value of the critical Reynolds number Re_c at neutral stability ($Ra = 0$) is 228.0. The values of z_T , a_p and β_p that correspond to the inflection point curve are well within the observed values of a and β but the values of β_p for the thermal mode are not representative of the observed values. Thus, on this day, we feel that the inflection point mode is the dominant mode, in agreement with Brümmer (1985) and Stensrud and Shirer (1988). Within the observed (Ra,Re)-region, we get $\beta_p = 75^\circ$ for the inflection point mode. Thus the roll axis is 15° to the left of the mean wind direction, which was reported by Brümmer (1985) to correspond to the observed orientation. A physically more accurate reference direction with which to compare the orientation angles given by the model is the direction of the mean wind shear value (Table 5.3). We use Simpson's rule to determine this value. On 26 September we find that the direction of the

mean wind shear is 7° to the left of the mean wind direction. The difference between the model and this reference direction is then only 8° --a significant improvement over using the mean wind as the reference direction.

Table 5.3

Summary of Typical Model Results
for the Inflection Point Instability Mode.

Case	β_p (degrees)				a_p			T_p	
	OBS		MODE		OBS	MODEL		MODEL	
	\tilde{V}_s	\tilde{V}_m	$\varepsilon_i=0$	$\varepsilon_i \neq 0$		$\varepsilon_i=0$	$\varepsilon_i \neq 0$	$\varepsilon_i=0$	$\varepsilon_i \neq 0$
18 Sep	-86	-90	-10	-75	0.24- 1.00	1.25	0.65	1 min	7 min
26 Sep	83	90	75	70	0.33- 1.37	0.80	0.80	4 min	3 min

18 Sep: $Re_c \approx 50$ 26 Sep: $Re_c \approx 150$

\tilde{V}_s is the direction of the mean wind shear and \tilde{V}_m is the direction of the mean wind

A typical frequency $|\omega_0^*|$ for the inflection point mode corresponds to a typical roll period of about three to four minutes and a phase velocity of approximately four to five meters per second. This phase velocity is greater than the cross-roll wind component, indicating that the roll is propagating downstream in addition to being advected by the

mean cross-roll wind. In addition, the phase velocity given by the thermal mode is about 20 percent larger than the phase velocity given by the inflection point mode. In comparison, Brown (1972) states that roll periods typically vary between 15 minutes and two hours and LeMone (1973) observed periods of 30 to 46 minutes in her case study. Our model apparently gives roll periods that are about five to ten times shorter than would be expected, possibly due to the rigid lid approximation or to the limited number of spectral components in the model. The reason for these higher than expected frequency rates must be understood in order to produce a spectral model that accurately captures all of the roll characteristics. Overall, however, the results for the linear temperature profile case on 26 September compare favorably with the observations, in agreement with Stensrud and Shirer (1988). This result is not altogether unexpected since the linear term well approximates the potential temperature profile (Fig. 5.6).

On 18 September, we cannot unambiguously identify separate thermal and inflection point modes, except for the appropriate limiting values of $Re_c = 0$ and $Ra_c = 0$. The mode that is indicated in Fig. 5.8 is the one corresponding to $(Ra_c)_{min}$, that is, it is the preferred mode. There appears to be considerable interaction between the thermal and inflection point modes making it difficult to distinguish where one mode ends and another begins.

Throughout the values of Re corresponding to the atmosphere, there are no apparent differences in aspect ratios, frequencies or orientation angles between the two modes.

To confirm that the curve shown in Fig. 5.8 for 18 September gives the preferred mode and to determine if there are two modes and how we might separate them, we contoured the values of Ra_c as functions of a and β for various values of Re_c . Fig. 5.9 shows a typical graph for the linear temperature case on 18 September at $Re_c = 50$. Immediately, we can see in Fig. 5.9 that only one mode exists. Thus the curve depicted in Fig. 5.8 is not only the preferred mode, it is the only mode that exists, possibly a hybrid rather than a pure mode.

The values of the orientation angles and aspect ratios associated with the preferred mode given in Fig. 5.8 match those values of a_p and β_p given by the mode in Fig. 5.9 that we identify with the thermal mode. The values of a compare favorably with the observed ones. However, the orientation angles along the part of the transition curve near the observed (Ra, Re) -region in Fig. 5.8 have values of -10° , or 80° to the right of the mean wind direction (Table 5.3). We use a typical frequency for the inflection point mode within the observed (Ra, Re) -region to calculate the propagation period for this case, and we find that it is on the order of one minute. This propagation period appears

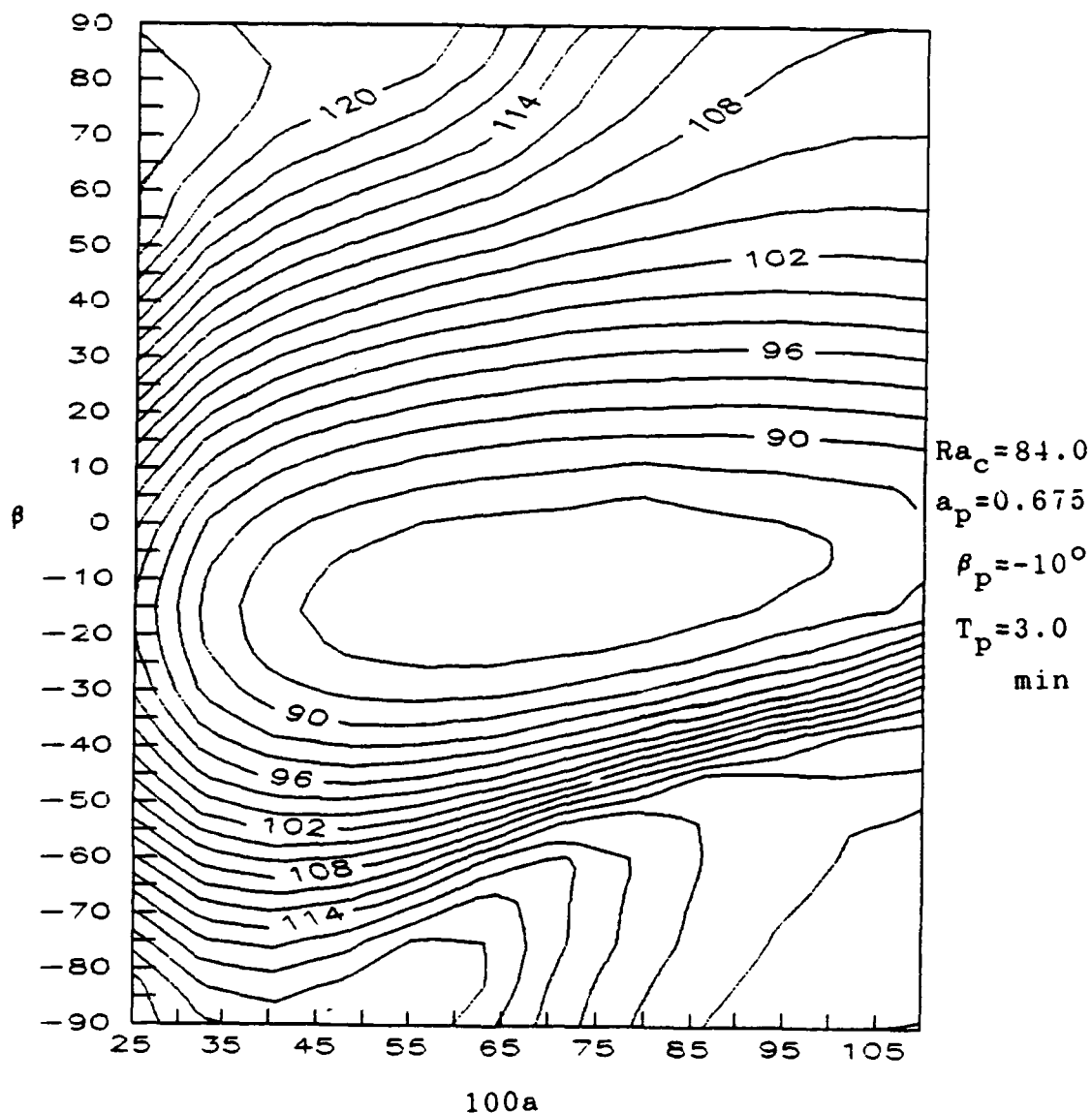


Fig. 5.9 Contour Diagram Showing Values of Ra_c as Functions of a and β for $Re_c = 50$ in the $\epsilon_i = 0$ Case for 18 September 1981 Shown in Fig. 5.8. The parameter values corresponding to the preferred mode given by the minimum value of Ra_c are noted to the right of the diagram.

to be too short to be physically realistic. We conclude from Fig. 5.8 that the $\varepsilon_i = 0$ case for 18 September does not give satisfactory results, in agreement with the conclusion of Haack-Hirschberg (1988) who also used a linear temperature profile. We next investigate the effects of including the complete inversion ($\varepsilon_i \neq 0$) case on the stability analyses for 18 and 26 September.

5.4.2 The Nonlinear ($\varepsilon_i \neq 0$) Temperature Profile Case

The mode diagrams for the full inversion cases are given by Figs. 5.10 and 5.12; they follow the same format as that used in Figs. 5.7 and 5.8. As before, the locations of the small shifts in the transition curves (stippled regions) are due to the method by which the least squares program fits a curve to the potential temperature profile when a constant term is and is not included in the expansion (5.2). For the case of 26 September, the linear term $\Delta_z \theta_{(\text{air})}$ remains positive and increases in magnitude from 0.39 to 4.4 °C when the constant term is included. In this instance, the net effect of the new magnitudes of the coefficients multiplying the trigonometric functions is to offset the large change in magnitude of the linear term and to shift the curve slightly to the left, as shown by the stippled region in Fig. 5.10. For the case of 18 September, the linear term changes in magnitude and sign

from 0.30 to -1.05°C . However, owing to the effect of the new magnitudes of the coefficients multiplying the trigonometric functions, the transition curves in Fig. 5.12 shift to the right slightly, thereby offsetting the effect of the changes in magnitude and sign of the linear term. The widths of the stippled regions shown in Figs. 5.10 and 5.12 depict the small amount of error introduced into the values of Ra_c when the constant term is not used in the expansion (5.2). For the $\varepsilon_i \neq 0$ case, we see that the constant terms can be neglected without introducing significant errors into Ra_c ; the variations in Ra_c given by the stippled regions in Figs. 5.10 and 5.12 are less than 10 in both cases.

As seen in Fig. 5.10 for 26 September, the thermal and inflection point modes apparently interact in the same manner as they did for the non-inversion case on the 18th. The transition curve here represents only the preferred mode that occurs at the minimum values of Ra_c and Re_c . Figure 5.11 shows the contoured graph of Ra_c as a function of a and β at a value of $Re_c = 150$ for the nonlinear temperature profile case on 26 September. In contrast to Fig. 5.9, we see that there are two modes present, as normally expected. Two modes also occurred at each value of Re_c that we tested. Thus it is possible to separate these individual modes, but it requires a grid of about 1, 2 and 0.025 in Re , β and a , respectively. A grid of this

26 SEPTEMBER 1981 1120 UTC

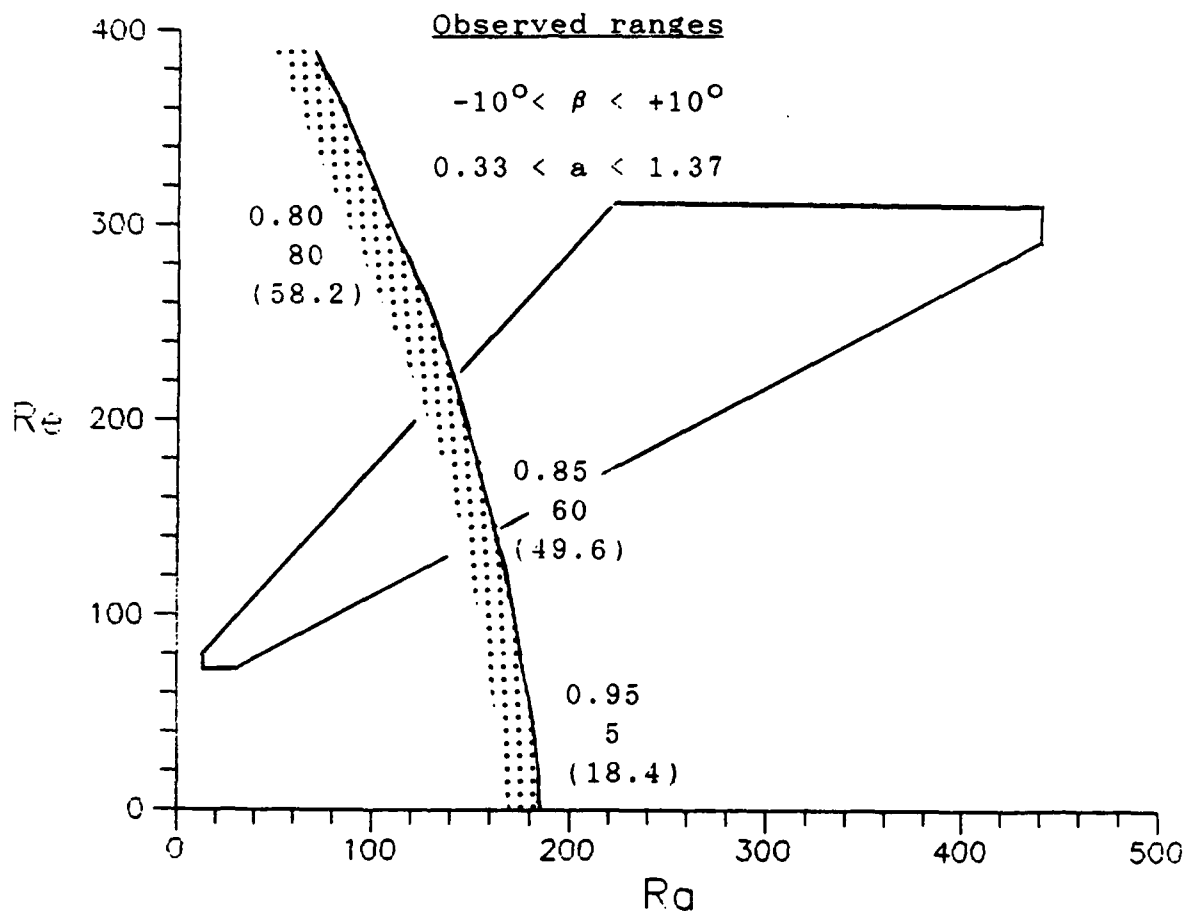


Fig. 5.10 Mode Diagram for the $\varepsilon_i \neq 0$ Case on 26 September 1981. The observed (Ra, Re) -forcing region is denoted by the tilted box and the stippled region near the transition curve denotes the uncertainty in the location of the curve owing to the method of determining the values of ε_i (see text). Here, the preferred transition curve is the minimum one consisting of the thermal q-mode at lower values of Re and the inflection point mode at higher values of Re . Preferred values of a are given above preferred values of β_p (in degrees). Preferred values of $|\omega_0^*|$ are shown in parentheses. Here, $q = 1$, $n = 2$, $P = 1$, $z_{Tp} = 450$ m and $\nu = 17$ m²/s.

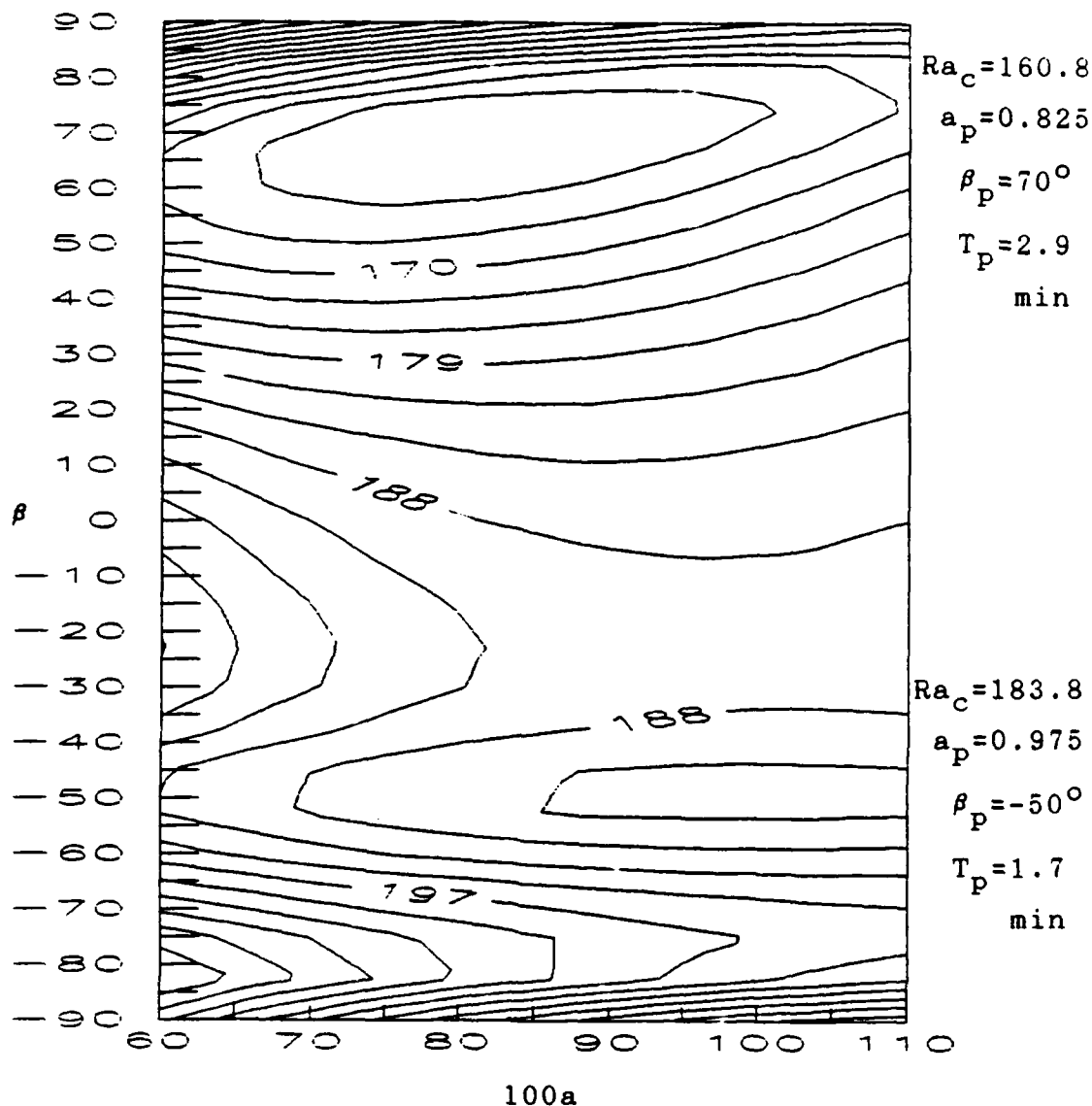


Fig. 5.11 Contour Diagram Showing Values of Ra_c as Functions of a and β for $Re_c = 150$ in the $\varepsilon_i \neq 0$ Case on 26 September 1981 Shown in Fig. 5.10. The parameter values corresponding to the two preferred modes given by the local and global minimum values of Ra_c are noted to the right of the diagram.

18 SEPTEMBER 1981 0855 UTC

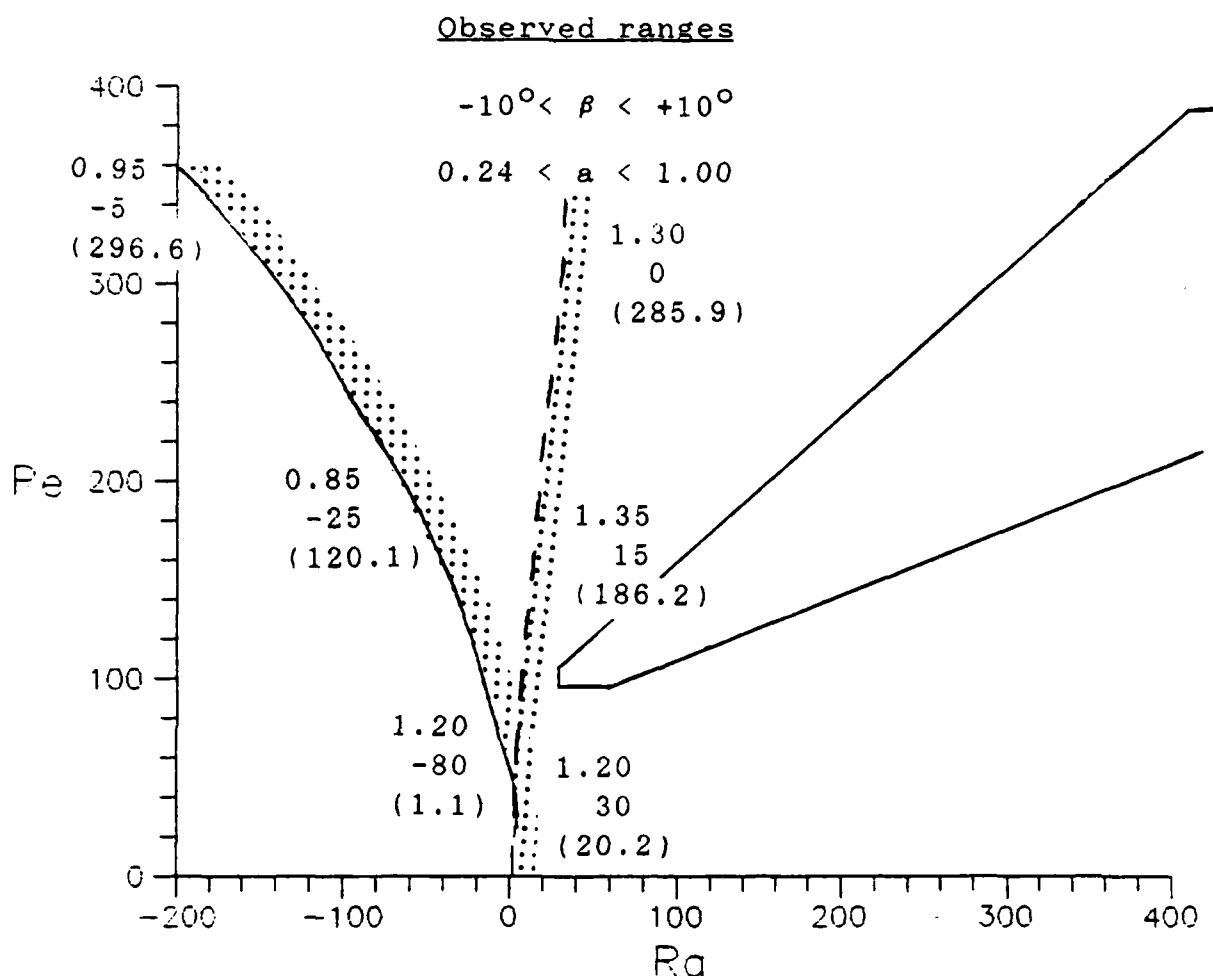


Fig. 5.12 Mode Diagram for the $\varepsilon_1 \neq 0$ Case on 18 September 1981. The observed (Ra, Re) -forcing region is denoted by the tilted box and the stippled regions near the transition curves denote the uncertainty in the locations of the curves owing to the method of determining the values of ε_1 (see text). The thermal q-mode is denoted by the dashed line and the inflection point mode is denoted by the solid line. Preferred values of a_p are given above preferred values of β_p (in degrees). Preferred values of $|\omega_0^*|$ are shown in parentheses. Here $q = 1$, $n = 2$, $P = 1$, $Z_{Tp} = 525$ m and $\nu = 30$ m²/s.

resolution is too fine to be computationally practical in this case over the range required to perform the analysis.

One of the modes in Fig. 5.11 occurs at a local minimum value in Ra_c ($Ra_c \approx 184$) and has an orientation angle that is about 40 degrees from the observed value. The value of β_p corresponding to this mode changes little and its value of Ra_c increases gradually as the magnitude of Re_c increases. This mode displays characteristics of the thermal mode. The other mode occurs at a global minimum value in Ra_c ($Ra_c \approx 161$) that decreases as the magnitude of Re_c increases. This effect combined with the fact that values of β_p change significantly with changes in the magnitude of Re_c , leads us to conclude that this mode in Fig. 5.11 is the inflection point mode. The corresponding values of β_p compare favorably with the observed values of β (Table 5.3). The values of a_p and β_p for this mode are not quite as representative of the observed values as those for the $\epsilon_i = 0$ case.

One of the results of including the full inversion for the 26 September case is to increase the roll aspect ratio a . The analysis of the billows profile in Chapter 4 also revealed an increase in the magnitude of a when $\epsilon_i \neq 0$ and, as we stated there, we believe that the value of a_p increases in response to the increase in static stability, as well as to the increase in values of z_{Tp} that occur when wind shear in the inversion forces deeper rolls to exist.

The orientation angle β_p decreases slightly for the full inversion case meaning that the angle that the roll makes with the mean wind direction increases. For example, at a value of $Re_c \approx 140$, we find that $\beta_p = 70^\circ$. The angle that the roll makes with the mean wind direction is therefore 20° . For the linear case, the roll axis is aligned 15° from the observed direction. Since β_p has increased in the full inversion case, for consistency the magnitude of the cross-roll wind should increase and the propagation period should decrease. Indeed, the propagation period decreases to about three minutes.

In general, we conclude that on 26 September the linear case gives better results than the nonlinear case. Previous researchers (e.g., Haack-Hirschberg, 1988; Stensrud, 1987; and Shirer and Brümmer, 1986) have found satisfactory results from their models that do not include a capping inversion. Their models assumed a linear temperature profile that well approximates the observed profile on the 26th. We think that the nonlinear Fourier temperature coefficients ε_i that we used introduced some error in the representation of the deviation from the predominantly linear temperature profile. We conclude that the shear in the inversion was not able to drive circulations significantly into the inversion.

As can be seen by comparing Figs. 5.8 and 5.12, the ε_i terms significantly improve the results for 18 September.

In Fig 5.5, we discovered that the potential temperature profile on the 18th can be approximated adequately only by a nonlinear function. The requirement of a nonlinear potential temperature function to adequately represent the potential temperature profile likely explains the failure of simpler models. Unlike the case of 26 September, the ϵ_i terms for the case of 18 September allow for a clear distinction between instability modes. The thermal mode (dashed line) shown in Fig. 5.12 is located in the statically unstable region and the inflection point mode (solid line) is characterized by neutral stability. Of the two possible instability mechanisms, the inflection point mode clearly represents the observed values much better and so these rolls are likely to have been dynamically driven, in agreement with Brümmer (1985). Fig. 5.3 reveals the existence of a very large amount of wind shear within the inversion on the 18th and so we conclude, in agreement with model results, that the inflection point instability mechanism could have driven the rolls only if they had extended significantly into the inversion.

As with the case of 26 September and the billows case, the values of a_p for the case of 18 September increase with the inclusion of the nonlinear terms ϵ_i (Table 5.3). The increase in the value of a_p on this day is significant and less representative of the observed range of the values of a . However, the difference in the values of a_p in this

case may not signify a problem with our model. As noted in Section 5.1, the cloud streets on the 18th were well developed and had been observed for hours before the observations were taken, and so they have likely evolved to an advanced stage of development. Etling and Raach (1987) showed that roll circulations tend to develop smaller values of a as the magnitude of the forcing rates increase (i.e., as the atmospheric forcing values move away from those values required for bifurcation) in order to transport energy more efficiently. Finding larger preferred values of a , which are associated with the minimum value of the bifurcation point, than observed is consistent with this general cell broadening result (see also Chang and Shirer, 1984).

The most significant improvement in the 18 September case is in the value of β_p . Here, for values of Re_c near the range for the atmosphere, the values of β_p improve to -80° at $Re_c \approx 25$ and to -70° at $Re_c \approx 60$. These angles are even closer to the mean wind shear reference direction that is 4° to the right of the mean wind direction, giving a reference angle of -86° (Table 5.3). At increasingly larger values of the wind speed or Re_c , β_p gradually decreases in magnitude, and so the cross-roll wind component increases in value. This decrease in the values of β as the magnitude of the wind speed increases is in agreement with the roll energy balance equation (2.78).

For constant values of the other generation and dissipation terms in (2.78), we use the definition of the Reynolds stress RS in (2.75) to show that RS can also remain unchanged in (2.78) for increases in the magnitude of Re_c if the value of β_p is decreased in magnitude so that the Fourier coefficient Λ_2 is decreased in value.

Since the rolls on 18 September with $\epsilon_i \neq 0$ are now aligned more nearly parallel to the mean wind direction, the roll periods have increased significantly from their values in the linear case. With the nonlinear terms ϵ_i included in the model, the roll period at a value of $Re_c \approx 60$ becomes six to seven minutes. However, since the values of β_p decrease rapidly with values of Re_c , the roll propagation periods decrease correspondingly.

On both 18 and 26 September, we find that a shear mode begins at values of $Re_c > 360$ for both the linear and nonlinear cases. These values of Re_c are located at the upper limit of the range of values of Re for the atmosphere on both days. In addition, the range of observed values of Ra for the atmosphere is located in the statically unstable region given by $Ra > 0$, whereas the shear mode is located at values of $Ra < -600$. For these reasons, we do not consider the shear mode to be physically relevant in these cases, and so we do not include them on our regime diagrams.

5.4.3 Summary of Results

As stated in Chapters 1 and 2, the effects on the stability analysis of including the nonlinear terms ε_i in the definition of the vertical variation of background temperature may not be apparent until a specific case is examined. We have found that the ε_i terms provide significant improvement in model results for a temperature profile having a distinct capping inversion and significant wind shear, such as occurred on 18 September. When used with a case having an approximately linear temperature profile and a smaller amount of shear as on 26 September, we found that the ε_i terms give slightly poorer results. On 18 September, our model gives values of a_p and β_p that are in good agreement with the observed values only for the nonlinear ($\varepsilon_i \neq 0$) case. The values of a_p in this case are near the upper limit of the observed values.

Including the nonlinear temperature terms in the model causes a marked increase in the roll aspect ratios for the billows case and the cases of 18 and 26 September. On 18 September the nonlinear temperature terms shift all modes toward more negative values of the thermal forcing; on 26 September there is no significant shift in the transition curve. Also on 18 September, which is the case having the larger amount of shear in a more distinct inversion, the ε_i terms tend to increase the roll periods to values closer to

the expected ones in comparison with the $\epsilon_i = 0$ case. However, the periods produced by $\epsilon_i \neq 0$ case are still about five times too small, which as we noted above suggests that further model improvement is needed. The values of β_p on both days may signal even better agreement with the observed values since Shirer and Haack (1989), using FIRE data, have shown that removing some of the linear component of the background cross-roll wind improves β_p by as much as 15 to 20 degrees. We have found that the inflection point instability mechanism likely produced the rolls on both 18 and 26 September, which is in agreement with the energetics analyses by Brümmer (1985). Table 5.3 above summarizes our results and compares them with the observed values.

In this study, we have gained considerable insight into the representation of boundary layer roll circulations that develop in the presence of an arbitrary vertical temperature profile and an arbitrary, vertically sheared, horizontal wind profile. In particular, we have seen how shear in an inversion above a well-mixed layer can interact synergistically with thermal forcing from below to produce a boundary layer roll circulation extending well into the inversion. We conclude that for many cases this type of spectral modeling approach captures the information necessary for adequate representation of boundary layer rolls. However, to be certain, further testing with data

from other field programs such as FIRE and ERICA is clearly needed. Owing to the inclusion of the additional physical effects via the arbitrary temperature representation, there may be a secondary application of this model. An interesting experiment would be to apply this model to the transverse bands or billow clouds that frequently are found in the atmosphere at levels of three to six thousand meters.

REFERENCES

- Agee, E.M., T.S. Chen and K.E. Dowell, 1973: A review of mesoscale cellular convection. Bull. Am. Meteor. Soc., 54, 1004-1012.
- Asai, T., 1970: Stability of a plane parallel flow with variable vertical shear and unstable stratification. J. Meteor. Soc. Japan, 48, 129-138.
- Asai, T., 1972: Thermal instability of a shear flow Turning the direction with height. J. Meteor. Soc. Japan, 50, 525-532.
- Asai, T. and I. Nakasuji, 1973: On the stability of Ekman boundary layer flow with thermally unstable stratification. J. Meteor. Soc. Japan, 51, 29-42.
- Brown, R.A., 1970: A secondary flow model for the planetary boundary layer. J. Atmos. Sci., 27, 742-757.
- Brown, R.A., 1972: On the inflection point instability of a stratified Ekman boundary layer. J. Atmos. Sci., 29, 850-859.
- Brown, R.A., 1980: Longitudinal instabilities and secondary flows in the planetary boundary layer: A review. Rev. Geophys. Space Phys., 58, 683-697.
- Brümmer, B., 1985: Structure, dynamics and energetics of boundary layer rolls from KonTur aircraft observations. Beitr. Phys. Atmos., 58, 237-254.
- Brümmer B., S. Bakan and H. Hinzpeter, 1985: KonTur: Observations of cloud streets and open cellular structures. Dyn. Atmos. Ocean, 9, 281-296.

- Brümmer B. and M. Latif, 1985: Some studies on inflection point instability. Beitr. Phys. Atmos., 58, 117-126.
- Chang, H.R. and H.N. Shirer, 1984: Transition in shallow convection: An explanation for lateral cell expansion. J. Atmos. Sci., 41, 2334-2346.
- Clark, T.L., T. Hauf and J.P. Kuettner, 1986: Convectively forced internal gravity waves: Results from two-dimensional numerical experiments. Quart. J. Roy. Meteor. Soc., 112, 899-926.
- Devaney, R.L., 1987: An Introduction to Chaotic Dynamical Systems. Addison Wesley, 320 pp.
- Drazin, P.G. and L.N. Howard, 1966: Hydrodynamic stability of parallel flow of inviscid fluid. Advan. Appl. Mech., 9, 1-89.
- Dutton, J.A., 1976: The Ceaseless Wind: An Introduction to the Theory of Atmospheric Motion. McGraw-Hill, New York, 579 pp.
- Etling, D., 1971: The stability of an Ekman boundary layer flow as influenced by the thermal stratification. Beitr. Phys. Atmos., 44, 168-186.
- Etling, D. and S. Raasch, 1987: Numerical simulation of vortex roll development during a cold air outbreak. Dyn. Atmos. Oceans, 10, 277-290.
- Faller, A.J. and R.E. Kaylor, 1966: A numerical study of the instability of the laminar Ekman boundary layer. J. Atmos. Sci., 23, 466-480.

- Haack-Hirschberg, T., 1988: Boundary layer roll circulations in a stratified atmosphere. M.S. Thesis, The Pennsylvania State University, 161 pp.
- Haack, T.H. and H.N. Shirer, 1989: Boundary layer roll circulations in a stratified atmosphere. Manuscript in publication.
- Higgins, R.W., 1987: From the equations of motion to spectral models. Chapter 3 in Nonlinear Hydrodynamic Modeling: A Mathematical Introduction, H.N. Shirer (Ed.), Lecture Notes in Physics, 271, Springer-Verlag, Heidelberg, 47-85.
- Hirsch, M.W. and S. Smale, 1974: Differential Equations, Dynamical Systems, and Linear Algebra. Academic Press, New York, 358 pp.
- Kaylor, R.E. and A.J. Faller, 1972: Instability of the stratified Ekman boundary layer and the generation of internal gravity waves. J. Atmos. Sci., 29, 497-509.
- Kelly, R.D., 1984: Horizontal roll and boundary-layer interrelationships observed over Lake Michian. J. Atmos. Sci., 29, 497-509.
- Kuettner, J.P., 1959: The band structure of the atmosphere. Tellus, 11, 267-294.
- Kuettner, J.P., 1971: Cloud bands in the earth's atmosphere: Observations and theory. Tellus, 23, 404-425.
- Laufersweiler, M.J. and H.N. Shirer, 1989: A simple dynamical model of a stratocumulus-topped boundary layer. J. Atmos. Sci., 46, 1133-1153.

- LeMone, M.A., 1973: The structure and dynamics of horizontal roll vortices in the planetary boundary layer. J. Atmos. Sci., 33, 1308-1320.
- Lilly, D.K., 1966: On the instability of Ekman boundary flow. J. Atmos. Sci., 23, 481-494.
- Lorenz, E.N., 1960: Maximum simplification of the dynamic equations. Tellus, 12, 243-254.
- Lorenz, E.N., 1963: Deterministic nonperiodic flow. J. Atmos. Sci., 20, 130-141.
- Marsden, J.E. and M. McCracken, 1976: The Hopf Bifurcation and its Applications. Applied Mathematical Sciences, 19, Springer-Verlag, Heidelberg, 408 pp.
- Nicholls, S., 1984: The dynamics of stratocumulus: aircraft observations and comparisons with a mixed layer model. Quart. J. Roy. Meteor. Soc., 110, 783-820.
- Plank, V.G., 1966: Wind conditions in situations of patternform and nonpatternform cumulus convection. Tellus, 18, 1-12.
- Plye, R.J., 1987: Typical branching forms: Periodic solutions. Chapter 11 in Nonlinear Hydrodynamic Modeling: A Mathematical Introduction, H.N. Shিরer (Ed.), Lecture Notes in Physics, 271, Springer-Verlag, Heidelberg, 264-291.
- Rayleigh, Lord, 1880: On the stability, or instability, of certain fluid motions. Scientific Papers, I, 474-487.

- Rayleigh, Lord, 1916: On convective currents in a horizontal layer of fluid when the higher temperature is on the underside. Phil. Mag., 32, 520-546.
- Shirer, H.N., 1980: Bifurcation and stability in a model of moist convection in a shearing environment. J. Atmos. Sci., 37, 1586-1602.
- Shirer, H.N., 1986: On cloud street development in three dimensions: Parallel and Rayleigh instabilities. Beitr. Phys. Atmos., 59, 129-149.
- Shirer, H.N., (Ed.), 1987a: Nonlinear Hydrodynamic Modeling: A Mathematical Introduction, Lecture Notes in Physics, 271, Springer-Verlag, Heidelberg, 546 pp.
- Shirer, H.N., 1987b: A simple nonlinear model of convection. Chapter 2 in Nonlinear Hydrodynamic Modeling: A Mathematical Introduction, H.N. Shirer (Ed.), Lecture Notes in Physics, 271, Springer-Verlag, Heidelberg, 22-46.
- Shirer, H.N. and B. Brümmer, 1986: Cloud streets during KonTur: A comparison of parallel/thermal instability modes with observations. Beitr. Phys. Atmos., 59, 150-169.
- Shirer, H.N. and J.A. Dutton, 1979: The branching hierarchy of multiple solutions in a model of moist convection. J. Atmos. Sci., 36, 1705-1721.
- Shirer, H.N. and T. Haack, 1989: Modifications of the background flow by roll vortices. Extended abstract volume for the 1989 FIRE annual meeting.

- Stensrud, D.J., 1985: On the development of boundary layer rolls from the inflection point instability. M.S. Thesis, The Pennsylvania State University, 125 pp.
- Stensrud, D.J., 1987: The expected branching solution: Preferred wavelengths and orientations. Chapter 12 in Nonlinear Hydrodynamic Modeling: A Mathematical Introduction, H.N. Shirer (Ed.), Lecture Notes in Physics, 271, Springer-Verlag, Heidelberg, 292-324.
- Stensrud, D.J. and H.N. Shirer, 1988: Development of boundary layer rolls from dynamic instabilities. J. Atmos. Sci., 45, 1007-1019.
- Suarez, M.J., A. Arakawa and D.A. Randall, 1983: The parameterization of the planetary boundary layer in the UCLA General Circulation Model: formulation and results. Mon. Wea. Rev., 111, 2224-2243.

Appendix

A Portion of the Output Produced by the Symbolic Manipulator CFORMAC That Was Used to Find the Coefficients in (3.12).

Here, A, B, D and F are the coefficients A_i , B_i , D_i and F_i in the imaginary portion of (3.12).

a=coeff(imag,w**3)

A = - P B1 - P B2 - B1 - B2

b=coeff(imag,re*w**2)

B = - P B1 A3 - P B1 A5 - P B1 A7 - P A1 B2 - P B2 A5 - P B2 A7 -
A1 - B1 A3 - B1 A7 - A1 B2 - B2 A3 - B2 A5

d=coeff(imag,w*re**2)

D = - P B1 A3 A5 - P B1 A3 A7 - P B1 A5 A7 + P B1 A6² - P A1 B2

- P A1 B2 A7 - P B2 A5 A7 + P B2 A6² - B1 A1 A3 - B1 A1 A7 + B1
A4 - B1 A3 A7 - A1 B2 A3 - A1 B2 A5 + A2 A4 B2 - B2 A3 A5

f=coeff(imag,w*re)

F = 0

f=coeff(imag,w*ra)

F = - P B1 D2 - P D1 B2 - B1 D2 - D1 B2

c1=coeff(imag,w)

C1 = P² B1² B2 + P² B1 B2² + P B1² B2 - P B1 RE² A3 A5 - P B1